A MULTI-SCALE AND MULTI-PHYSICS FRAMEWORK FOR INTEGRATED ELECTRONICS OPERATING IN HARSH ENVIRONMENT: A SENSOR-TO-SYSTEM PERSPECTIVE

A Dissertation

Submitted to the Faculty

of

Purdue University

by

Xin Jin

In Partial Fulfillment of the

Requirements for the Degree

of

Doctor of Philosophy

May 2020

Purdue University

West Lafayette, Indiana

THE PURDUE UNIVERSITY GRADUATE SCHOOL
STATEMENT OF DISSERTATION APPROVAL

Dr. Muhammad A. Alam, chair

School of Electrical and Computer Engineering

Dr. Mark Lundstrom

School of Electrical and Computer Engineering

Dr. David Janes

School of Electrical and Computer Engineering

Dr. Alexander Wei

Department of Chemistry

Approved by:

Dr. Dimitrios Peroulis

Head of the school of Electrical and Computer Engineering

This thesis is dedicated to my parents, for their selfless love, support and sacrifices.

ACKNOWLEDGMENTS

I would like to express my sincere gratitude to my advisor, Professor Muhammad A. Alam, for accepting me as a direct PhD student in his group about 6 years ago, for his mentorship, and for his continuous support during these years. He gave me the opportunity to study and conduct research in the field of bio-electronic devices modeling, which is a valuable experience for my future career. He shared me with countless knowledge in device physics and has always been very supportive whenever I have a question. He provided me with great help in improving the quality of my research and has always been open to discuss about new ideas.

I am thankful to Professor Mark Lundstrom and Prof. David Janes, for their serving as my PhD committee members and for their patience in answering my questions. From their courses (ECE 656 and ECE 557), I have learned a lot about the fundamentals in carrier transport, semiconductor device physics, and integrated circuit/MEMS fabrication.

I sincerely thank Professor Alexander Wei for serving as my PhD committee member. I appreciate him for many insightful discussions from a chemist's perspective. He has always been very kind to offer me helpful guidance to solve various scientific and technical problems.

I am grateful to Professor John A. Rogers from Northwestern University for many years of research collaborations in the field of bio-electronics. He has been inspired me to come up with many new ideas, connected me with very supportive experts and researchers, and provided me with many helpful suggestions.

I would like to thank Professor Ali Shakouri at Purdue Birck Nanotechnology Center for introducing me to the Scalable Manufacturing of Aware & Responsive Thin Films (SMART) project, where I got the chance to present my work and to meet many experts in this field.

I am also thankful to Professor Jan Allebach, Professor Mukerrem Cakmak, Professor Dimitrios Peroulis, Professor Bruno Ribeiro, Professor Rahim Rahimi, Professor Hyowon Lee, and Professor Jenna Rickus. Some of the most critical results in my research would not be acquired without their help.

And I would like to say special thank you to Dr. Enming Song, Professor Hui Fang, Dr. Amay J. Bandodkar, Dr. Siddarth Sridharan Dr. Jose Ferney Rivera Miranda, and Tran NH Nguyen for their efforts in our collaborative projects. They have always been very patient in answering my questions and extremely responsive to offer experimental support.

I also want to say a big thank you to my former and current colleagues and lab mates. The friendships we built over the years are what I cherish most.

To my past lab mates from Alam's group: Piyush Dak,Aida Ebrahimi, Xingshu Sun, Chunsheng Jiang, Hai Jiang, SangHoon Shin, Ryyan Khan, Raghu Chavali, Nicolo Zagni, Ratul Baruah, Md Abdul Wahab, and Ankit Jain for giving me always kind and insightful replies whenever I ask a question.

To my current lab mates from Alam's group: Marco Fratus, Reza Asadpour, Tahir Patel, Yen-Pu Chen, Bikram Mahajan, and Levi Davies. The weekly group meeting is what I look forward to most. The inspiring discussions and collaborations are invaluable.

To my colleagues from SMART project: Nick Glassmaker, Yang Yan, Qingyu Yang, Ramazan Oduncu, Hongjie, Jiang, Kerry Maize, FNU Chandra Mouli Sekar, Armen Yildirim, Guy Telesnicki, Harris Mousoulis, Nithin Raghunathan, and Xiaofan Jiang. I'm grateful to have so much support from so many ingenious minds.

I also thank all my dear friends, including Dr. Xufeng Wang, Yubo Sun, Dr. Zhiguang Zhou, Dr. Yuanchen Chu, Dr. Evan Wilson, and Matt Mckillip for their caring and encouragement.

I would like to thank Vicki Johnson, Christine M. Ramsey,Jaime J. Turner, Lori J. Carte, Matt Golden, and Elisheba Vanwinkle for their help in scheduling meetings, reserving rooms, and administrative assistance.

Finally, I would like to extend my deepest gratitude to my family. I would like to express my gratitude towards my parents: Qiangning Jin, and Haiou Wang for their unconditional love and unparalleled support that made it possible for me to pursue Ph.D.

TABLE OF CONTENTS

Page

Page

Page

Page

LIST OF TABLES

LIST OF FIGURES

Figure Page

Figure Page

Figure Page

ABSTRACT

Jin Xin Ph.D., Purdue University, May 2020. A Multi-Scale and Multi-Physics Framework for Integrated Electronics Operating in Harsh Environment: A Sensor-to-System Perspective. Major Professor: Muhammad A. Alam.

In a modern IoT network, the design of edge computing electronics operating in harsh environment faces great challenges. In this doctoral thesis, we are developing an end-to-end modeling framework for two IoT-based applications: personalized medicine and precision agriculture. By coupling the physics of analyte mass transfer, electrochemical reactions, and electrostatics, the framework paves the way for the development of the following new generation electrochemical/biosensors: 1) high sensitivity nano-electrode non-enzymatic/enzymatic amperometric glucose sensors, 2) self-powered enzymatic biofuel cell (EBFC)-based lactate sensors, and 3) roll-to-roll printed thin-film ion-selective electrode (ISE)-based soil nitrate sensors.

Glucose sensors have transformed diabetes control. Amperometric glucose sensors with nanoparticle electrodes promise fast and highly sensitive detection of glucose concentration in both *in vivo* and *in vitro* applications. Unfortunately, the sensitivity and response of the sensor, as a function of nanoparticle geometry and glucose oxidase distribution, is not fully understood, making it difficult to optimize the sensor performance. In this work, we derive an analytical relationship that explicitly correlates sensor performance to the elementary properties of the electrodes and oxidase. The model facilitates predictive design and optimization of nanoparticle-based amperometric biosensors that can eventually be integrated into the wearable platform.

Most glucose sensors are enzymatic, but a non-enzymatic metal oxide-based glucose sensor on a nanostructured substrate is of considerable interest for future always-on wearable closed-loop sensing for hypoglycemia management. Recently, various

research groups have demonstrated that different nanostructured substrates (fabricated by a variety of innovative techniques) boost the sensitivity of non-enzymatic glucose sensor. In this work, we develop a physics-based model to correlate the geometrical and chemical design parameters to the non-linear amperometric response of non-enzymatic glucose sensor on the geometrically complex substrate. Using this model, we can interpret the scattered results in the literature within a common conceptual framework. Our model will predictably improve the design of non-enzymatic glucose sensors for integrating into continuous glucose monitoring system (CGMS) in wearable and implantable platforms.

Enzymatic biofuel (EBFC)-based self-powered sensors represent an interesting class of biochemical sensors as they obviate the need for external power sources thus enabling device miniaturization. While recent efforts driven by experimentalists illustrate the potential of EBFC-based sensors for real-time monitoring of physiologically relevant biochemicals, a robust mathematical model that helps understand the contributions of sensor components and empowers experimentalists to pre-dict sensor performance remains missing. In this work, we provide an elegant yet simple equivalent circuit model that cap-tures the complex, three-dimensional interplay between coupled catalytic redox reactions occurring in an EBFC-based sensor and predicts its output signal with high correlations to experimental observations. Systematic experiments validate the accuracy of the described model. The mathematical model derived in this work can be easily adapted to understand a wide range of two-electrode systems, including sensors, fuel cells, and energy storage devices.

To improve farm-to-folk productivity, we develop design guidelines for roll-to-roll thin-film ion-selective electrode sensors. The sensor detects the local soil nitrate level on demand. The fabrication process involves roll-to-roll (R2R) nano-manufacturing facility which enables high throughput at low cost. We developed a fundamental physics-based model to describe both steady-state response and transient response of ISE sensor. We discover that the conventional logarithmic Nernst relationship in the steady-state can be extended in the time domain. For a thin solid-contact ISE, the

ion-selective membrane thickness plays a significant role due to the accumulation and depletion of target ions in the entire membrane region. We successfully eliminate the effect of ion-selective membrane variation on output emf voltage by image analysis and machine learning methods. We introduce a new graphene-based ISE design to reduce ISE response time and sensor-to-sensor variations.

In addition to sensor performance, the theoretical framework developed in this thesis also focuses on the general reliability issues for the IoT edge-computing electronics in the system integration level. It includes the physics of the multiple degradation mechanisms in harsh environments, such as corrosion assisted by moisture diffusion, device instability due to ion drift, and dissolution of the packaging material in the salty biochemical environment. Wearable and implantable electronic devices are enabling a new generation of customized real-time health monitoring systems. Some of the highest performance systems involve MOSFET-based sensors as well as MOSFET-based digital and analog circuits. Protecting these transistors in a harsh fluidic environment is difficult because the requirement of wearability/flexibility demands ultra-thin encapsulation. The charged ions (such as Na^+) from the body-fluids can diffuse rapidly through the thin encapsulation layer and destabilize the transistors, and render the component nonfunctional. In this paper, we develop an analytical framework and scaling theory for Na^+ penetration into the encapsulation layer of wearable and implantable electronic devices. Coupled with physics of MOSFET degradation, the ion penetration model predicts lifetime of MOSFET-based electronics encapsulated by various types of encapsulating materials. The model is easily generalized to include multiple design parameters, such as stacks of encapsulation layers, encapsulation layer thicknesses, temperature/field dependent ion drift and rate of dissolution of the encapsulation layer, etc. Our simulations and experiments show that 1) a multi-layer encapsulation is essential to achieve multi-objective passivation. and 2) the encapsulation thickness must be optimized by accounting for charged ion penetration and dissolution of the encapsulation layer. Our results can be used to predict the performance degradation and project the lifetime of electronic devices for implantable

and autonomous sensors, providing direction to optimize the design of the protective packaging.

1. INTRODUCTION

1.1 The trend of IoT network

Looking back at the history of humankind in the past century, the advancement of science and technology has greatly improved people's lives: the discovery and cognition of bacteria and viruses, and the large-scale use of antibiotics have greatly increased the control of disease and prolonged the average human life expectancy; breakthroughs in genetic engineering in biology have increased agricultural grain production and fed more populations; the booming development of the semiconductor industry has made it possible for big data processing, computing, and storage to push humans into the information age.

In the near future, the development of Internet of Things (IoT) will closely connect the physical and digital realms, greatly expanding the coverage of information technology. The number of connected devices is expected to exceed 50.1 billion in 2020, almost double the number (28.4 billion) in 2017. The driving force behind this exponential growth comes from two rapidly developing areas: 1) the increasing computation and storage capability at the cloud/server side thanks to Moore's law, and 2) the expansion of edge electronic devices.

On the IoT edge side, electronic devices such as sensors, transistors, energy harvesters, etc. have become increasingly sophisticated and their widespread use is beginning to transform daily life. [1] The trend offers an opportunity to integrate these individual electronic devices into integrated systems for IoT applications such as self-driving cars, smart cities, and smart grids. [2,3] The interconnected electronic systems will be embedded in everyday objects to measure, send, receive, and analyze data. This inter-connectivity would allow one to program the system to optimize power vs. performance trade-off. [4, 5] Specifically, there are two potential areas of applica-

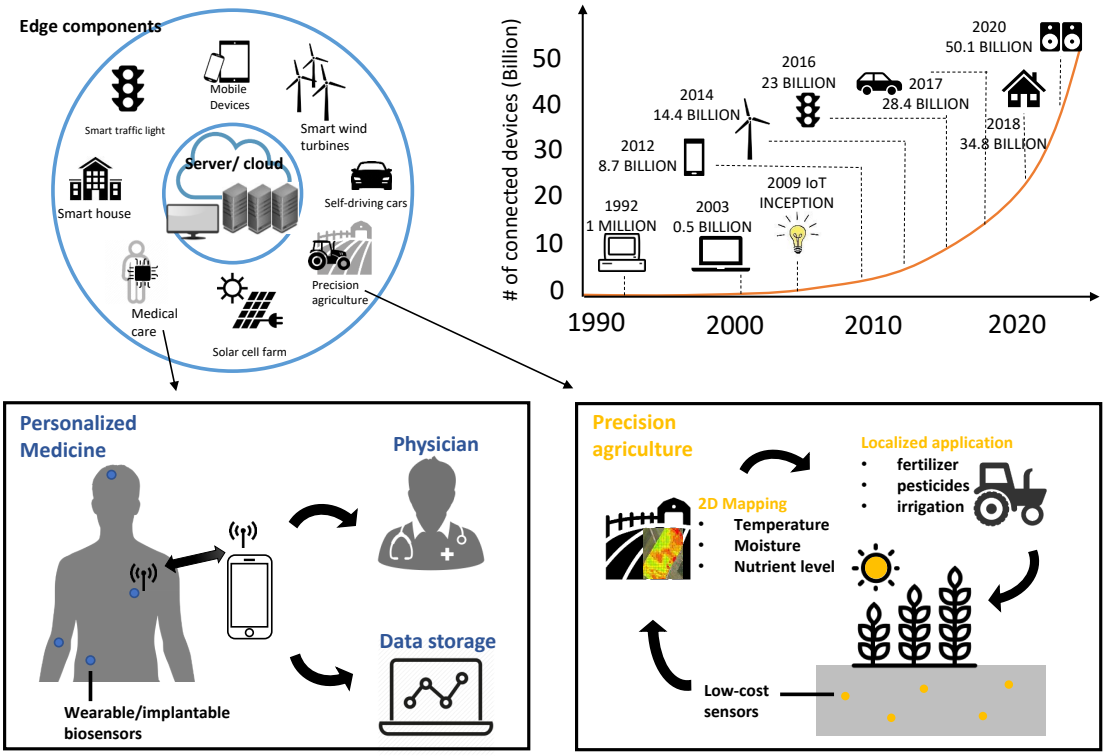

Fig. 1.1.: The Internet of Thing (IoT) network. Cloud computing component vs. edge components. Number or connected devices. IoT application in personalized medicine and precision agriculture.

tions (see Fig. 1.1) where tremendous growth will take place in the coming decades: personalized medicine and precision agriculture.

Personalized Medicine: To combat either chronic physical diseases (e.g., diabetes, epilepsy, nephritis, glaucoma, and, cancer) or mental illnesses (e.g., depression, anxiety disorder, and autism), there is an increasing demand for continuous health monitoring. [6] For this purpose, researchers have developed wearable and bio-implantable systems and these systems are considered reliable tools for long-term health monitoring systems. [7] The application for next-generation bio-implantable systems will not only be restricted to monitoring health condition in a clinical setting

but will also include fitness tracking and preventative health care in everyday life. [8] Furthermore, human body performance evaluation in extreme environments, such as an airman in the fighter aircraft and an athlete during high-pressure games, have emerged as important research topics. [9, 10]

Benefiting from the improvement of semiconductor technology, the electronic sensors can now reliability monitor the full range of physiological indices (e.g., blood pressure, heart beat, blood oxygen saturation). Implementation of the electrochemical biosensors into wearable and bio-implantable systems, however, is still in its infancy stage. [6] Currently, there are two main trends in the development of next-generation electronic body monitoring system: 1) liberate the massive monitoring instruments from the lab into portable lab-on-a-chip system, and 2) introduce the ability to test for multiple analytes. [11] Both of them require significant advances in electronic sensor technology.

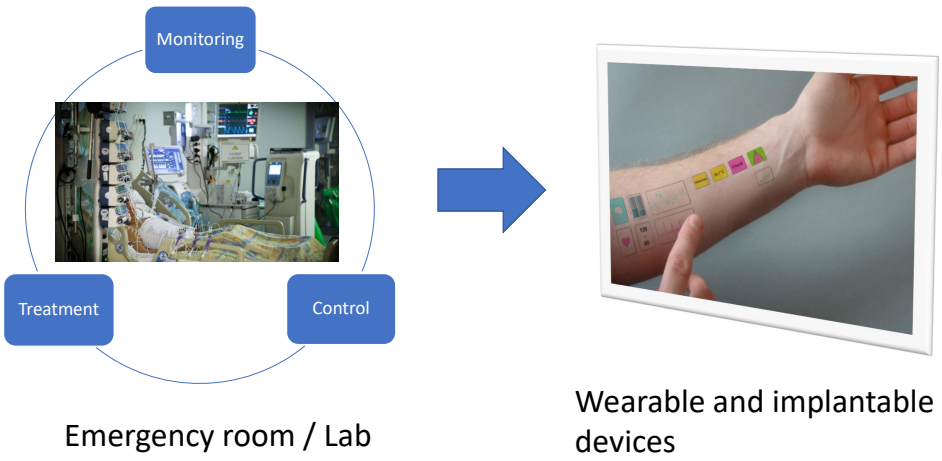

Fig. 1.2.: IoT medical care application: liberating the sensors from lab to lab-on-a-chip wearable electronic devices.

Precision Agriculture: Nowadays agriculture has evolved into an incredibly sophisticated industry. A new concept called precision agriculture is the critical component in the wave of modern agriculture revolution. [12] The objective of precision agriculture is to optimize crop returns while preserving resources. [13] To achieve this objective, people need customized devices to precisely understand and improve plants for the whole farm management. A modern IoT network can connect all those customized devices together. This closed-loop IoT network must be completed by sensors that can continuously monitor and send data to the farmers, chemical vendors, and agronomists. The data include information on plant health status as well as biophysical parameters indicating the need for inputs, such as soil pH level, nitrate level, relative humidity, number of fungus/bacteria, etc. [14,15] In the back end, the network analyzes the data and then deliver on-demand nutrition/pesticide to the plant, or precisely control the irrigation systems.

1.2 The evolution of modern electrochemical biosensors

Modern electrochemical biosensors, integrated with nanotechnology, can detect tiny elements such as chemical molecules, bacteria, and mycotoxin in low concentration. Therefore, it is particularly attractive for the IoT network. [16] Also, modern material technologies offer the possibility to implement sensors in an all-organic approach. Hence, the sensor can be more functional by the integration of environmentally friendly and biocompatible material with specific properties, making the tailor-made design possible for low-cost, fully-integrated biosensors operating uniquely in the field of medical care and precision agriculture [17].

Based on the detection mechanism, modern electrochemical biosensors could be categorized into four groups: amperometric, potentiometric, impedance, and optical.

Amperometric sensors. This type of sensor detects the concentration of a chemical species by measuring the current. The target analytes for this detection mechanism are usually charged neutral (glucose, lactate, etc.). The current comes

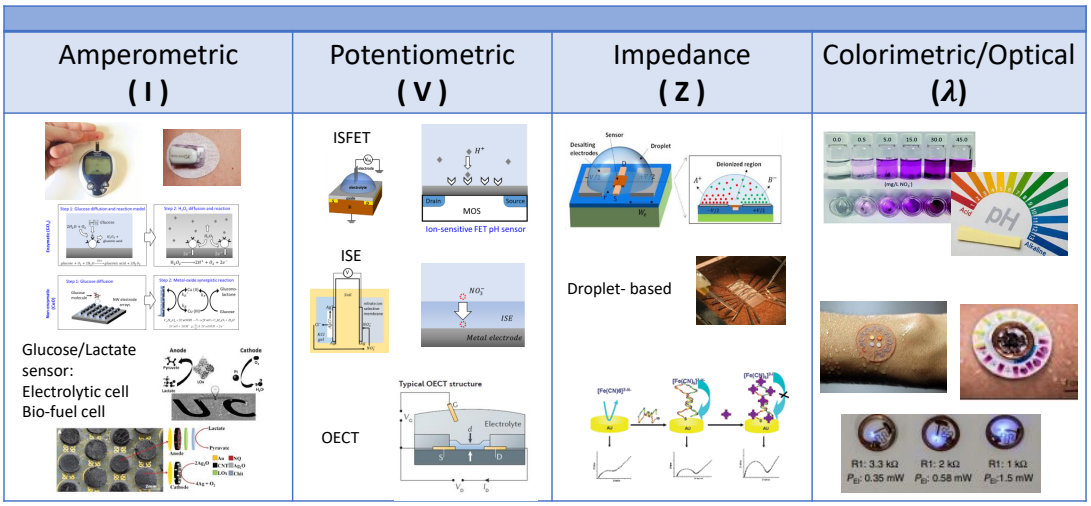

Fig. 1.3.: Four fundamental categories of modern electrochemical biosensors

from the electrons generated by specific electrochemical oxidation/reduction reactions of either the initial analyte or the secondary by-products.

A typical amperometric sensor uses the three-electrode setup shown in Fig.4. A voltage bias is applied between the working and reference electrode during measurement to maintain a constant potential. The current passes through and is measured between the working electrode and the auxiliary electrode (sometimes referred to the counter electrode).

The amperometric sensors offer many advantages: the specificity of the electrochemical oxidation/reduction reaction makes them more selective compared to other sensing techniques. Unlike potentiometric sensors, the response of the amperometric sensor is not limited by charge screening. Amperometric sensors are widely used in environmental, clinical, and industrial applications.

An important application of amperometric biosensors involves glucose detection. Commercial glucose sensors depend on the amperometric method to measure the glucose level in a blood sample for diabetes control. As shown in the Fig. 1.5 (a), a

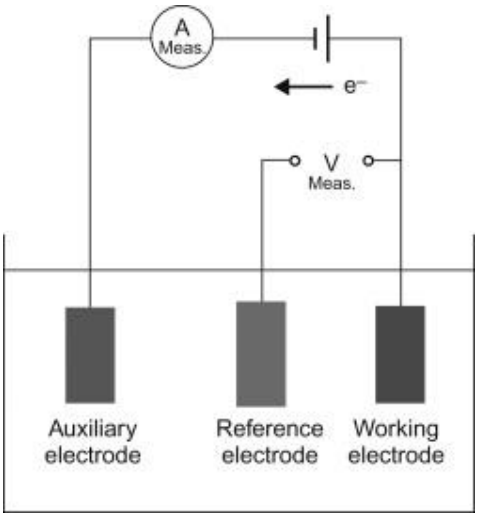

Fig. 1.4.: The three-electrode measurement setup for amperometric sensors. [18]

chain of redox reactions happens on the working electrode. Enzymatic glucose oxidase (GOx) catalyzes the reaction between glucose and oxygen to produce hydrogen peroxide (H_2O_2) as an intermediate product. The applied voltage extracts electrons from H_2O_2 and generates the output current signal.

For IoT personalized medicine applications, several design limitations need to be resolved before the amperometric sensors can be fully integrated: First, GO_x activity depends sensitively on the ambient temperature. The degree of temperature control needed is incompatible with long-term bio-implantable applications. Second, the consumption of O_2 during glucose oxidation causes the sensor reading to drift, requiring frequent calibration. Finally, the reaction by-product H_2O_2 is potentially harmful to the human body.

In chapter 2, 3, and4 of this thesis, we will introduce three novel amperometric sensor designs that overcome the drawbacks of conventional amperometric sensor: nano-particle based enzymatic glucose sensor (Fig. 1.5 (a)), non-enzymatic glucose sensor(Fig. 1.5 (b)), and enzymatic biofuel cell (EBFC) based amperometric sensor (Fig. 1.5 (c)).

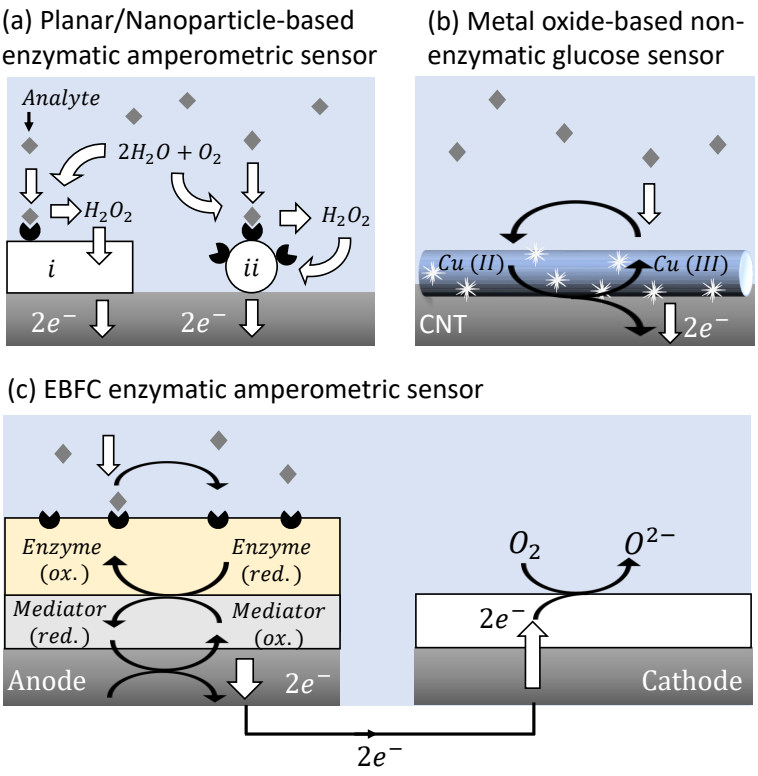

Fig. 1.5.: Schematic illustrations of the working mechanism of (a) (i)Planar/(ii)Nanoparticle-based enzymatic glucose/lactate sensor. GO_x/LO_x works as enzyme and H_2O_2 works as electron mediator (b) Metal oxide-based non-enzymatic glucose sensor. (c) Bio-fuel amperometric enzymatic glucose/lactate sensor.

Potentiometric sensors. In contrast to the amperometric sensor, a potentiometric sensor is a type of chemical sensor that used to determine the concentration of species from the voltage response. For this detection mechanism, the target analytes are normally charged molecules such as DNA, protein, and ions. These sensors measure the electrostatic potential (or electromotive force EMF) generated by the charged species under zero-current conditions.

There are several types of potentiometric sensors. One typical example called ion-sensitive field effect transistor (ISFET) combines the chemical sensor technology with

CMOS technology. The structure of ISFET is like conventional MOSFET except that the metal gate of MOSFET is replaced by a liquid gate. When the charged target species in the measuring solution combines with the selective molecules (antibody, enzyme, etc.) on the liquid gate, the equivalent gate bias changes and the source to drain current I_D reveals the analyte concentration accordingly.

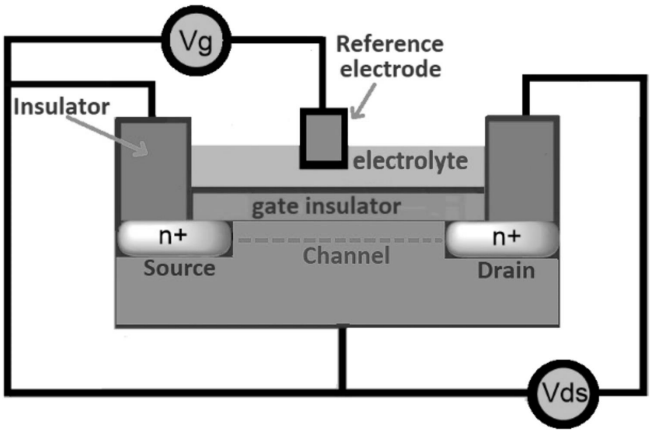

Fig. 1.6.: Schematic illustration of the working mechanism of ion-sensitive FET. Figure has been regenerated from [19]

In chapter 5 and chapter 6 of this thesis, we are going to investigate the sensing mechanism and performance limit of another type of potentiometric method: ion-selective electrode (ISE) sensor. Because of the simplicity of the sensor setup, ISE is more widely used for IoT integrated systems.

Impedance sensors. Electrical impedance-based sensor determines the analyte concentration from the impedance spectroscopy. The basic idea behind this approach is to bias the sensor electrode with a small AC signal and to observe electrode response. When the analyte is captured by the probe of the impedance sensor, the impedance of the electrode-solution interface changes. [20, 21] Impedance biosensors are commonly used to detect larger analytes, such as bacteria, cocaine, etc.

Optical colorimetric sensors. Another group of modern biosensors relies on optical detection mechanism. "Traditional in-lab optical detection is based on the measurement of luminescent, fluorescent, and colorimetric signals produced by the interaction of microorganisms with the analytes." [22] The observed optical signal is related to the concentration of target analyte. Among different optical technologies, the colorimetric sensing techniques recently have received a lot of attention for IoT applications for their simple, battery-free, and inexpensive measurement setup. The conversion of a chromogen substrate into a colorful compound can be either distinguished by eye or other quantitative image processing techniques such as smartphone app that analyzes the captured image of the color change.

1.3 The examples of modern sensor integration for IoT applications

In recent years, a lot of research groups have integrated a wide variety of modern biosensors into a single electronic system. The system usually contains the following functional units as showing in Fig. 1.7: multi-spectral sensors adapted from different biosensing techniques, peripheral circuits for signal processing, power and energy harvesting systems, wireless data transmission unit, etc.

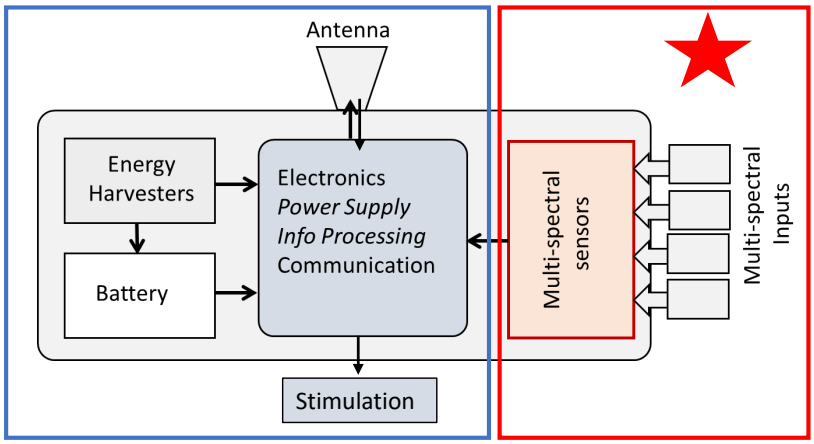

Fig. 1.7.: Schematic illustration of closed-loop integrated sensor system

Gao et al. [23] introduced the most influential sensing electrode technology with the Fully Integrated Sensor Array (FISA) wristband (Fig.1.8 (a)). This device is able to simultaneously measure the sweat concentration of glucose, lactate, Na^+ and K^+ by fitting two amperometric sensors and two potentiometric sensors into a single wearable system. In addition to the sensing electrodes, the system also includes a temperature sensor, a power supply unit, an on-board amplifier, an analog-to-digital converter, and a wireless data transmission unit.

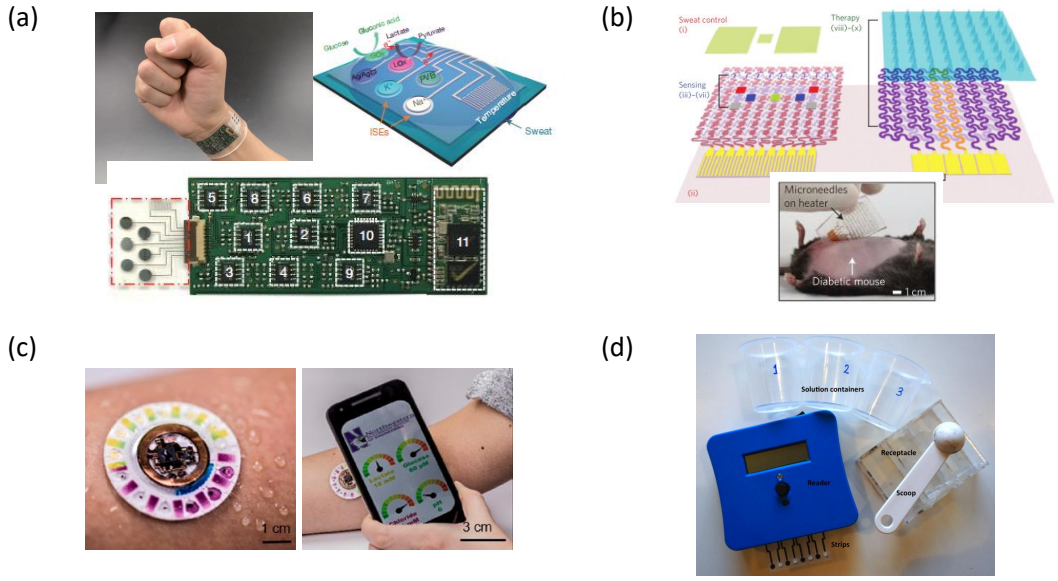

Fig. 1.8.: Examples of modern sensor integration for IoT applications. (a) Fully Integrated Sensor Array (FISA) wristband [23]. (b) A graphene-based electrochemical device with thermo-responsive microneedles for diabetes monitoring and therapy [24]. (c) Battery-free, skin-interfaced microfluidic/electronic systems [25]. (d) Integrated point-of-use soil testing system [26].

As shown in Fig. 1.8 (b), Lee et al. [24] introduce a thin-film wearable patch consisting of a heater; temperature, humidity, glucose, and pH sensors. The patch also includes polymeric microneedles that can be thermally activated to deliver drugs. Lee's group have successfully demonstrated the *in vivo* test to thermally actuate and

deliver Metform to reduce the diabetic mice's blood glucose level in a closed feedback loop.

Bandodkar et al. have demonstrated a battery-free, wireless electronic sensing platform that simultaneously monitors sweat rate/loss, pH, lactate, glucose, and chloride shown in Fig. 1.8 (c). The prototyped device integrates chronometric microfluidic platforms with embedded colorimetric assays and potentiometric ion-selective sensors. One highlight of this work is that the potentiometric ion-selective sensors are inspired by the biofuel cell technology where no external power source is required. "This new design combines the advantages of electronic and microfluidic functionality in a platform that is significantly lighter, cheaper, and smaller than its alternatives." [25].

Rosenberg et al. have developed an integrated point-of-use soil testing system, including a set of disposable solid-state ion-selective electrode strips to detect the potassium and chloride level in the soil [26]. As shown in Fig. 1.8 (d), a handheld electrochemical reader is designed to record the measurement data. This system could be deployed for soil nutrient management in resource-limited environments.

1.4 New challenges facing modern electrochemical biosensors for IoT system-level integration

Even though many promising integrated IoT sensor systems has been demonstrated, the design of biosensors for IoT systems must solve the following common challenges before they can be successfully commercialized:

1. Optimization of sensor performance. Biosensors must continuously sample the comparatively weak biochemical signals. In contrast, environmental variability is expected to increase noise. Hence, sensors must be designed to achieve the following sensor performance requirements:

    (a) High sensitivity. The sensitivity of a biosensor is defined as the relative change of sensor output signal corresponding to the change of target molecule concentration. Mathematically, the sensitivity can be calculated

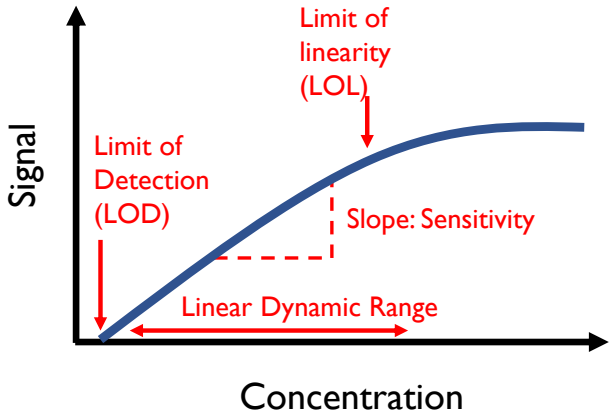

Fig. 1.9.: Schematic illustration of a typical steady-state response and the performance characterization metrics of an electrochemical biosensor

as the slope of the sensor steady-state response. High sensitivity ensures a strong sensor response to the target analyte signal in the environment.

(b) Good selectivity. Selectivity denotes the ability of a sensor to detect the desired target in the presence of various other secondary analytes. In a biofluid or soil, there are many types of unwanted molecules. Selecting the target analyte and filtering out the other analytes from the operating environment is critical to guarantee a large signal to noise ratio for IoT application.

(c) Wide linear dynamic range. Linear dynamic range is the maximum linear response of a sensor where the sensitivity remains a constant. For any particular IoT application, the concentration range of the target analyte should fall within this linear dynamic range.

(d) Limit of detection. The limit of detection is the lowest quantity of the analyte that can be detect by a sensor. Under certain IoT edge detection conditions, the analyte concentration could reduce to micromolar or pico-

molar. The reduction of the detection limit is another critical design goal for modern electrochemical biosensors.

2. Reliability. The sensors need to be either implanted in a harsh environment (e.g., soil, human body) for a long period of time. The stability of the biosensor is a critical design criterion due to the changing operating environment, such as considerable temperature variation, different pH, and high relative humanity.

3. System integration. In both personalized medicine and precision agriculture, it is difficult to integrate all the closed-loop functionalities, such as sensing, wireless signal transmission, low power operation, and energy harvesting shown in Fig. 1.7, within a single edge computing electronic device. Moreover, the sensors must have a quick response time to be integrated with other elements in the IoT network.

1.5 Outline of thesis

In this thesis, we are going to focus on several novel modern electrochemical biosensor designs which are considered as promising candidates for IoT personalized medicine and precision agriculture applications. We will develop physics-based methodologies and predictive modeling framework to model and simulate the performance of those new sensors and to overcome the challenges mentioned above. Our research work will establishes a comprehensive and rigorous framework that covers from the device level to system level biosensor design. In analogy to how device physics of transistors is connected to IC design in electronics, the framework developed in this thesis will link the device level characteristics to the short-term sensor performance as well as the long-term system-level issues. Specifically, we will focus on three main topics:

1. Amperometric sensors (chapter 2, 3, and 4): By coupling electrical and mass transfer simulations, the modeling frameworks will clarify the fundamental

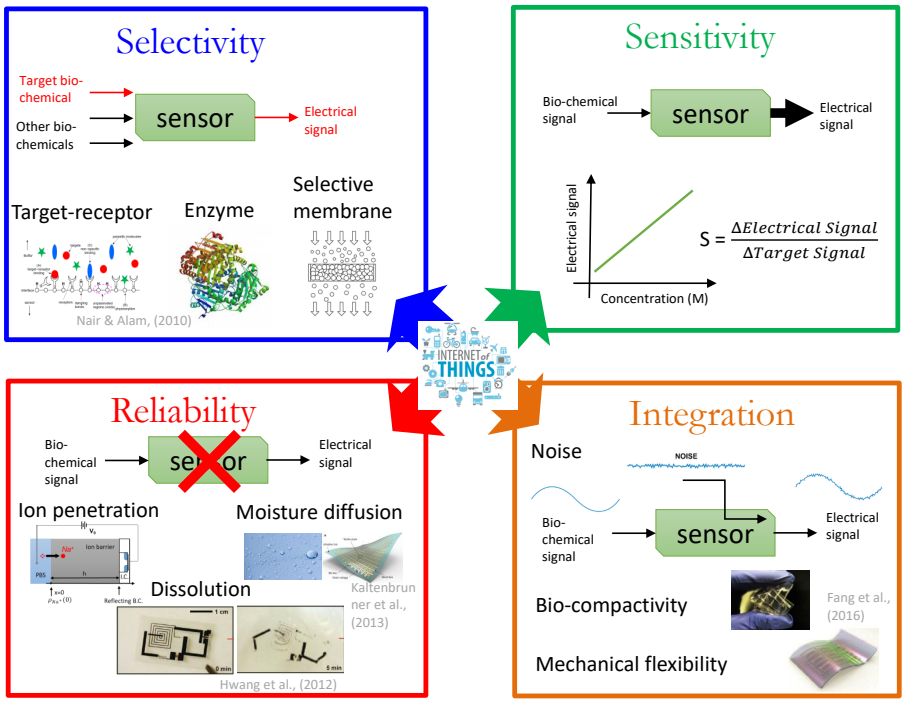

Fig. 1.10.: New challenges facing modern sensor for IoT system: selectivity, sensitivity, reliability, and integration issues.

physics of bio-molecule diffusion and reaction process. They will pave the path for the development of novel micro/nano-structured electrodes to enhance the sensitivity, the spatial resolution, and temporal resolution of sensors.

2. Potentiometric ion-selective sensor (chapter 5 and chapter 6): We will apply the physical models of biosensors to establish design guidelines for thin-film based solid-contact ion-selective electrode (ISE) sensors. Our research work will help to develop more economical printed thin-film foldable nitrate sensors to improve the farm-to-folk productivity related to precision agriculture.

3. Reliability of IoT electronics in a harsh environment (chapter 7).

The detailed outline of each chapter is as follows:

In chapter 2, the goal is to identify and quantify the design parameters and to improve the performance of enzymatic amperometric glucose biosensors with micro/nano-scale structured electrode. We will develop a new analytical model to capture the essence of the NPs array electrode structure and to correlate its steady-state current response explicitly to geometrical, physical and chemical parameters. The conceptual approach of breaking the complex reaction-diffusion kinetics into a series of elemental steps, describing each step analytically by concepts such as diffusion capacitance, and finally integrating the elements into a simple formula will solve the original system integration problems.

In chapter 3, we will focus on a non-enzymatic amperometric glucose detection strategy. This detection strategy shows higher sensitivity and better thermal stability, making it suitable for implantable sensors for long term real-time monitoring. We will develop a new analytical model to capture the essence of the non-enzymatic glucose sensors. The model will quantify the effectiveness of various design parameters and provides guidelines to improve the overall performance of metal oxide-based non-enzymatic glucose sensor.

In chapter 4, we will investigate self-powered amperometric sensors based on enzymatic biofuel cell (EBFC). This type of sensor draws much attention in the biosensor field for their applications in energy-limited settings including wearable and implantable technology. We will apply an equivalent circuit method to self-consistently include the impact of both anode and cathode reactions. The equivalent circuit model can be easily adapted to solve the problems in other two-electrode redox amperometric systems, such as fuel cells, and other energy storage systems.

In chapter 5, we will develop design guidelines for roll-to-roll thin-film ion-selective sensors to improve farm-to-folk productivity. The sensor detects the local soil nitrate level on demand and sends the data wirelessly to the server. The thin-film sensor is fabricated by a unique roll-to-roll (R2R) nano-manufacturing facility which enables high throughput at low cost. The flexible substrate is processed in a series

of multi-layer manufacturing technologies including roll-to-roll metal inject printing, ellipsometry, slot die/micro-gravure coating, and pulsed laser processing. To characterize the sensor performance, we will develop a fundamental physics-based model for this thin-film nitrate sensor. This chapter mainly focuses on the modeling of the solid-contact ISE sensor.

Chapter 6 will focus on the application of physics-based model developed in chapter 5 to solve for more general ISE integration problems: the transient response, sensor-to-sensor variations, and other issues that associated with the non-ideal performance of solid contact ISE. Based on our theoretical study, we will also provide new design strategies to improve both short-term and long-term performances.

In chapter 7, we will design smart encapsulants to precisely control the lifetime of IoT edge computing electronics in a harsh environment. We will introduce bi-layer or tri-layer encapsulant designs for multi-target (e.g., ion, humidity) protection. By developing both numerical and analytical frameworks for the multi-objective transport process in the encapsulation layer, we can accurately predict the lifetime of encapsulated MOSFET-based electronic devices in a severe environment. The physics-based transport model helps better understand the performance degradation of edge IoT electronics in a harsh environment. Our purposed multi-layer encapsulant design could protect the embedded electronic devices from various failure factors.

Finally, we will conclude in chapter 8 by summarizing the key conclusions and suggesting opportunities of future works.

2. NANOPARTICLE-BASED AMPEROMETRIC GLUCOSE BIOSENSORS

2.1 Motivation

For the 422 million people worldwide who have diabetes, the glucose sensor is a life-changing technology. [27] After Clark and Lyons developed the first glucose enzyme electrode in 1953 [28], different research groups and companies have developed related technologies for numerous applications ranging from diabetes control to food analysis. In 1973, Guilbault and Lubrano introduced amperometric glucose sensor by measuring the charge current from the hydrogen peroxide (H_2O_2) redox reaction [29]. In 1975, YSI Inc. launched the first commercial glucose sensor system. In 1987, Medisense Inc. launched the first personal glucose sensor. Cygnus Inc. developed a wearable non-invasive glucose monitor in 2000 [30]. Most diabetics monitor the glucose in patient's blood by pricking their fingers many times each day—a necessity because the level of glucose fluctuates in response to meals, exercise, and other everyday activities. Even continuous glucose monitors, which use electrodes that sit under the skin, require multiple daily finger pricks for calibration. Today, numerous research groups are working in the direction that integrates the glucose sensors into complex multi-functional systems that detect glucose concentration in sweat, saliva [23] and tears [31], with the hope of obviating the need for repeated needle pricks in diabetes.

In 2014, both Google and Swiss pharmaceutical giant Novartis International announced to design, develop, and commercialize smart contact lens with a microsensor that continuously measures glucose levels. [32] The smart lenses benefited from new kinds of flexible electronics that are microscopic or semitransparent. Typical tear

[0]The content of this chapter is primarily taken from a published paper: X. Jin, T. Fisher, and M. A. Alam, "Generalized compact modeling of nanoparticle-based amperometric glucose biosensors." *IEEE Transactions on Electron Devices*, 63, no. 12 (2016): 4924-4932.

glucose levels are on the order of 0.1 to 0.6 mM, [33] while glucose levels in the blood range from about 4 to 6 mM. [34, 35] Therefore, the glucose sensor in the smart contact lens requires much better performance compared to existing commercial blood glucose sensor.

Recently, various nanostructures have been utilized to enhance the performance of glucose sensors. In particular, nanostructured platinum (Pt) nanoparticle (NP) glucose sensors have shown promising performance [36, 37], especially at detecting relatively low glucose concentration. Such results are hardly unexpected because NPs are less susceptible to classical diffusion limits compared to planar sensors [38]. Moreover, the nanostructured substrate such as carbon-nanotube and graphene is more suitable for the mechanical flexibility implantable requirement. All those features enable the NP-based glucose sensor to become a potential candidate for future sensor integration in a wearable platform such as the smart contact lens.

2.2 Background: enzymatic NP amperometric glucose sensor

As shown in Fig. 2.1 (a), Pt NP glucose sensors utilize an array of Pt NPs as the working electrode. Glucose oxidase (GO_x) enzymes are immobilized on each NP surface. GO_x catalyzes the reaction between glucose and oxygen (Steps 1 and 2 in Fig. 2.1(c)) to produce hydrogen peroxide (H_2O_2) as a reaction product, i.e.,

$$D - glucose + O_2 + H_2O_2 \quad \xrightarrow{GOx} \quad D - gluconic\ acid + H_2O_2 \tag{2.1}$$

A fraction of H_2O_2 react with the Pt NPs (step 3 in Fig. 2.1 (c)), while the remainder diffuses into the bulk solution (step 4 in Fig. 2.1(c)).

$$\mathrm{H_2}O_2 \qquad \longrightarrow \qquad 2H^+ + O_2 + 2e^- \tag{2.2}$$

The reaction produces the electrical charges in individual NP, integrated by the 2D and 1D substrates such as graphene, carbon nanotubes, see Fig. 2.2 (a) and (b). The substrate plays an active role in dictating the geometrical arrangement of

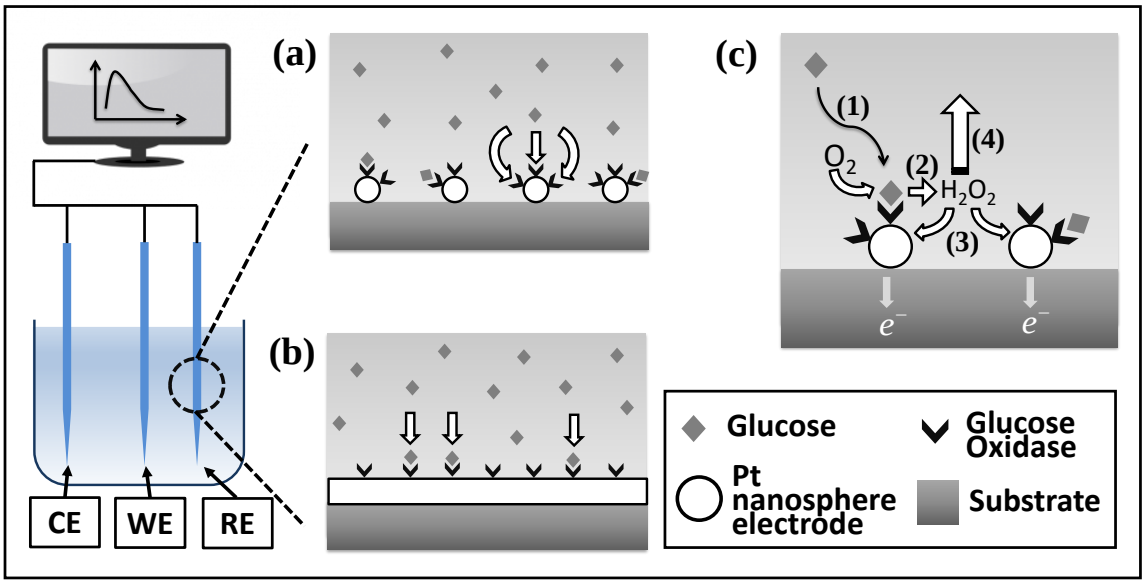

Fig. 2.1.: Schematic side view of (a) A Pt nanoparticle-based amperometric glucose biosensor and (b) A planar amperometric glucose biosensor. (c) The Pt nanosphere electrodes (circles) are located on top of sensor substrate material surface. Glucose oxidase (black) is immobilized on each electrode surface. (1) Glucose molecules (diamonds) diffuse in solution and are captured by the glucose oxidase enzyme. (2) The reaction of glucose with oxygen generates the intermediate product H_2O_2, which can either (3) react on the electrode surface and produce charged species or (4) diffuse into the solution.

NPs. The NPs can be distributed randomly on 2D substrates such as multilayered graphene petal nanosheets (MGPN), see Fig. 2.2(b); while in Fig. 2.2(a), they aggregate like 'pearls on a chain' along 1D carbon nanotube (CNT) chains. The details of the fabrication process are discussed in prior work [39, 40]. Such sensor structures offer the advantage of large electrode surface-to-volume ratio, unique molecule capture geometry, short response time and enhanced mass transport and electrochemical response [41].

A Pt NP amperometric sensor differs fundamentally from a classical sensor as follows:

1. The curvature of classical sensors is large enough and the glucose concentration is typically high enough to justify the assumption of 1D diffusion of glucose toward the sensor surface [42]; this approximation does not hold for NP amperometric sensors.

2. Glucose oxidase molecules in classical sensors are embedded within a membrane so that the reaction is distributed within the membrane volume. For NP sensors, the oxidation occurs directly on the NP surface. The two processes have very different kinetic response characteristics.

3. Most models of classical sensors presume that H_2O_2, once generated, is converted fully into the current. In other words, Eq. 2.2 is 100 percent efficient. While this may be true for classical sensors, the assumption has not been validated for NP-sensors.

These geometrical and physical differences suggest that it would be inappropriate to use classical expressions to describe NP sensors. Moreover, the classical models are often numerical – making it difficult to extract the exact functional dependencies among various variables, such as electrode geometry, distribution of enzyme reaction centers on the NPs and the diffusive cross-talk of the target molecules among the neighboring NPs. The purpose of this chapter is to develop a new analytical model that captures the essence of the glucose sensor with NPs array electrode structure and to correlate its steady-state current response explicitly to geometrical, physical and chemical parameters. The conceptual approach of breaking the complex reaction-diffusion kinetics into a series of elemental steps, describing each step analytically by concepts such as diffusion capacitance, and finally integrating the elements into a simple formula to solve the original problem, is general and can be used as a template to solve a broad range of other biophysical problems.

2.3 Diffusion and reaction of glucose molecules:

2.3.1 Diffusion of glucose molecules to the Pt NPs surface

Mass transportation of glucose in the solution can be described by classical diffusion equation [43]:

$$\frac{dG}{dt} = D_G \nabla^2 G \tag{2.3}$$

where G is the glucose concentration and D_G is the glucose diffusion constant. The GO_x is immobilized only onto the Pt NP surface. Therefore, the enzymatic glucose oxidation reaction occurs only on the NP surface. The surface reaction rate for glucose (R_G) is directly proportional to the enzyme surface density (E_0), glucose concentration at the sensor surface (G_S), and the forward reaction constant k_f, so that:

$$R_G = k_f \cdot E_0 \cdot G_s \tag{2.4}$$

A direct 3D numerical solution of Eqs. 2.3 and 2.4 for the electrode geometries shown in Fig. 2.2(c) and (e) is possible, but it would not be very useful as a tool for interpretation and optimization of sensor response. Two approximations simplify the problem dramatically and make it amenable to analytical solution:

1. First, faithful to the original geometry, the electrodes in Fig. 2.2 can be approximated as a periodic structure shown in Fig. 2.2 (d) and (f). Specifically, with a low density of NPs on 1D or 2D substrates (**case 1**), cross diffusion among the NPs can be neglected because the capture of glucose molecules by one NP is unaffected by its neighbors. Therefore, we model these Pt NP electrodes as isolated nanoparticles within a unit cell shown in Fig. 2.2 (c). At higher densities, the NPs on a 2D substrate (**case 2**) can still be approximated as being arranged in a periodic array, but cross-diffusion is important and cannot be neglected. At even higher densities of NPs on a 2D substrate (**case 3**), the arrangement of the particles begins to resemble a fractal surface, which is accessible to analytical

techniques, as described by Nair *et al.* [44] On the other hand, for high densities of NPs arranged onto relatively low-density 1D substrate (such as Carbon nanotube **case 4**), the particles are arranged densely along 1D chains, as shown in Fig. 2.2 (d). Here, the proximity of the NPs encourages cross-diffusion among the NPs in one Cartesian direction. At very high densities, the configuration is indistinguishable from **case 3** discussed above. Among the four cases, experiments reported in Claussen *et al.* [39] resemble **case 1** and **case 4**, respectively. Therefore, we will focus on developing the model for these configurations. Once the basic model is understood, the generalization to other cases should be intuitive.

2. Steady-state diffusion can be solved analytically by recognizing that it is isomorphic to the Laplace's equation for electrostatic problems, thus allowing us to use the notion of diffusion-equivalent capacitance. Briefly, at steady-state, the glucose diffusion equation reduces to $D_G \nabla^2 G = 0$, which has the same form, mathematically, as the Laplace's equation, $\epsilon \nabla^2 \phi = 0$ [45]. The solution of one equation can be mapped to that of the other by recognizing the mathematical equivalence of the electrostatic potential ϕ to the glucose concentration G and the permittivity ϵ to the diffusion coefficient D_G. Similarly, one can define an analogous parameter to electrostatic capacitance (C) called 'diffusion equivalent capacitance' (C_D) related to the solution of the diffusion equation [38]. Note that C_D does not have the same units as electric capacitance, but does have a similar functional form.

With these two approximations, we are ready to solve the diffusion Eqs. 2.3 and 2.4 for the electrode geometry shown in Fig. 2.3(c) and (d). The glucose diffusion fluxes J_G^{iNP} and J_G^{cNP} (in units of mol·m$^{-2} \cdot s^{-1}$) towards the sensor electrode surface in isolated NP (**iNP, case1**) and chain-NP (**cNP, case4**) limits can be represented as:

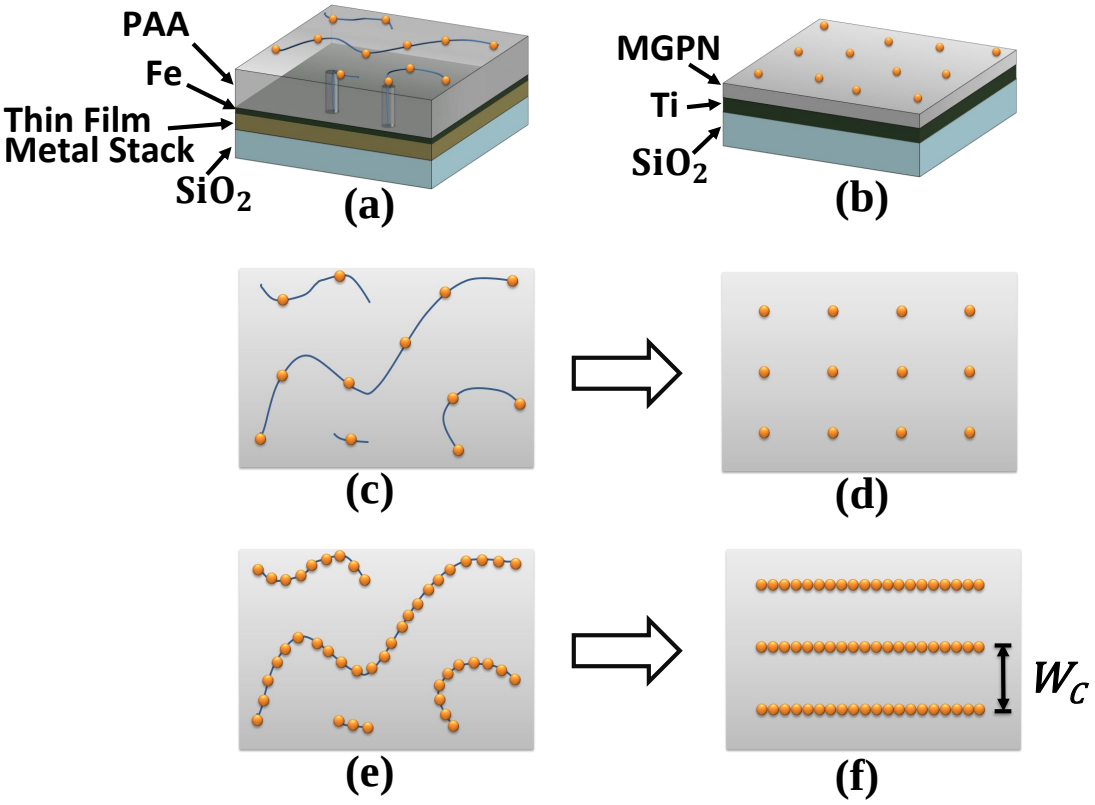

Fig. 2.2.: Schematic view of Pt NP on (a) carbon nanotube(CNT) tethered amperometric substrate and (b) multilayered graphene petal nanosheet(MPGN) substrate. The low-density electrodes in (c) can be modeled as an equivalent nanosphere array in (d). The high-density electrodes in (e) can be modeled as nanowire arrays in (f).

$$J_G^{iNP} = C_{iNP} \cdot \frac{(G_0 - G_S^{iNP})}{4\pi r_{Pt}^2} \tag{2.5}$$

$$J_G^{cNP} = C_{cNP} \cdot \frac{(G_0 - G_S^{cNP})}{2\pi r_{Pt} l} \tag{2.6}$$

where C_{iNP} and C_{cNP} are the diffusion equivalent capacitances, G_0 is the glucose concentration in the solution far from the sensor surface, G_S^{iNP} and G_S^{cNP} are the glucose concentrations near the sensor reaction center; r_{Pt} is the radius of nanosphere.

The glucose flux is normalized either by the area of the individual spheres (iNP) or that of a close-packed nanosphere chain (cNP), behaving as a cylinder of length l.

Because the glucose oxidase enzyme molecules are randomly immobilized on the Pt sphere surface, a simple absorption sphere/cylinder model does not fully capture the physics of diffusion. We must instead model the individual spheres (radius r_{Pt}) decorated by N disk-like absorbers (radius r_{ez} and thickness t_{ez}), where $r_{ez} << r_{Pt}$ [43]. We assume that the distance between each enzyme absorber (of the order of tens nanometers) is larger than their radii (typical value: 4 nm) but is smaller than the radius of nanosphere/nanowire (typical value: 75nm). As glucose molecules diffuse in solution from large distances, they resolve the sensor geometry only as a classical sphere/cylinder. As the molecules diffuse closer to the surface, they can resolve the disk-like absorbers immobilized onto the NP surface. Over all the diffusion equivalent capacitance reduces to [43, 46]:

$$C_{iNP} = \frac{4\pi D_G \cdot r_{Pt}}{1+(\pi \cdot r_{pt})/(N \cdot r_{ez})} \tag{2.7}$$

$$C_{cNP} = \frac{2\pi D_G \cdot l}{ln\left(\frac{sinh\left(\frac{2\pi(\sqrt{2D_G t}+r_{Pt})}{W_c}\right)}{sinh\left(\frac{\pi \cdot r_{Pt}}{W_c}\right)}\right) + \frac{\pi l}{2N \cdot r_{ez}}} \tag{2.8}$$

where N is the number of disk-like absorbers, l is the length of each nanowire and W_c is the pitch in between. Note that all the parameters are physical and readily determined from independent experiments. At steady state, the reaction rate balances the diffusion flux. By equating Eqs. 2.4 and 2.5 or Eqs. 2.4 and 2.6, one obtains the steady-state glucose concentration at the surface of the NPs:

$$G_S^{iNP} = \frac{G_0}{1 + (k_f \cdot E_0 \cdot 4\pi r_{Pt}^2)/C_{iNP}} \tag{2.9}$$

$$G_S^{cNP} = \frac{G_0}{1 + (k_f \cdot E_0 \cdot 2\pi r_{Pt} l)/C_{cNP}} \tag{2.10}$$

The model neglects second-order effects such as the size distribution and spatial randomness of NPs and GOx. We have also neglected diffusion distortion by the sub-

strate and cross-diffusion of glucose among neighboring NPs, which are simplifications of a complex environment whose reasonableness can be assessed with experimental validation of the model predictions.

2.3.2 Glucose oxidation and current generation

The H_2O_2 produced by the glucose reaction on individual nanosphere surfaces must now diffuse and react with Pt to generate useful signal current. Assuming sufficient supply of oxygen, we can use Michaelis-Menten kinetics [47] to model the glucose oxidation process. In steady state, the magnitude of the H_2O_2 generation flux can be expressed as:

$$J_{H_2O_2} = \frac{k_c E_0 G_s}{K_M + G_S} \tag{2.11}$$

where k_c is the catalytic rate constant, E_0 is the enzyme surface density, K_m is the Michaelis-Menten constant and G_s is glucose concentration at the surface, obtained from Eqs. 2.9 and 2.10. Eq. 2.11 provides an explicit solution of the H_2O_2 flux generated as an explicit function of the sensor parameters.

2.4 Self-,cross-, and bulk diffusion of hydrogen peroxide

Hydrogen peroxide generated in the preceding reaction will now diffuse in three dimensions into the solution until it reacts with the exposed Pt surface. The reaction could either take place on the same NP from which peroxide was generated (self-diffusion) or occur on a neighboring NP (cross- or mutual diffusion). The remaining fraction will be lost to the bulk solution, unreacted and swept away by the fluid flow. Although the self- and cross-diffusion problems are complex, the concept of diffusion equivalent capacitance solves the problem of H_2O_2 diffusion as efficiently as it did for glucose diffusion. Specifically, the ratio of H_2O_2 flux moving toward and reacting on the sensor surface compared to total flux can be expressed as:

$$J_{in} = \frac{C_{in}}{C_{in} + C_{out}} \cdot J_{H_2O_2} \tag{2.12}$$

where C_{in} is the sensor self-capacitance, and C_{out} is the diffusion equivalent capacitance in the solution.

Isolated NP Limit. The hypothetical sphere (dashed line shown in Fig. 2.3(b)) with radius of $r_{Pt} + t_{ez}$ acts as a source of H_2O_2 within each unit cell. Here, t_{ez} is the average thickness of each GOx enzyme molecule immobilized on the NP surface. At steady state, the cross-diffusion of H_2O_2 fluxes from neighboring NPs cancel each other, so that the net flux at unit cell side boundary is zero. The H_2O_2 molecules, however, can escape the system through the unit cell top boundary. Therefore, the self-capacitance $C_i n^{iNP}$ can be viewed as the capacitance between shell of radius $r_{Pt} + t_{ez}$ and the inner sphere; while the bulk diffusion capacitance C_{out}^{iNP} is defined as the capacitance between the source shell and the unit cell top absorbing boundary, succinctly described by Karmalkar et al. Therefore, C_{in}^{iNP} and C_{out}^{iNP} are given as:

$$C_{in}^{iNP} = \frac{4\pi D_{H_2O_2}}{r_{Pt}^{-1} - (r_{Pt} + t_{ez})^{-1}} \tag{2.13}$$

$$C_{out}^{iNP} = \frac{r_{Pt}^2 D_{H_2O_2}}{H} \cdot \zeta \tag{2.14}$$

where H is the height of the unit cell, and ζ is a correction factor given by Karmalkar et al. [48] Combining Eqs. 2.11 through 2.14, the flux of absorbed H_2O_2 on the surface of a Pt NP can be expressed as:

$$\overrightarrow{J}_{in}^{iNP} = \frac{4\pi}{4\pi + \frac{r_{Pt}t}{H(r_{Pt}+t)} \cdot \zeta} \cdot \frac{k_c \cdot E_0 \cdot G_S}{K_M + G_S} \cdot \hat{n} \tag{2.15}$$

Chain NP Limit. Similar to the iNP limit, H_2O_2 molecules are modeled to be generated at a distance t_{ez} away from the chain. The inward and outward diffusion equivalent capacitance is given as:

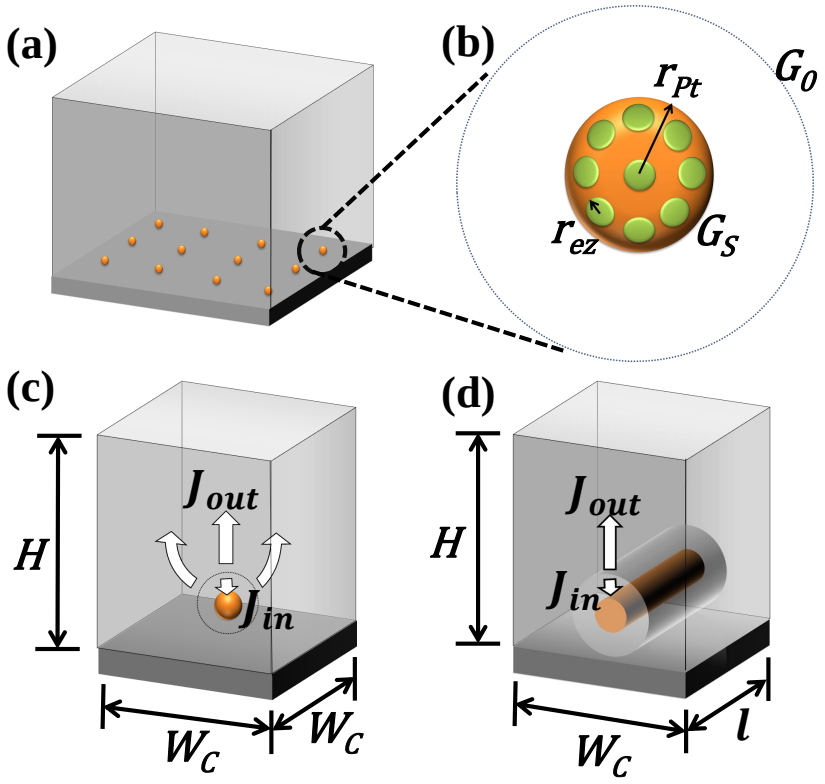

Fig. 2.3.: Isolated nano-particle (iNP) model and chain nano-particle (cNP) model. (a) Each Pt NP electrode is modeled as an identical individual nanosphere isolated in a unit cell. (b) For a single nanosphere electrode with radius r_{Pt}, glucose oxidase enzymes (green) are modeled as disk-like absorbers with radius r_{ez} and thickness t_{ez}. G_S is the glucose concentration near the sensor surface, and G_0 is the glucose concentration far into the solution. The dashed circle represents the spherical boundary of the unit cell. (c) Inward (J_{in}) and outward (J_{out}) H_2O_2 flux inside an iNP unit cell. The H_2O_2 molecules are assumed to generate on a sphere surface with radius $r_{Pt}+t_{ez}$ (solid circle) located between a NP and the unit cell boundary. The unit cell boundary height (H) is much larger than r_{Pt}, and r_{Pt} is much greater than t_{ez}. (d) Unit cell of cNP array unit cell.

$$C_{in}^{cNP} = \frac{2\pi D_{H_2O_2} \cdot l}{ln((r_{Pt}+t_{ez})/r_{Pt})} \tag{2.16}$$

$$C_{out}^{cNP} = \frac{2\pi D_{H_2O_2} \cdot l}{ln(sinh(\frac{2\pi H}{W_c})/sinh(\frac{\pi r_{Pt}}{W_c}))} \tag{2.17}$$

where l is the length of each nanoparticle chain shown in Fig. 2.2 (f). W_c is the pitch between NP chains, and H is the height of the unit cell shown in Fig. 2.3(d). Because the cNP model is periodic at steady state, the concentration at the top surface may be presumed to be small, while the H_2O_2 fluxes among the neighboring cNP cancel each other. The effect of cNP density is reflected in W_c. A small W_c indicates a dense nanowire system so that the output diffusion capacitance is small as well. The corresponding cNP inward flux is therefore expressed as:

$$\overrightarrow{J}_{in}^{cNP} = \frac{ln\left(\frac{sinh\left(\frac{2\pi H}{W_c}\right)}{sinh\left(\frac{\pi r_{Pt}}{W_c}\right)}\right)}{ln\left(\frac{(r_{Pt}+t_{ez})}{r_{Pt}}\right) + ln\left(\frac{sinh\left(\frac{2\pi H}{W_c}\right)}{sinh\left(\frac{\pi r_{Pt}}{W_c}\right)}\right)} \cdot \frac{k_c E_0 G_S}{K_M + G_S} \cdot \hat{n} \tag{2.18}$$

Eqs. 2.15 and 2.18 are the exact inward H_2O_2 flux analytical expressions for iNP and cNP cases, respectively. They depend on reaction parameters such as k_c, E_0, K_m, and G_s as well as electrode geometry parameters such as r_{Pt}, t_{ez}, W_c and H. We emphasize that the parameters are physical, and unlike traditional models, the functional dependencies are explicit.

2.4.1 Total output current

As a final step, we calculate the total output current by integrating the oxidative H_2O_2 flux over the each platinum electrode surface area (S) and sum the contributions from all NPs as follows:

$$I_{tot} = M \cdot 2 \cdot N_A \cdot q \cdot \int \overrightarrow{J}_{in} \cdot d\overrightarrow{S} \tag{2.19}$$

where N_A is Avogadro's constant, M is the total number of NPs in the iNP limit and the number of nanowires in the cNP limit. The factor of 2 reflects the fact that every 1 mole of H_2O_2 generates 2 moles of electrons (Eq. 2.2).

2.5 Results and discussion

To validate the accuracy of the compact model, we compare the model prediction (Eq. 2.19) to experimental data for the sensor structures shown in Fig. 2.2 (a) and (b). Here, the substrate materials are: i) carbon nanotubes (CNTs) and ii) multilayered graphene petal nanosheets (MGPNs). The experimental data are reproduced from Claussen *et al.* [39,40] Appendix A Table A.1 summarizes the physical constants, and Table A.2 lists the model parameters used to evaluate Eq. 2.19. The predictive power of the model is obvious: based on the physical parameters (independently measured or obtained from literature), Eq. 2.19 captures almost perfectly the magnitude and the shape of the response curves for these NP sensors. In Appendix B, we also perform numerical simulation for cNP and iNP systems. The analytical solution and numerical simulation match well, validating the model.

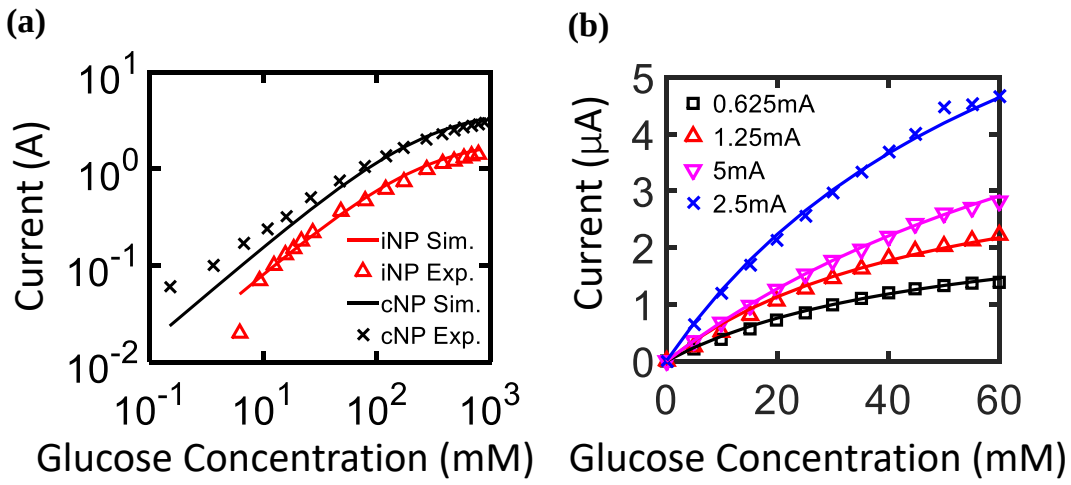

Fig. 2.4.: Experimental and compact model glucose amperometric sensor current response. (a) CNT NP sensor. (b) MPGN NP sensor. The crosses, triangles, and squares represent the experimental data. The solid lines represent the analytical model simulation results.

Fig. 2.2(a) interprets the experimental data for the CNT NP amperometric sensor. For the low-density NP sensor, we find that the iNP model (red line) captures the experimental data (red triangles) with high fidelity based on the following model parameters: distance between NPs W_c= $4r_{pt}$ and the total number of NPs M= 2.67×10^7 (obtained directly from image analysis explained by Claussen *et al.* [39] Here, we find a Michaelis-Menten constant of K_m = 24.9 mol/m^3, consistent with typical values reported in the literature [49, 50].

Similarly, in the high-density limit, the cNP model (black line) interprets the experimental data equally effectively, with the following model parameters: total length of NP chain l= 10 m (equivalent to 6.67×10^7 NPs lined up on a chain side by side) and the distance between chains W_c = $6r_{Pt}$. For glucose concentration below 1mM, our compact model slightly underestimates the experimental data. This reflects our assumption that a 1D cylindrical nanowire can approximate a dense array NPs arranged in a linear chain. Although the surface area of a chain of closely-packed nanospheres equals that of a cylinder of equal radius, the curvatures are different. Therefore, a chain of nano-spheres captures the analyte molecules slightly more effectively than its equivalent cylindrical counterpart.

The same Michaelis-Menten constant (K_m= 24.9 mol/m^3) explains both high and low density cases, as expected. The linear correlation between glucose and output current holds for glucose concentration$G < K_m$. At higher glucose concentrations, the output current begins to saturate to reflect the saturation of H_2O_2 flux, as in Eq. 2.11. Indeed, a turn-over point can therefore be used as an indirect measure of K_m.

Fig. 2.4(b) shows how the model interprets one additional set of data on a MGPN substrate. In the experiment, field emission scanning electron microscopy (FESEM) images of the sensor surface reveal a ridge line of NPs with r_{Pt} values of 86±5 nm, 100±10 nm, 100±10 nm (with smaller inter-NP length) and 300±50 nm that were varied by changing the Pt electrodeposition current pulses from 0.625 mA to 5 mA [39]. We use the measured r_{Pt} values as inputs to our model in Eq. 2.19. For

electrodeposition current pulses of 0.312 mA and 0.625 mA, the NPs were reported to remain isolated. Thus, we use the iNP model to generate the current glucose concentration response. At 1.25mA and 2.5 mA electrodeposition currents, FESEM micrographs indicated that the inter-NP length decreases, and the NPs begin to coalesce. Therefore, we apply the cNP model. At 5mA electrodeposition current, the ridgeline NP chains were reported to expand in width and start to overlap with each other. The corresponding sensor output current for the 5mA electrodeposition case falls between 1.25 mA and 2.5 mA cases. This phenomenon results from a conversion of sensor geometry form 2D chain structure to 1D plane (**case 3**). The individual signature of NPs is now erased, and therefore the current is simply calculated by the classical (planar sensor) model. We quantitatively discuss this phenomenon in Appendix B.

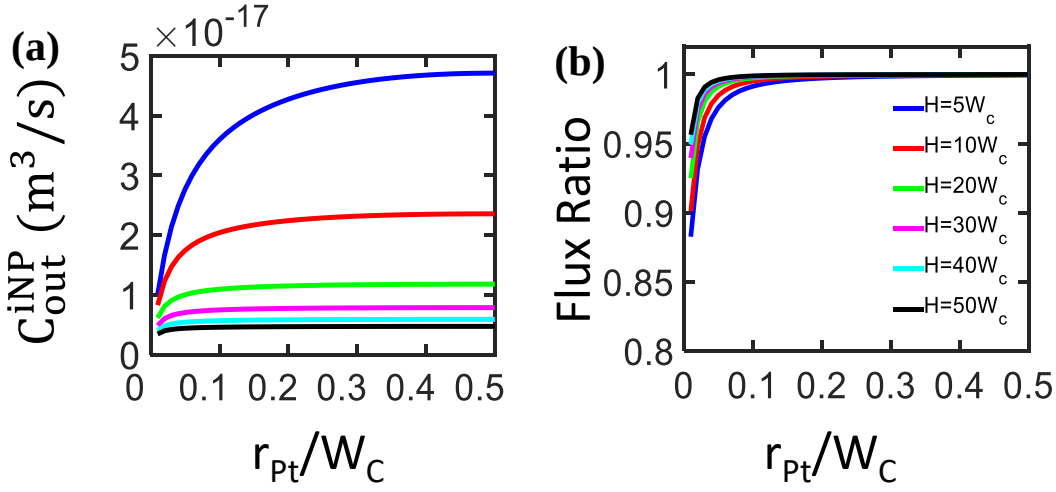

Fig. 2.5.: The impact of Pt on (a) outward diffusion capacitance and (b) H_2O_2 absorption flux ratio with different unit cell height.

Of the three differences between planar sensors and NP sensors discussed in the Introduction as the motivation to develop a new compact model, the results above explained how the shapes/size of the NP and the surface reactions of H_2O_2 influence amperometric current. Next, we wish to discuss the validity of the assumption that

H_2O_2 is fully converted to amperometric current, even for NP sensors. After all, as discussed in 2.2, H_2O_2 generated in one NP can contribute to redox reactions in neighboring NPs through reaction cross-talk. An important observation is that since the total current includes the sum of contributions from all NPs, it is irrelevant if H_2O_2 generated from a NP returns to the same the NP to generate current locally (self-diffusion) or diffuses away to generate current in the neighboring NPs (mutual diffusion) shown in Fig. 2.3 (c) and (d). Instead, the magnitude of the current is determined by the ratio $C_{in}/(C_{in} + C_{out})$ (see Eq. 2.12), dictated by H_2O_2 captured by the NPs (C_{in}) vs. those that diffuses away from the NP and are lost into the solution (C_{out}). Indeed, if a significant fraction of H_2O_2 diffuses away from the sensor surface *(i.e.,* $\mathrm{C_{out}} \gg C_{in}$), the faradic current reduces dramatically. We use the iNP model to discuss this issue quantitatively.

As shown in Fig. 2.5(a), C_{out} increases as a function of normalized r_{Pt}; however, compared to C_{in}, the increase is somewhat smaller. In Fig. 2.5(b), we plot the ratio of absorbing H_2O_2 flux to total H_2O_2 flux as a function of normalized r_{Pt} for different heights of fluid column (H) above the sensor. As the ratio of r_{Pt} and W_c approaches unity (reflecting increasing NP density), the fraction of H_2O_2 converted to current increases and eventually saturates to 100%. In addition, the flux saturates quickly as Hincreases. Intuitively, this phenomenon reflects the fact that the denser NPs have a higher probability of capturing the H_2O_2 molecules before they escape to the solution. Remarkably, even for NPs at relatively low density, more than 90% of H_2O_2 are converted to current.

In addition, the analytical model developed here offers an opportunity to calculate the sensitivity of the total current as a function of various sensor parameters. As an illustrative example, Fig. 2.6 (a) and (b) show that for a given number of NPs, the sensitivity increases with the *square* of the r_{Pt}. The increasing surface area improves H_2O_2 generation and charge collection, as expected. The sensitivity to other parameters, subject to various technology and physical constraints, can easily be evaluated as well.

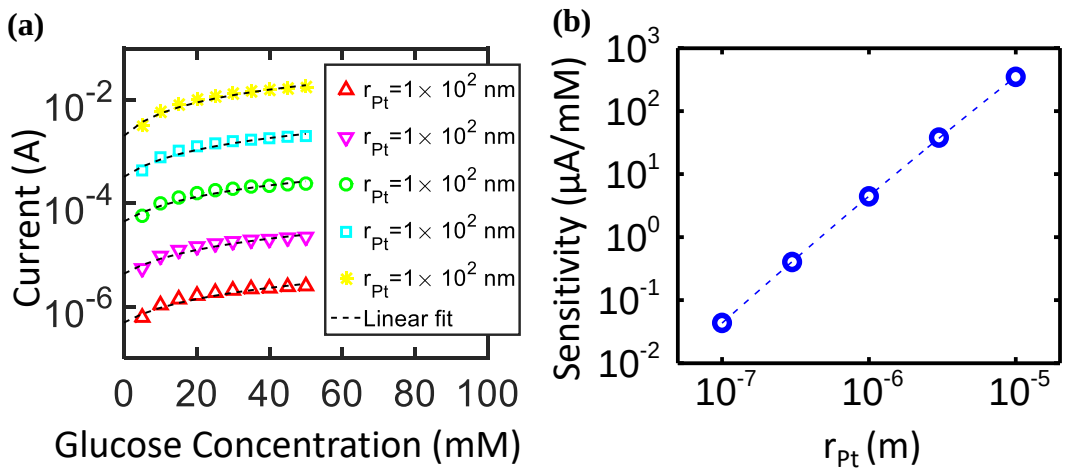

Fig. 2.6.: (a) Amperometric current response as a function of r_{Pt} ranging from 100 nm to 10^4 nm. The total number of NPs presumed a constant. The sensitivity in (b) is calculated from the slope of each fitted lines in (a). The slope of fitted line is 2 (in the log-log plot), indicating that the sensitivity depends quadratically on the radius of NP.

Finally, even though our model was developed specifically for NP amperometric glucose sensor, the conceptual approaches we have used (e.g., dividing the problem into a series of elementary steps, periodic approximation of a random array, use of diffusion equivalent capacitance, etc.) are general, and can be used as building blocks to address other geometrically complex nanoscale bio-chemical sensors that rely on diffusion and reaction of multiple species to achieve their functions.

2.6 Conclusions

In this chapter, we have developed an analytical compact model for amperometric glucose sensors with NP electrodes. This physics-based analytical model captures the functional dependence of the parameters of a NP glucose sensor and thereby can accurately anticipate the experimental trends reported in prior literature. The model

not only suggests opportunities for further optimization, but also can be used for design of complex integrated circuits involving different classes of sensors and other processing elements.

3. METAL OXIDE-BASED NON-ENZYMATIC GLUCOSE SENSOR: CONCEPTS, METHODS, AND CHALLENGES

3.1 Motivation

Glucose sensors have transformed diabetes control. As discussed in chapter 2, most commercial glucose sensors are enzymatic. The first-generation sensors use glucose oxidase (GO_x) enzyme to convert glucose into gluconic acid and hydrogen peroxide (H_2O_2). The amperometric response of H_2O_2 determines the blood glucose level [51]. Although most glucose meters in the market are still enzyme-based, the intrinsic instability of GO_x makes integration onto wearable and implantable platform difficult [52]. For example, GO_x activity depends sensitively on temperature. The degree of temperature control needed is incompatible with long-term bio-implantable applications. Second, the consumption of O_2 during glucose oxidation causes the sensor reading to drift, requiring frequent calibration [53]. Finally, the reaction by-product H_2O_2 is potentially harmful to human body. To overcome these problems of O_2 consumption and H_2O_2 generation, the second-generation mediator-based glucose biosensor replaces O_2 with a non-physiological electron acceptor. It can directly transfer the electrons from the redox center of the enzyme to the surface of the electrode, eliminating the generation of H_2O_2. Unfortunately, the problem of enzyme degradation persists in the 2^{nd} generation sensors.

The development of non-enzymatic electrode for glucose detection promises a new (third) generation of glucose sensors. Metal/metal oxide modified electrode for glucose oxidation had been reported in the 1980s [54–56], but the sensitivity variations due to electrode surface structure prevented its practical application. Over the past

[0]The content of this chapter is primarily taken from a published paper: X. Jin, and M. A. Alam, "Generalized modeling framework of metal oxide-based non-enzymatic glucose sensor: concepts, methods, and challenges." *IEEE Transactions on Biomedical Engineering*, (2019)

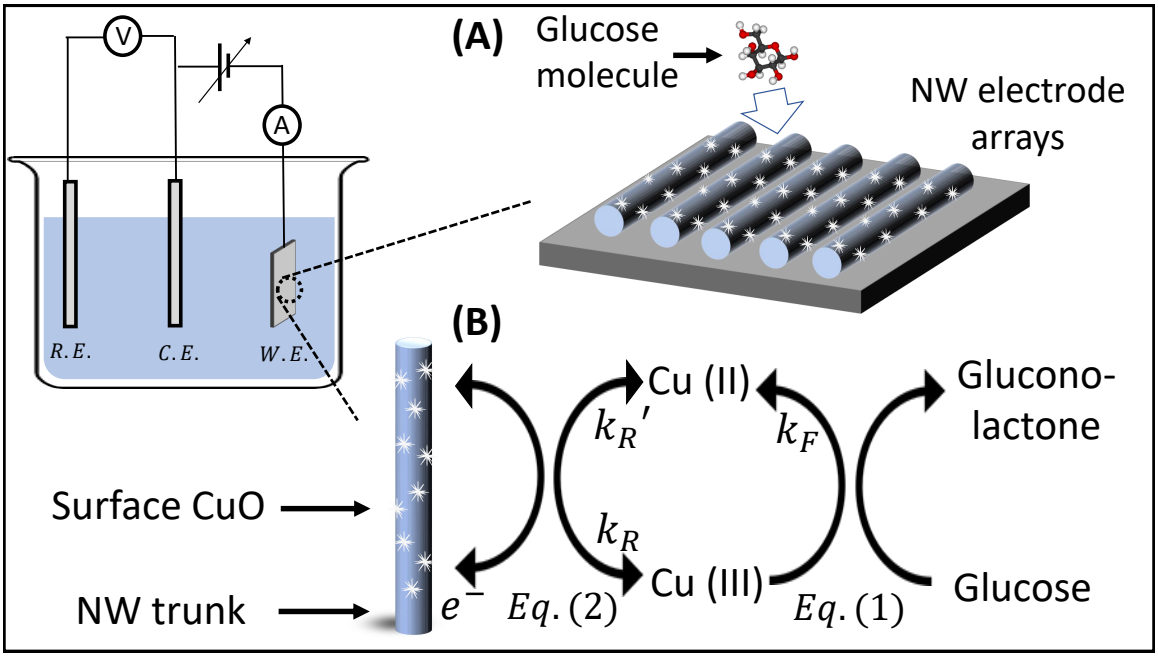

Fig. 3.1.: The detection mechanism of metal oxide-based non-enzymatic glucose sensor. A. Schematic illustration of glucose diffusion in the bulk solution and surface reaction on the NWs. B. Schematic illustration of the intermediate synergistic reaction between oxidative and reductive metal oxide (Cu (III) and Cu (II))

decade, the development of nanostructured material has enabled metal-oxide based non-enzymatic glucose sensing with consistently high sensitivity [57]. Since then a number of groups have developed various platforms integrated with various nanostructured substrates, such as carbon fiber (CF) [58], Cu form [59], carbon coated ZnO nanorod [60], graphene oxide (GO) [61, 62], and CuO-ZnO hierarchical nanocomposites (HNCs) [63], with the objective of enhancing the amperometric response of the sensor. An illustrative example of such a sensor involving an array of nanowires (NW) is shown schematically in Fig. 3.1 A. Although many recently-developed high-performance sensor geometries share the NW-array format, the theory developed in this chapter can be used to optimize other sensors as well.

3.2 Background: non-enzymatic glucose detection

Fig. 3.1 B shows the glucose non-enzymatic detection mechanism. The glucose oxidation process involves the synergistic reactions between the oxidative and reductive metal oxide (Cu (II) and Cu (III) in the example). Eqs. 3.1 and 3.2 show the two specific chemical reactions in the half-reaction cycles:

$$C_6H_{12}O_6 + 2CuO\,(OH) \xrightarrow{k_F} 2CuO + C_6H_{12}O_7 + H_2O \tag{3.1}$$

$$\mathrm{CuO} + \mathrm{OH^-} \underset{\mathrm{k_{R'}}}{\overset{\mathrm{k_R}}{\rightleftharpoons}} \mathrm{CuO(OH)} + \mathrm{e^-} \tag{3.2}$$

Eq. 3.1 describes the forward reaction half cycle where the glucose ($C_6H_{12}O_6$) molecules diffuse towards the electrode surface and are oxidized by the oxidative form of the metal oxide (Cu (III)) in CuO(OH)). Here, k_F denotes the forward oxidation rate. Since the reaction products (gluconic acid, $C_6H_{12}O_7$ and water, H_2O) diffuse back into the bulk solution, we ignore the reverse reaction in Eq. 3.1. In the second backward reaction half cycle in Eq. 3.2, the reductive form of the metal oxide (Cu (II)) in CuO is oxidized back to Cu (III) in CuO(OH) by hydroxide ion (OH^-). The nanostructured conducting substrate collects the extra electron in Eq. 3.2. Unlike the one-way reaction in the first half cycle, Eq. 3.2 is reversible. We use k_R and k'_R to denote the forward and reverse reaction constants, respectively.

Phenomenological amperometric glucose reaction models [64–66] often use k_F, k_R and k'_R as empirical constants. We can briefly explain the physical and chemical basis of these reaction rate constants. The forward reaction constants $\mathrm{k_F}$ describe the ability of the Cu III reaction sites on the nanostructured electrode to capture glucose molecules from the bulk solution. $\mathrm{k_F}$ is determined by several factors such as the morphology of the electrode surface, the pH of the electrolyte [67], etc. Similarly, $\mathrm{k_R}$ and $\mathrm{k'_R}$ describe the ability of the Cu II to gain or lose electrons in the backward reaction. In general, $k'_R$and $\mathrm{k_R}$ follow the Butler Volmer equations [68] shown in Table A.3.

Non-enzymatic glucose detection strategy discussed above takes advantage of both high conductivity and catalytic activity of the metal oxides [69]. Due to the synergistic reactions between the reductive and oxidative states of metal-oxide adsorption sites, the non-enzymatic glucose sensor shows persistent glucose oxidation activity [58]. Unlike the bulk diffusion of H_2O_2 in the first generation enzymatic glucose sensors, the metal-oxide electrodes as well as the intermediate products in the third generation sensors are biocompatible [62, 70, 71]. Similar to the nanoparticle (NP) based enzymatic glucose sensors described in [72], the nanostructured substrate maximizes the active area of the electrode, and thereby improve the output amperometric signal. Finally, the non-enzymatic glucose sensors show thermal stability [73, 74], making them suitable for implantable sensors for chronic diseases.

The chemical reactions of the metal-oxide-based non-enzymatic amperometric glucose sensor are well known [57], however a quantitative model (which includes the physical, chemical, and geometrical design properties) is missing. For example, experimental groups often use a linear relationship between glucose concentration and output current to fit the experimental data [70]. We find that the linear approximation does hold at low glucose detection range (usually up to $\sim$ 2mM). For effective diabetic monitoring, however, the blood glucose concentration ranges from 4.9 - 6.9 mM for healthy individuals and 2 - 40 mM for the diabetic patient [37, 62]. Over this extended range, the amperometric response of the metal-oxide-based non-enzymatic glucose sensor is nonlinear which saturates at high glucose concentration. The limit of linearity where the linear to nonlinear transition occurs depends on the geometrical and chemical features of the sensor design. Thus, an accurate nonlinear model is necessary to describe the sensitivity of the non-enzymatic glucose sensors.

To develop a generalized model for non-enzymatic sensors, one cannot directly apply the model of classical enzymatic glucose sensors for the following reasons: 1) classical glucose sensors typically use planar electrode so that the glucose diffusion towards the electrode is essentially one dimensional (1D). For the nanostructured electrode, the electrode geometry alters the geometry of glucose diffusion in a way

that cannot be described by the 1D approximation. 2) The chemical reactions shown in Fig. 3.1 B are very different from those of the enzymatic glucose reaction. Moreover, all the reactions occur at the surface. Therefore IHOAM (Incipient Hydrous Oxide-Adatom Mediator) model developed by Burke *et al.* does not apply because the model uses Michaelis-Menten kinetics in bulk solution to calculate the amperometric response [75]. For the new non-enzymatic sensor, the glucose reaction occurs on the surface of the nanostructured electrode, thus we cannot ignore the effect of the sensor electrode geometry. A model which quantitatively establishes the impact of the different geometrical and chemical parameters on the overall sensor output response is significant but is not available in the literature.

In this chapter, we develop a new analytical model to capture the essence of the non-enzymatic glucose sensors. As shown in Fig. 3.1 A, the NW electrodes reported in the literature (carbon nanotube, carbon fiber, nanorod, etc.) can be approximated as an array of nanowires by the following assumptions:

1. Glucose oxidation reaction occurs primarily at the top surface of the outermost layer of NWs. This NW layer absorbs most of the glucose molecules, making it difficult for the glucose molecules to diffuse and react within the bulk of the electrode.

2. The effectiveness of random arranged NWs is equivalent to a periodically aligned array of NWs with the same effective density [76].

Although we focus on NW array substrate to interpret experiments, our approach based on equivalent diffusion capacitance model applies to any electrode geometry. We analytically calculate the coupled surface reactions of the metal oxides by solving mass transfer flux balance equations. We also numerically simulate the diffusion-reaction processes and validate the accuracy of the analytical model. We calibrate the design parameters such as different reaction constant and the electrode geometry factors by fitting the measurement data from several experimental groups. The model

quantifies the effectiveness of various design parameters and provides guidelines to improve the overall performance of metal oxide-based non-enzymatic glucose sensor.

3.3 Modeling

As described in 3.1, we model the non-enzymatic glucose detection mechanism as a two-step process: 1) diffusion and oxidation of glucose molecules assisted by metal oxide, and 2) subsequent metal oxide reaction and generation of the amperometric signal.

The classical diffusion Eq. 3.3 describes the mass transport of glucose in the bulk solution before they reach the electrode surface. In a bulk solution, the transport of glucose molecules is a diffusion-limited (or diffusion controlled) process [77, 78]. Any secondary transport phenomena such as natural convection is neglected in our model. This assumption will ultimately be test by the ability of the model to anticipate experimental results.

The oxidation reaction occurs only when the glucose molecules diffuse near the electrodes, described by Eq. 3.4 since the metal oxide molecules are immobilized on the nanostructured electrode surface. Therefore, the solutions of the following equations describe the surface glucose absorption flux:

$$\frac{dG}{dt} = D\nabla^2 G \tag{3.3}$$

$$J_{rec} = k_F \cdot N_{III} \cdot G_s \tag{3.4}$$

where G is the glucose concentration, D is the glucose diffusion coefficient, N_{III} represent the surface density of metal oxide in the oxidative state (Cu III), and G_S is the bulk glucose concentration near the NW surface. The occurrence of chemical reactions as a source term is included in Eq. 3.4 where the reaction flux J_{rex} associated with Eq. 3.1 at the electrode surface is proportional to k_F, G_s and N_{III}.

Similarly, a detailed description of the solution of Eq. 3.2 is included in Eq. 3.5 and Eq. 3.6. The changing rate of the surface density of Cu (II) can be expressed as the sum of forward and reverse reaction flux:

$$\frac{dN_{II}}{dt} = k_F N_{III} G_S - (k_R N_{II} - k'_R N_{III}) \tag{3.5}$$

where N_{III} and N_{II} follow the total metal element conservation relation:

$$N_{III} + N_{II} = N_0 \tag{3.6}$$

As reported by many experimental groups [62, 63, 79], the selectivity of the metal oxide to glucose is orders of magnitude higher than other biomolecules such as dopamine, ascorbic acid, uric acid, fructose, lactose, and sucrose. The impact of the competing species on the Cu active sites is negligible. Therefore, we need not include the additional reaction terms for the competing species in Eq. 3.5.

It is also worth noticing that the effect of pH is very important. Therefore, the sensor characterization experiments in the literature are conducted in an electrolyte with a constant pH value of 9-13 [70, 71, 79]. The high pH solution ensures that there are sufficient OH^- supply for the chemical reaction in Eq. 3.2. As a result, the reaction rate-limiting factor is Cu (II) surface density N_{II}, not the concentration of OH^-. Thus, the pH-dependence term is not included in our current model.

The coupled diffusion and surface reaction equations (Eq. 3.3 to 3.6) can be solved both numerically and analytically. In the analytical solution, we apply the concept of 'diffusion equivalent capacitance' [80]. Note that glucose diffusion equation reduces to $D\nabla^2 G = 0$ in the steady state, which has the same form mathematically, as the Laplace's equation, $\epsilon\nabla^2\phi = 0$ [81]. The solution of one equation can be mapped to that of the other by recognizing the mathematical equivalence of the electrostatic potential ϕ to the glucose concentration G and the permittivity ϵ to the diffusion coefficient D. Similarly, one can define an analogous parameter to the electrostatic capacitance (C) called 'diffusion equivalent capacitance' (C_D).

The steady-state diffusion flux of glucose molecule in the bulk solution can be written as:

$$J_{diff} = C_D \cdot \frac{G_0 - G_S}{A_e} \tag{3.7}$$

where C_D is the equivalent diffusion capacitance for the nanostructured electrode of any geometry (the expression for nanowire array as an illustrative example can be found in Table A.3). Here, G_0 and G_s are the bulk glucose concentration and glucose concentration near the electrode surface respectively. A_e denotes one single nanoelectrode surface area.

To calculate the sensor response by solving Eq. 3.3 to 3.7, we rewrite the equations in the normalized form with the unitless variables: $N^*_{III} = \frac{N_{III}}{N_0}$, $N^*_{II} = \frac{N_{II}}{N_0}$, $G^*_s = \frac{G_s}{G_0}$, $\gamma = \frac{C_D}{A_e \cdot k_F N_0}$, $\alpha = \frac{k_R}{k_F G_0}$, and $\beta = \frac{k'_R}{k_F G_0}$. We can then solve for the three unknown variables: N^*_{III}, N^*_{II}, and G^*_s. The exact solution can be found in Table A.3. We also derive an approximate expression for N^*_{III} and N^*_{II}:

$$N^*_{III} = \frac{\alpha}{(\alpha+\beta+1)-\alpha/\gamma} \tag{3.8}$$

$$N^*_{II} = 1 - N^*_{III} \frac{G_0 + \left(\frac{k'_R}{k_F} - \frac{A_e k_R N_0}{C_D}\right)}{G_0 + \left(\frac{k_R + k'_R}{k_F} - \frac{A_e k_R N_0}{C_D}\right)} \tag{3.9}$$

The analytical expression for N^*_{II} is similar to the analytical model in the Michaelis-Menten kinetics. Michaelis-Menten constant (K_M) only accounts for the chemical reaction, however, the extra terms in both the numerator and the denominator of Eq. 3.9 include the diffusion capacitance C_D to capture the effect of the nanostructured sensor electrodes.

The final amperometric response of the glucose sensor can be expressed as a function of N_{II}:

$$\begin{aligned} i &= q \cdot N_A \cdot A_{eff} \cdot (k_R N_{II} - k'_R N_{III}) \\ &= q \cdot N_A \cdot A_{eff} \cdot (k_R + k'_R) \cdot N_0 \cdot (N^*_{II} - \tfrac{k'_R}{k_R + k'_R}) \end{aligned} \tag{3.10}$$

Eq. 3.8 to Eq. 3.10 are general expressions that describe the response of any metal-oxide based non-enzymatic glucose sensor with an arbitrarily complex nanostructured electrode. To interpret specific experiment, we need to use the appropriate expressions for the diffusion capacitance C_D and the effective electrode surface area A_{eff}. The effective electrode surface area can be written as $A_{eff} = \eta \cdot A_e$. Here A_e is the real sensor surface area, η is the current transfer efficiency coefficient which account for the electron loss. The electron loss is due to some secondary reactions associated with glucose or metal oxide. η describes the fraction of electrons from glucose molecules that follow the electrochemical reactions in Eq. 3.1 and Eq. 3.2 and contribute to the amperometric response of the sensor.

To summarize, we have derived an analytical model describing the steady-state amperometric response of non-enzymatic glucose sensor. We have used CuO/CuO(OH) glucose sensor as an example to illustrate the physical meaning of the modeling parameters. Our general modeling framework can describe a variety of non-enzymatic glucose sensors such as metal-based glucose sensor [82,83]. Taking the Platinum non-enzymatic glucose sensor in [84] as an example, we could change N_{II} and N_{III} to be the surface density of $Pt[OH]_{ads}$ and Pt. Next, we are going to validate our model by numerical simulation and experimental data.

3.4 Model validation

In this section, we will validate our analytical model Eq. 3.8 to Eq. 3.10 against the numerical and experimental results. Since NW-array is the most commonly used substrate material reported in the literature, we will focus on this specific class of sensors to demonstrate the validity of the model. We will first compare the numerical simulation results with the analytical expression in Table A.3 and Eq. 3.10. This comparison will explain the origin of the nonlinear response of these sensors from the reaction-diffusion perspective. Then, we will use our model to explain the experimental observations reported in the literature.

3.4.1 Validation by Numerical simulation

In the numerical simulation, we set up a simplified 3D NW geometrical structure shown in Fig. 3.1 A. The NW sensor is decorated with numerous CuO(OH)/CuO reaction-sites. We solve Eq. 3.3 to Eq. 3.7 by finite element method (FEM) for the single unit cell of the NW array. The length of the unit cell equals the length of a single NW (l). The width of the unit cell W_C represent the pitch between each NW. The bulk glucose concentration G_0 is held fixed at the top surface of the unit cell. We use reflective boundary condition on the side surface to interpret the cross diffusion of glucose from the neighboring unit cells.

The FEM solution in Fig. 3.2 B shows that the surface reaction reduces the glucose concentration near the NW surface (G_s). By Eq. 3.7, we can then numerically calculate the total output current by directly integrating the current flux over all the NW surface. The FEM transient current fluxes in Fig. 3.2 C show that the current is initially negative due to the initial condition: $N_{III} = N_0$. After the transient phase spanning several hundred seconds, the fluxes saturate to levels defined by the glucose concentration.

3.4.2 Experimental validation

For the experimental validation, we use different types of non-enzymatic glucose sensors reported in the literature. The substrate NW electrode are: 1) nanostructured graphene foam (GF). 2) carbon fiber (CF) [71] and 3) ZnO-CuO hierarchical nanocomposite (HNC) NW [63]. Nanocrystalline CuO (Cu II) molecules with imperfect crystallinity or special morphology are immobilized onto the surface of different NW electrode substrates.

As mentioned in the Introduction, the reaction constants in Eq. 3.1 and Eq. 3.2 have physicochemical interpretation. Since we focus on the steady-state response in our model, we calibrate k_F, k_R and k'_R as constants based on the following assumptions:

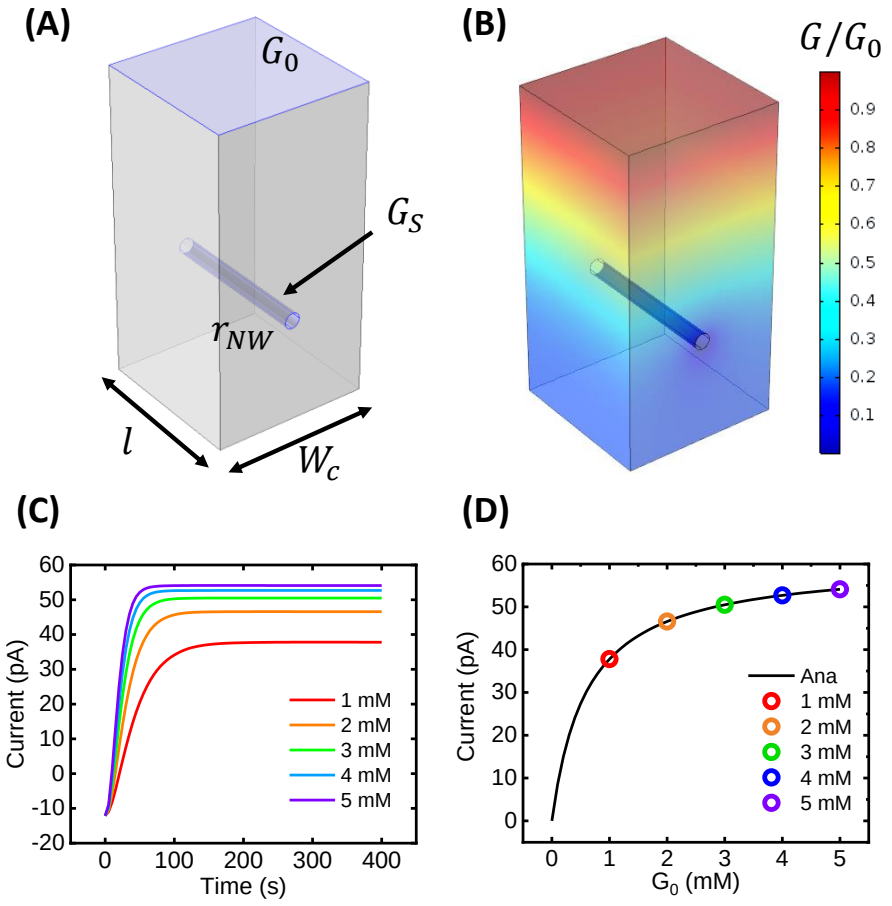

Fig. 3.2.: Numerical validation. A. 3D NW electrode structure in the numerical simulation. B. Bulk glucose concentration profile. C. The non-enzymatic glucose sensor transient response from the numerical simulation. D. Steady-state response from numerical simulation vs. analytical solution.

1. In the steady state, the applied voltage bias E is a constant. The voltage dependences have been included in k_R and k'_R.

2. The chemical property of Cu III does not change during the characterization experiment so that the prefactor k_0 in the Butler-Volmer equation is a constant.

A detailed discussion regarding the physical origin of the parameters k_F, k_R and k'_R on the overall sensor output response can be found in 3.5.2

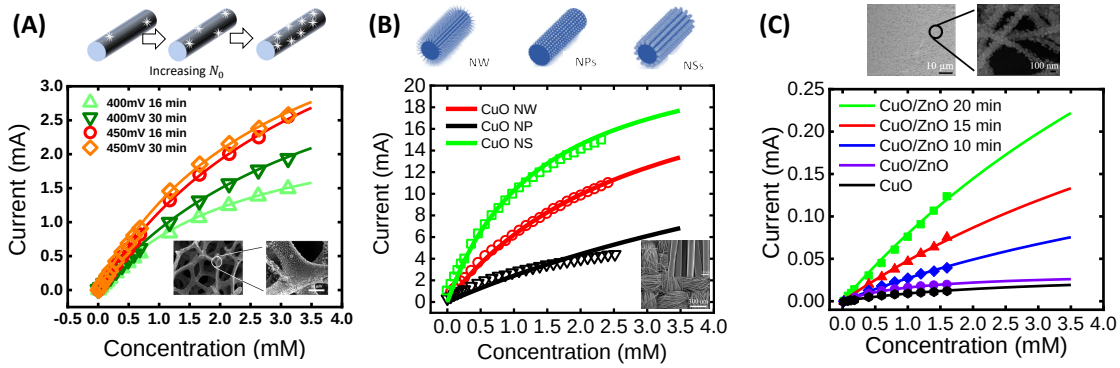

Fig. 3.3.: The steady-state amperometric response of different types of non-enzymatic glucose sensors. (A) metal-oxide-based non-enzymatic glucose sensor on graphene foam substrate with different CuO deposition voltages (400mV and 450mV) and different deposition time (16 min and 30 min). The inset SEM figure shows the CuO form has NW morphology. The figure on the top illustrate an increase of surface density of CuO/CuO(OH) N_0 due to increasing deposition voltage and deposition time. (B) ultrasensitive non-enzymatic glucose sensors based on different copper oxide nanostructures by in-situ growth. Schematic illustration of three different CuO morphology appear in the top figure. (the inset SEM figure and top figures come from Zhong et al.) (C) ultrasensitive non-enzymatic glucose sensor based on a three-dimensional network of ZnO-CuO hierarchical nanocomposites by electrospinning. SEM image of CuO/ZnO NW structure appears in the top figure (come from Zhou et al.). The symbols in all the figures represent the measurement data and the solid lines indicate the simulation results from our model.

Fig. 3.3 A shows the experimental data for the GF substrate non-enzymatic glucose sensor. The low-noise character of GF substrate allows one to detect small amperometric signal induced by glucose redox reactions [62]. The CuO (Cu II) is deposited on the GF by the electrophoretic deposition (EPD). The CuO particles exhibit a fluffy morphology. The size and surface density of the CuO is controlled by deposition voltage and deposition time in the fabrication process. In this work,

Park [44] used two deposition potentials (400mV and 450 mV) and two deposition times (16 min and 30 min). The microscopy images show that the CuO particles are mostly deposited on the outside surface of graphene foam. The inset figure in Fig. 3.2 A show that this layer of graphene foam trunk resembles a nanowire morphology. Hence the nanowire model is appropriate for the geometrical approximation of the sensing electrode

The higher deposition voltage and longer deposition time increase the surface density of CuO on the GF surface (N_0), with a corresponding increase in the output. With the copper oxide surface density N_0 as the only fitting parameter, the results show that our model captures the experimental data with high fidelity. Table A.4 summarizes the value of N_0 for each electrophoretic deposition case. The table shows that the deposition voltage have a larger impact on N_0 than deposition time, as expected.

In Fig. 3.3 B, we compare the model prediction to another set of experimental data on carbon cloth (CC) substrate. The FESEM image shows that the CC is weaved by bunches of carbon fibers (CF) with an average radius of $\sim 5\mu m$. The sensor electrode micro-morphology can be interpreted by an equivalent layer of periodic NW array [76]. In the detailed fabrication process, Zhong *et al.* in-situ growth CuO on the CF surface. Under different fabrication conditions, the CuO nanoparticles themselves show three distinct morphologies: nanoparticle (NP), nanowire (NW) and nanosheets (NSs). Fig. 3.3 B shows that the CuO NSs generate the strongest amperometric response while the CuO NP electrode exhibits the weakest. To model different CuO morphologies, we calibrate the forward chemical reaction constant k_F. The current response of NSs CuO morphology reveal highest k_F value, which indicates that NSs CuO intercepts the glucose molecules more effectively than NW CuO and NP CuO.

Finally, Fig. 3.3 C shows how the model interprets one additional set of data on 3D ZnO-CuO HNC. Zhou *et al.* fabricated ZnO-CuO NW trunk as the non-enzymatic glucose sensor electrode by electrospinning method. Additional CuO nanoparticles were attached to the NW outer surface. In this experiment, the amperometric re-

sponse of the glucose sensor alters much more complicated since it is affected by a combination of changing variables at the same time. Fig. 3.3 C shows that by adding ZnO to the CuO NW trunk (black curve and magenta curve), the sensor electrode amperometric response is slightly improved. Adding a small amount of ZnO could have the potential to boost the electron exchange rate from the glucose molecule, which is revealed in the increase of k_F. As the electrospinning time increases, more ZnO molecules are getting mixed with the CuO NW trunk. To account for this phenomenon, we increase the reverse reaction constant (k_R and k'_R). Larger k_R and k'_R values reveal the observation in [63] that additional Zn element shift the Cu 2p orbital X-ray photoelectron spectroscopy (XPS) peak to higher binding energy, therefore making it easier to transfer electrons from the CuO particles to the CuO/ZnO NW electrode. In addition, for the first two cases (CuO only and CuO/ZnO NW) where the electrospinning time is relatively short, the amperometric response saturates at high glucose concentration. It is perfectly caught by our analytical model. By sweeping the coeletrospinning time to 10 min - 20 min, the surface density of CuO on the electrode as well as the density of ZnO-CuO HNCs NW array electrodes themselves were reported to be higher which further enhance the output current.

3.5 Discussions: Parametric Response, Design Guidelines and Comparison with Enzymatic Sensors

In the previous section, we have successfully interpreted the amperometric response of various non-enzymatic metal-oxide-based glucose sensor within a common theoretical framework. In this section, we will explore the effect of some critical parameters on the overall nonlinear response of the sensor. We will compare glucose detection performance of non-enzymatic sensor to classical glucose oxidase (GO_x)-based sensors. Finally, we will summarize the design guidelines for improving the sensor performance.

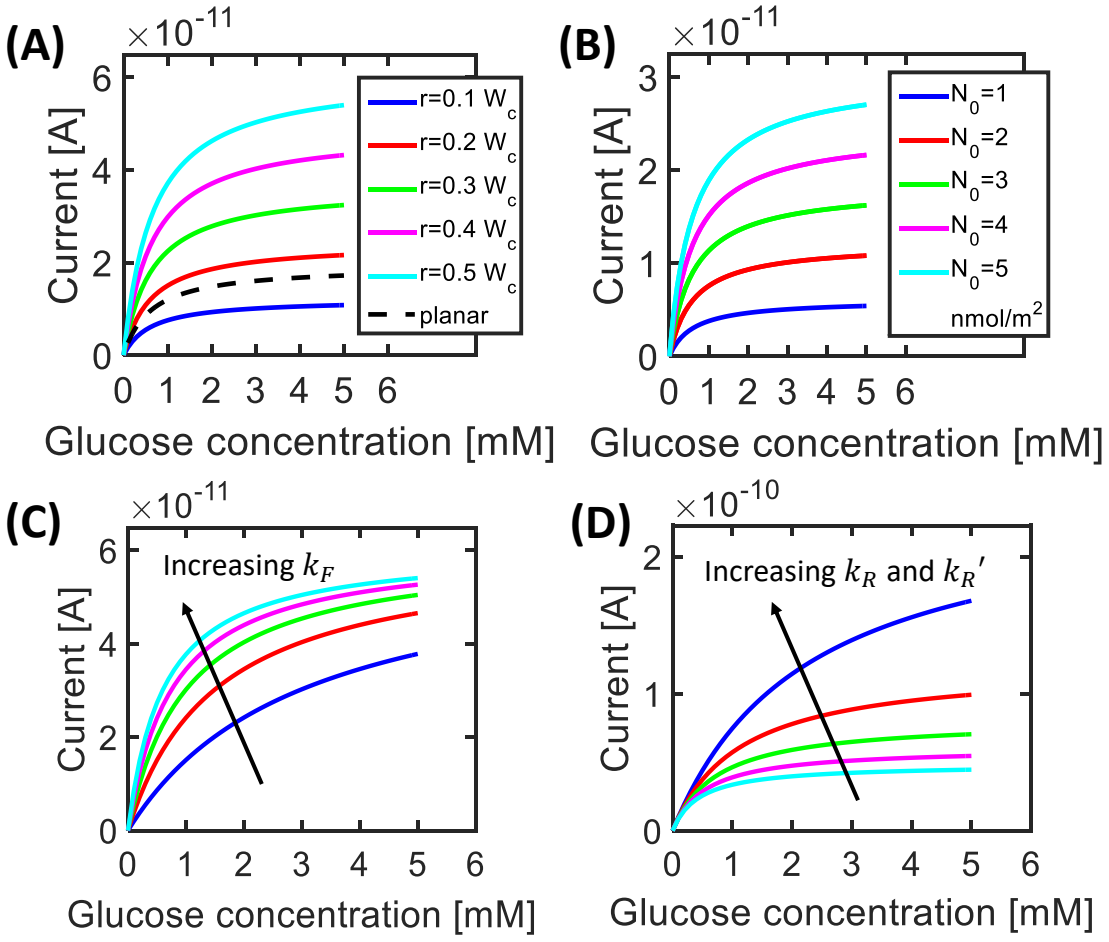

Fig. 3.4.: The simulated parametric response of non-enzymatic glucose sensors. A. Amperometric current response of non-enzymatic glucose sensor with r_{NW} ranging from 1 μm to 5 μm. B. Amperometric current response of non-enzymatic glucose sensor with G_0 ranging from 1 mM to 5 mM. C. Amperometric current response of non-enzymatic glucose sensor with different forward reaction constant k_F. D. Amperometric current response of non-enzymatic glucose sensor with different backward reaction constant k_R and k'_R.

3.5.1 Effect of the radius of NWs and surface metal-oxide density

Fig 3.4 A shows that for a given number of NWs, the output current increases linearly with r_{NW}(W_C is the pitch between NWs). It indicates that the total electronic

charge collected by the NWs scales proportionally to the total surface area of the NW electrodes. Also, the sensitivity in the linear range scales with r_{NW}. Similarly, Fig. 3.4 B shows that the CuO density on the NW electrodes surface also scales the amperometric response linearly (for a fixed NW surface area.) However, the amperometric response in Fig. 3.4 A and Fig. 3.4 B both saturate around glucose concentration at 1 mM. In other words, the linear dynamic range does not scale with r_{NW} and N_0.

In Fig. 3.4 A, it is worth noting that the amperometric response of a planar electrode with the same unit cell footprint area (dashed line) occurs between $r_{NW} = 0.1\ W_C$ and $r_{NW} = 0.2\ W_C$. It means that when the effective NW surface area ($2\pi r_{NW} l$) surpass the planar sensor ($W_C \cdot l$), the overall sensor output current of the NW electrode will be larger than the equivalent planar sensor. NW electrode with larger radius (or equivalently a larger density) would increase the overall amperometric response compared to the classical planar sensor.

The effect of N_0 on sensor response is best explained by the experimental observation in Fig. 3.3 A which shows that the deposition voltage have a larger impact on N_0 than deposition time. Therefore, we conclude that higher electrophoretic deposition voltage and longer deposition time increase N_0 substantially. As a result, the amperometric response for a given glucose concentration scales with total effective electrode surface area and the area density of CuO. The limits of linearity (LOL) and the corresponding dynamic range, however, does not scale with either of these variables.

3.5.2 Effect of chemical reaction constants

Zhong *et al.* reported the nonlinear amperometric response for surfaces with various types of copper oxide nanostructure [71]. The effect of local nanostructures is reflected in the forward reaction constant k_F as shown in Eq. 3.1. To study how the surface morphology (and local nanostructure) affect sensor performance, we plot

in Fig. 3.4 C the sensor current as a function of k_F with all other parameters held constant. We find that an increase of k_F increases the sensitivity (up to LOL, the limit of linearity), but the nonlinear curve saturates at a *lower* glucose concentration. This simulation result is consistent with Zhong's experimental observation in [71] (Fig. 3.3 B). The current response of nanosheet CuO morphology shows the effect of high k_F value. This indicates that nanosheet CuO morphology intercepts the glucose molecules more effectively than NW CuO and NP CuO.

In Fig. 3.4 D, we analyze the relative importance of the backward reaction constants: k_R and k'_R (the ratio of k_R and k'_R remains a constant due to the well-known Bulter-Volmer kinetics). Physically, k_R and k'_R describe the ability of the CuO to gain or lose electrons in the backward reaction in Eq. 3.2. We find that the increase of k_R and k'_R not only enhance the magnitude of the amperometric current response, but also expand the linear dynamic range.

The ZnO-CuO HNC non-enzymatic glucose sensor reported in [63] (Fig. 3.3 C) confirm our assertion. We conclude that adding a different type of metal oxide (such as ZnO) will improve the chemical reaction rates. We can manually increase the dynamic range by changing the chemical composition of the metal oxide.

3.5.3 A comparison between different glucose sensing techniques

Finally, it is important to compare the relative performances of the first generation (widely used) enzymatic glucose sensor, the third-generation non-enzymatic glucose sensor discussed in this chapter, and other newly reported glucose sensor. Table 3.1 compares the performance of several nanoelectrode glucose sensors in terms of their linear range, detection limit, and sensitivity. Specifically, let us focus on two non-enzymatic metal oxide-based cases (CuO and CuO/ZnO) studied in this chapter, as well as two metal-based cases(Pt) [84,85], and two classical enzymatic glucose sensors reported in the literature [86, 87]. The enzymatic sensors use Pt nanoparticle (NP) as the sensing electrode and glucose oxidase as the enzyme catalysis. Multilayer

graphene petal nanosheet (MGPNs) or single wall carbon nanotubes (SWCNT) are used as the substrate material to collect the output current.

In general, the limits of detection for all the glucose detection techniques range within the same order of magnitude (i.e. a few μM.) However, the linear dynamic range for non-enzymatic metal oxide-based sensors is *much smaller* than that of other types of glucose sensors (metal-based, enzymatic, and optical). The sensitivity of non-enzymatic metal oxide-based sensors, on the other hand, is orders of magnitude larger. It appears that these different types of sensors make very different linearity-sensitivity tradeoff with important implications for their practical applications.

First, our analytical model summarized in Eq. 3.8 to Eq. 3.10 attributes the difference in linear range to the intrinsic property of different reaction mechanisms. Quantitatively, if we ignore the effect of nanoelectrode geometry on glucose molecule diffusion in Eq. 3.9, the ratio of forward and backward reaction rate ($\frac{k_R+k'_R}{k_F}$) determines the linear dynamic range. This ratio for a non-enzymatic metal oxide-based glucose sensor is smaller than that of metal-based sensors or the equivalent Michaelis-Menten constant K_M for glucose oxidase in an enzymatic glucose sensor. Second, the huge gap between the sensitivities arise from a combination of different geometrical factors and reaction rates. In Eq. 3.10, the factor $A_e \cdot (k_R + k'_R) \cdot N_0$ for non-enzymatic metal oxide-based case is much larger than either the metal-based sensors or the equivalent $A_e \cdot k_{cat} \cdot E_0$ for enzymatic glucose sensors, where k_{cat} denote the glucose oxidase catalysis rate and E_0 stands for the surface density of glucose oxidase. A_e is the effective surface area of the NW/NP electrode per sensor footprint area.

Table 3.1.: Detection performance of non-enzymatic vs. enzymatic glucose sensor

Glucose Sensor	Sensor Type	Linear Range (mM)	Detection Limit (μM)	Sensitivity ($\mu A \cdot mM^{-1} \cdot cm^{P}-2$)	Ref.
CuO, NP	Non-enzymatic Metal oxide-based	Up to 1.22	1	1245.9	[71]
CuO, NW		Up to 1.12	same	2973.2	
CuO, NSs		Up to 1	same	4901.9	
CuO NW	Non-enzymatic Metal oxide-based	0.046 - 1.6	3.2	278.4	[63]
CuO/ZnO NW		0.025 - 1.6	1.8	484	
CuO/ZnO HNC 10min		0.0142 - 1.6	0.52	1680.2	
CuO/ZnO HNC 15min		0.015- 1.6	0.78	2080.7	
CuO/ZnO HNC 20min		0.0047 - 1.6	0.21	3066.4	
Pt-MWCNT/AC/CNF	Non-enzymatic	2 - 20	Not reported	1.10, 1.07, and 0.52	[84]
Nanoporous Pt		Up to 10	Not reported	6	[85]
GOx-PtNP/MGPNs 0.312mA	Metal-based Enzymatic	Up to 30	0.3	9.71	[87]
GOx-PtNP/MGPNs 0.625mA		same	same	11	
GOx-PtNP/MGPNs 1.25mA		same	same	12	
GOx-PtNP/MGPNs 2.5mA		same	same	13.7	
GOx-PtNP/MGPNs 5mA		same	same	12.9	
GOx-Pt-iNP/SWCNT	Enzymatic	0.2 - 8	5.8	0.32	[86]
GOx-Pt-cNP/SWCNT		0.6 - 20	same	same	
SPR Ag NP	Optical	0 - 20	2.7	0,053 a.u./mM (Light absorbance)	[88]
SPR MCFs		Up to 9	Not reported	0.019 degree/mg/dL (resonance angle)	[89]

Table 3.2.: Summary of glucose concentrations measure in physiological fluids of healthy and diabetic patients

Physiological fluid	Healthy concentration (mM)	Concentration for Diabetic Patients (mM)	Ref.
Blood	4.9 - 6.9	2 - 40	[90–92]
Interstitial fluid	3.9 - 6.6	1.99 - 22.2	[53, 93]
Urine	2.78 - 5.55	> 5.55	[94]
Sweat	0.06 - 0.11	0.01 - 5	[95]
Saliva	0.23 - 0.38	0.55 - 1.77	[96]
Ocular fluid	0.05 - 0.5	0.5 - 5	[90, 97]

Table 3.2 shows the range of glucose concentration for healthy and diabetic patients in various physiological fluid [98]. We find that blood, interstitial fluid, or urine glucose measurement require a large detection range, therefore the classical GO_x enzymatic sensors as well as the metal-based glucose sensors are the best options. The optical glucose sensors also match the detection range. They might be another interesting alternative option for diabetes control since it overcome some disadvantages of amperometric glucose sensors such as susceptible to electromagnetic interference[51]. On the other hand, for wearable closed-loop glucose control systems such as ocular fluid sensor in the contact lens or flexible skin-mounted sweat sensor, the non-enzymatic metal oxide-based glucose sensor discussed in this chapter might be a better option since it has extremely high sensitivity in the lower concentration range.

3.6 Conclusions

The non-enzymatic metal oxide-based glucose sensor is a promising candidate for future wearable and implantable closed-loop diabetes control systems. In this

chapter, we have derived a generalized mathematical model which captures the critical design parameters for this new non-enzymatic glucose sensors. We calibrate those parameters such as different reaction constant, electrode geometry factors by fitting the experimental data from experimental data reported in the literature. Based on our model, we explore the effectiveness of various design parameters. We conclude that:

1. The geometrical factors (such as the radius of NWs and surface metal oxide density) linearly scale the magnitude of output current response.

2. Changing the metal oxide morphology or adding different types of metal oxide alter the chemical reaction constants, thereby increasing the dynamic range.

3. The Non-enzymatic metal oxide-based glucose sensor appears particularly suited for low concentration glucose monitoring systems.

Our work will help integrate the new generation of non-enzymatic glucose sensor into continuous glucose monitoring system (CGMS) in wearable and implantable platforms.

4. MODELING, DESIGN GUIDELINES, AND DETECTION LIMITS OF SELF-POWERED ENZYMATIC BIOFUEL CELL (EBFC) AMPEROMETRIC SENSOR

4.1 Motivation

Advances in materials engineering, biotechnology, and electronics lay the foundations for the development of new classes of miniaturized biochemical sensors [72, 99–102] that offer performance similar to conventional, laboratory-based, benchtop analytical instruments. Of particular interest is the rise of enzymatic biofuel cell (EBFC)-based biochemical sensors as self-powered systems [103, 104] for their applications in energy-limited settings including wearable technology [105–107]. In contrast to traditional amperometric sensors introduced in chapter 2 and chapter3 [52,63,72,86,87,108] (Fig. 4.3 (a) and (b)) that require bulky external power sources and complex electrical designs and components, their EBFC-based counterparts [109–114] (Fig. 4.1 (c)) rely on spontaneous redox reactions thus circumventing the need for external energy source and complex electronics. These attributes allow several orders of device miniaturization essential for the realization of new sensor platforms, for example, tissue-integrated biochemical sensors in the form of epidermal [107, 115] and ocular systems [90, 116–118].

The recent increasing interest in wearable and field-deployable miniaturized sensors indicate imminent widespread exploration of EBFC-based sensors as self-powered alternatives [119–121] to conventional approaches. While the literature points to extensive experimental research in developing these sensors, the field of analytical modeling of these unconventional sensors remain understudied. Such analytical models are

[0]At the time of the thesis deposition, this chapter is reproduced from the submitted paper with the permission of ACS Publishing.

crucial for the success of the EBFC-based sensors as these can help researchers fathom complex inter-related redox reactions occurring within the EBFC-based sensors and provide valuable guidelines to develop systems with desired performance. Unfortunately, traditional theoretical papers in the field of EBFCs focus on optimizing the performance of EBFC as an energy source [122–124] (e.g. increase output power density, reduce charging time, suppress self-heating and parasitic reaction, etc.). Song et al. illustrate a Michaelis-Menten kinetics derived 3-D modeling and numerical simulation framework for EBFC interdigitated microelectrode arrays with the goal of improving energy density and output power [125]. To assess charging time and self-heating, Chan et al. introduce a dynamic model of anode function in EBFC [126]. The model includes sophisticated anode reactions and analyze their impact on the battery charging potential, power density and, dynamic response. However, the performance metrics of an EBFC biosensor differs significantly from an EBFC battery [127, 128] and hence cannot be directly applied to EBFC-based sensors. For example, unlike an energy source, a biosensor must be: (a) as small as possible for ease of integration, (b) the cell must always operate at physiologically relevant and time-variable analyte concentrations, (c) the linearity of response is a critical factor for calibration and any long-term drift in the conversion efficiency can mislead clinical diagnosis, (d) the cathode-reaction due to oxygen starvation is often a concern that is seldom encountered in EBFC batteries, (e) signal-to-noise ratio is a critical parameter to define selectivity and the limits of detection, and (f) the quasi-static evolution of signal need not be described by fast charge-discharge models and self-heating is not a concern. The goal of this chapter is to develop a comprehensive theoretical model (based on physical, chemical, and geometrical parameters) to transparently correlate the analyte concentration to the amperometric current so that one can optimize for the specific metric of EBFC-based biosensor [129].

In this chapter, we describe a new model for the EBFC-based self-powered biosensor. In section 4.2.1, 4.2.1, and 4.2.3 , we use sophisticated numerical modeling plus simple analytical formulas to capture the essential physics, which agree closely with

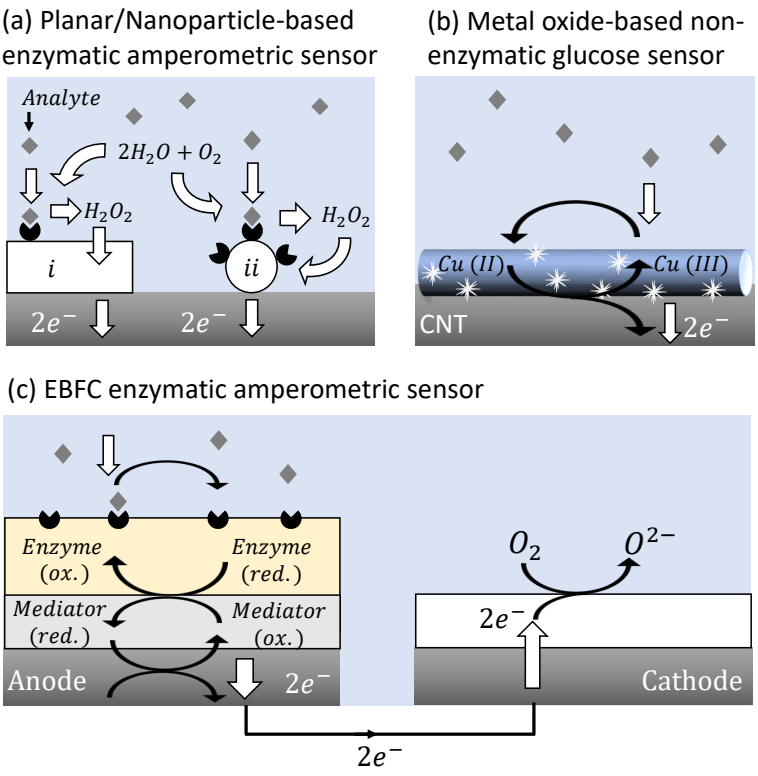

Fig. 4.1.: Schematic illustrations of the working mechanism of (a) (i)Planar/(ii)Nanoparticle-based enzymatic glucose/lactate sensor. GOx/LOx works as enzyme and H_2O_2 works as electron mediator (b) Metal oxide-based non-enzymatic glucose sensor. (c) Bio-fuel amperometric enzymatic glucose/lactate sensor.

the sensor experimental measurements. In section. 4.2.4, we apply an equivalent circuit method to self-consistently include the impact of both anode and cathode. In section 4.3, we validate our model by *in-vitro* experimental measurement results. In section 4.4, we discuss the fundamental impact of different design parameters of EBFC-based sensors on their detection performance. We show that the surface densities of oxidoreductase enzyme and electron transfer mediators have very different influences on the features of sensor output signal such as the sensitivity and the linear dynamic region. Furthermore, the cathodic reaction limits the magnitude of the sen-

sor output signal. In general, our equivalent circuit model can be easily adapted to solve the problems in other two-electrode redox amperometric systems, such as fuel cells [130], and other energy storage systems.

4.2 Model for EBFC-based Biosensors

4.2.1 Working Principle of EBFC-based Biosensors

We build our model based on a typical EBFC-based lactate biosensor as recently described in Bandodkar et, al [25]. Fig. 4.3 (a) summarizes the working mechanism of such a system wherein a lactate concentration dependent EBFC current output is transformed into a voltage signal using an external resistor for wireless data acquisition. Here the lactate present in the sample initiates a two-cycle synergistic redox reaction at the anode which includes first the enzymatic oxidation of lactate by the enzyme lactate oxidase (LOx) followed by an electron transfer reaction mediated by tetrathiafulvalene (TTF). The anode reaction is summarized as follows:

$$\text{Lactate} + \text{LOx (FAD)} \xrightarrow{k_F} \text{Pyruvate} + \text{LOx (FADH}_2\text{)} \tag{4.1}$$

$$\text{LOx(FADH}_2\text{)} + 2\text{TTF}^+ \xrightarrow{k_R} 2\text{TTF} + \text{LOx (FAD)} \tag{4.2}$$

$$2\text{TTF} \underset{k_{TTF,R}}{\overset{k_{TTF,F}}{\rightleftharpoons}} 2\text{TTF}^+ + 2e^- \tag{4.3}$$

Initially, the lactate molecules diffuse from the bulk solution towards the anode. Once they are captured by the LOx(FAD) enzyme, the enzymatic reaction in Eq. 4.1 occurs. Electrons are transferred from the lactate molecule through the two redox pairs (LOx and TTF in Eq. 4.1 and 4.2, respectively). Subsequently, the electrons are extracted from the TTF by the voltage dependent reaction in Eq. 4.3 and collected by the CNT electrode substrate.

The cross-coupling and complexity of enzymatic and mediator reactions at the anode influences the linearity, detection limit, and time-dependent evolution of sensor performance. Unlike traditional glucose sensors, however, the EBFC cathodic reaction

is also important. The electrons generated at the anode transfer through an external resistance and reach the cathode where dissolved O_2 gains the electrons and reduces to O^{2-} as the following:

$$O_2 + 4e^- \underset{k_{O_2,R}}{\overset{k_{O_2,F}}{\rightleftharpoons}} 2O^{2-} \tag{4.4}$$

Unlike a battery, the oxygen starvation in the cathode reaction plays an important role in dictating the linearity and limits of detection of EBFC sensors. Moreover, Eq. 4.3 and 4.4 are voltage dependent reactions, and we will see later in this chapter that their reactant-dependent voltage-partitioning have a dramatic effect on sensor response. In the next section, we are going to introduce mathematical models to describe the anodic and cathodic reactions.

4.2.2 3D Transient Modeling of EBFC-based Biosensor

As described in the previous section, the lactate molecules diffuse in the bulk biofluid solution and react with the enzyme immobilized onto the anode. The diffusion and reaction of lactate molecules subject to differential equation as:

$$\frac{d[C_3H_6O_3]}{dt} = D_L \nabla^2 [C_3H_6O_3] - k_F [C_3H_6O_3][\mathrm{LOx\,(FAD)}] \tag{4.5}$$

where D_L is the diffusivity of the lactate molecule in the bulk solution. k_F is the forward oxidation reaction constant in Eq. 4.1, and Eq. 4.6 to 4.9 describe the reaction fluxes for the analytes in the following two-cycle redox reactions:

$$\frac{d[\text{LOx (FADH}_2)]}{dt} = D_Q \nabla^2 [\text{LOx (FADH}_2)] + k_F [\text{C}_3H_6O_3] [\text{LOx (FAD)}] - k_R [\text{LOx (FADH}_2)][\text{TTF}^+] \tag{4.6}$$

$$\frac{d[\text{LOx (FAD)}]}{dt} = D_P \nabla^2 [\text{LOx (FAD)}] - k_F [\text{C}_3H_6O_3] [\text{LOx (FAD)}] + k_R [\text{LOx (FADH}_2)][\text{TTF}^+] \tag{4.7}$$

$$\frac{d[\text{TTF}]}{dt} = D_M \nabla^2 [\text{TTF}] + k_R [\text{LOx (FADH}_2)] \left[\text{TTF}^+\right] - k_{TTF,\ F}[TTF] + k_{TTF,\ R}[TTF^+] \tag{4.8}$$

$$\frac{d[\text{TTF}^+]}{dt} = D_N \nabla^2 \left[\text{TTF}^+\right] - k_R [\text{LOx (FADH}_2)] \left[\text{TTF}^+\right] + k_{TTF,\ F} [TTF] - k_{TTF,\ R}[TTF^+] \tag{4.9}$$

D_Q, D_P, D_M, and D_Q are the diffusion coefficient for enzyme LOx (LOx (FAD)-LOx($FADH_2$)), and the electron transfer mediator TTF-TTF^+ respectively. The two paired reactants (i) LOx (FAD) and LOx ($FADH_2$) and (ii) TTF and TTF^+ follow the mass conservation relation as:

$$[\text{LOxFADH}_2]+[\text{LOx(FAD)}] = \text{R}_0 \tag{4.10}$$

$$[\text{TTF}]+[\text{TTF}^+] = \text{K}_0 \tag{4.11}$$

where R_0 and K_0 are the total concentrations of LOx and TTF on the anode surface. On the cathode side, the oxygen reduction reaction follows similar flux and mass conservation equations:

$$\frac{d[O_2]}{dt} = D_H \nabla^2 [O_2] + k_{O_2,\text{R}}[O^{2-}] - k_{O_2,\text{F}}[O_2] \tag{4.12}$$

$$\frac{d[O^{2-}]}{dt} = D_F \nabla^2 [O^{2-}] + k_{O_2,\text{F}}[O_2] - k_{O_2,\text{R}}[O^{2-}] \tag{4.13}$$

$$[O_2] + [O^{2-}] = O_0 \tag{4.14}$$

where D_H and D_F are the diffusivity of O_2 and O^{2-}, $\text{k}_{\text{O}_2,F}$ and $\text{k}_{\text{O}_2,R}$ are the voltage dependent reaction constants from Eq. 4.4. O_0 is the total dissolved oxygen concentration near the cathode. Generation of one 1 mol of O^{2-} from the cathode consume

2 moles of electrons, which requires a consumption of 2 moles of TTF from the anode. Therefore, an additional electron balance equation between the anode and the cathode should be included as:

$$2\,[\mathrm{TTF}] = [\mathrm{O}^{2-}] \tag{4.15}$$

Note that the reaction constants from Eq. 4.5 to 4.9 and Eq. 4.12, 4.13 depend on the electrode potential that follow the exponential relationship defined by the Butler-Volmer equations as:

$$k_{TTF,F} = k_{0,A} \cdot \exp((E_A - E_{0,A})/\beta_{Ox,A}) \tag{4.16}$$

$$k_{TTF,R} = k_{0,A} \cdot \exp(-(E_A - E_{0,A})/\beta_{Red,A}) \tag{4.17}$$

$$k_{O_2,F} = k_{0,C} \cdot \exp((E_C - E_{0,C})/\beta_{Ox,C}) \tag{4.18}$$

$$k_{O_{2,R}} = k_{0,C} \cdot \exp(-(E_C - E_{0,C})/\beta_{Red,C}) \tag{4.19}$$

where $k_{0,A}/k_{0,C}$ are the reaction constant prefactor, E_A/E_C are the anode/cathode potential. $\mathrm{E_{0,A}/E_{0,C}}$ are the anode/cathode equilibrium potential, while $\beta_{\mathrm{Ox,A}}$, $\beta_{Red,A}$, $\beta_{Ox,\ C}$, $\beta_{\mathrm{Red,C}}$ are the Tafel slopes of the oxidation/reduction reactions on the anode and cathode respectively. Next, we will solve for Eq. 4.5 to 4.19 both numerically and analytically.

Based on the specific lactate sensor design parameters reported in Bandodkar et al. [25], Eq. 4.5 to 4.19 are solved numerically in a 3D coupled diffusion-reaction Finite Element Method (FEM) solver in *COMSOL.* The numerical simulation of the geometrical structure is shown in Fig. 4.2 (a) (i). The planar disk anode and cathode are located at the bottom of the unit cell. The anode is coated with two layers of redox reactants (LOx layer on top of the TTF layer). The reaction flux on the circular electrode surface is set to be $J_{rec} = k_F\,[\mathrm{C_3}H_6O_3]\,[\mathrm{LOx\ \ (FAD)}]$. The size of the unit cell (w: 4mm, l: 8mm, h: 1mm) represents a droplet of 0.032 mL biofuel sample solution. The bulk lactate concentration $\mathrm{L_0}$ is held fixed at the top surface of the

unit cell. We chose reflective boundary condition on the side surface of the unit cell. Preliminary studies reveal that increasing the size of the unit cell does not affect the results significantly.

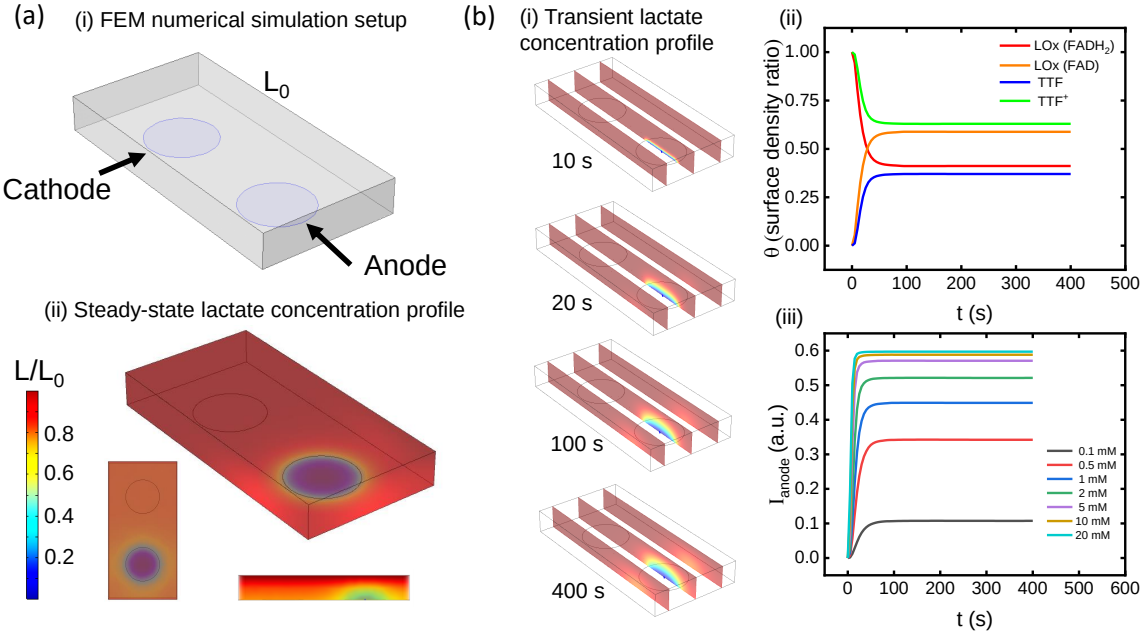

Fig. 4.2.: 3D Finite Element Numerical simulation. (a) (i) Simulation setup: disk planar cathode/anode at the bottom of the simulation system. (ii). Steady-state lactate concentration profile. (b). The transient re-sponse of EBFC sensor (i) Time sequence plot of lactate concentration. (ii) Surface density of interme-diate reactants. (iii) The transient output voltage from numerical simulation.

The numerical solution in Fig. 4.2 (a) (ii) shows the lactate concentration profile in the bulk cell in steady state. The lactate concentration depletes near the anode due to the lactate redox reaction. For the transient response, a time sequence of lactate bulk concentration is shown in Fig. 4.2 (b) (i). The time dependent surface density ratio of LOx (FAD), Lox ($FADH_2$), TTF, and TTF^+ are shown in Fig. 4.2 (b) (ii). After the transient phase lasting several tenth of seconds, the surface density of each species saturates to a constant value determined by the lactate concentration. The

total anode current generated from lactate reactions can be calculated by integrating the electron flux over the entire anode as follows:

$$I_{anode} = qN_A \int J_{e^-} dS \tag{4.20}$$

where N_A is the Avogadro constant and J_{e^-} is the electron generation flux. In Fig. 4.2 (b) (iii), we sweep the lactate bulk concentration L and record the anode current I_{anode}. The corresponding steady state response (current vs. concentration) shows that I_{anode} saturates to a constant value at high lactate concentration. The 3-D numerical model is an important contribution of this research because it can serve as a design tool for EBFC of arbitrary geometrical configuration and reaction rate constants.

4.2.3 Quasi-Steady State Analytical Model: Anodic Reaction Limited EBFC-based Sensor Response

A key insight from the numerical simulation is that diffusion limits do not play an important role in the range of analyte concentration of interest and the ultra-fast time-response itself is not of significant interest for relatively slow varying physiological signals (e.g. lactate concentration in blood). We can therefore neglect the diffusion delay terms from Eq.Eq. 4.5 to 4.19. In addition, we approximate the Butler-Volmer reaction constant in Eq. 4.17 and 4.18 as $k_{TTF,\,F} = k_P$ and $k_{TTF,R} = 0$ since the exponential voltage-dependence makes $k_{TTF,\,F} \gg k_{TTF,R}$. Remarkably, with these modest simplifications, Eq. 4.6 to 4.9 transforms into a coupled system of rate equation amenable to analytical simulation. The goal is to write simple but generalized equations suitable for EBFC-based biosensors to assist in design optimization and to identify system limits. The model results are validated against numerical simulation and experimental results to ensure that approach is justified.

$$\frac{dQ}{dt} = k_F LP - k_R QN \tag{4.21}$$

$$\frac{dP}{dt} = k_R QN - k_F LP \tag{4.22}$$

$$\frac{dM}{dt} = k_R QN - k_P M \tag{4.23}$$

$$\frac{dN}{dt} = k_P M - k_R QN \tag{4.24}$$

Here, P, Q, N, and M represent the surface density of LOx (FAD), LOx ($FADH_2$) , TTF, and TTF^+ since the diffusion of the chemicals across different layers on the electrode is ignored. R_0 and K_0 from Eq. 4.10 and 4.11 also reduce to the total surface density of LOx(FAD), LOx ($FADH_2$) , TTF, and TTF^+ respectively. We can solve Eq. 4.21 to 4.24 analytically in a normalized form by rewriting the parameters: $L^* = L/L_0$ (L_0 is chosen to be the upper limit of the lactate detection concentration), $P^* = P/R_0$, $Q^* = Q/R_0$, $M^* = M/K_0$, $N^* = N/K_0$, $t = \frac{t}{t_0} = \frac{t}{1/k_R K_0}$. In the steady state, we can set the reaction flux in Eq. 4.21 to 4.24 equal to zero. Including the mass conservation Eq. 4.10 to 4.11, the normalized form of the system of equations can be simplified as the following:

$$\frac{dQ^*}{dt^*} = -\frac{dP^*}{dt^*} = \alpha L^* P^* - Q^* N^* = 0 \tag{4.25}$$

$$\frac{dN^*}{dt^*} = \frac{\alpha}{\beta} QN - \beta M^* = 0 \tag{4.26}$$

$$P^* + Q^* = 1 \tag{4.27}$$

$$M^* + N^* = 1 \tag{4.28}$$

where $\alpha = \frac{k_F L_0}{k_R K_0}$ and $\beta = \frac{k_P}{k_R R_0}$ are unitless parameters derived from the combination of different sensor parameters.

By solving for Eq. 4.25 to 4.28 analytically, we can express the anodic current in steady state as the following:

$$I_{anode} = AqN_A \cdot k_P K_0 \cdot M^* = AqN_A \cdot k_P K_0 \frac{1}{2}\left(\Delta - \sqrt{\Delta^2 - 4\sigma}\right) \tag{4.29}$$

where Δ=$1+\frac{\alpha}{\beta}L^*+\alpha L^*$, $\sigma=\frac{\alpha}{\beta}L^*$. With $\frac{4\sigma}{\Delta^2}\ll 1$, Eq. 4.29 can be further approximated as the following:

$$I_{anode}\approx AqN_A\cdot\frac{k_PK_0}{1+\beta}\cdot\frac{L^*}{L^*+\frac{\beta}{(\beta+1)\alpha}} \tag{4.30}$$

This expression for EBFC-based sensor response has the same form as the Michaels-Menten equation where the term $\frac{\beta}{(\beta+1)\alpha}$ in the denominator determines the output linear dynamic range while the pre-factor $AqN_A\cdot\frac{k_PK_0}{1+\beta}$ dictates the sensitivity of the EBFC sensor.

Next, we calculate the output voltage signal measured across the external resistor. In an ideal case where the cathode can accept any number of electrons generated by the anode, i.e. there is enough dissolved O_2 at the cathode in the system, the overall EBFC output current is only limited by the anode reaction. The output voltage can be simply expressed as:

$$\psi_{total}=R\cdot I_{anode}+\psi_0 \tag{4.31}$$

where R is the external resistance, ψ_0 is the constant background signal generated by the parallel secondary reaction. Eq. 4.30 and 4.31 define the ultimate performance limit of EBFC-based biosensors.

4.2.4 Cathode-reaction Limited (Self-Consistent) Response

In practice, however, the anode-limited performance limit is seldom achieved: Fig. 4.3 (d) shows a cyclic-voltammetry experimental measurement result. In this measurement, we isolate the anode reaction by switching the cathode to a commercial Ag/AgCl reference electrode. We found that the linear dynamic range extends up to 50 mM which is higher than the original oxygen reaction cathode. This interesting phenomenon is due to the oxygen redox reaction at the cathode becomes the rate limiting factor due to the small amount of dissolved oxygen in the biofluid. In this

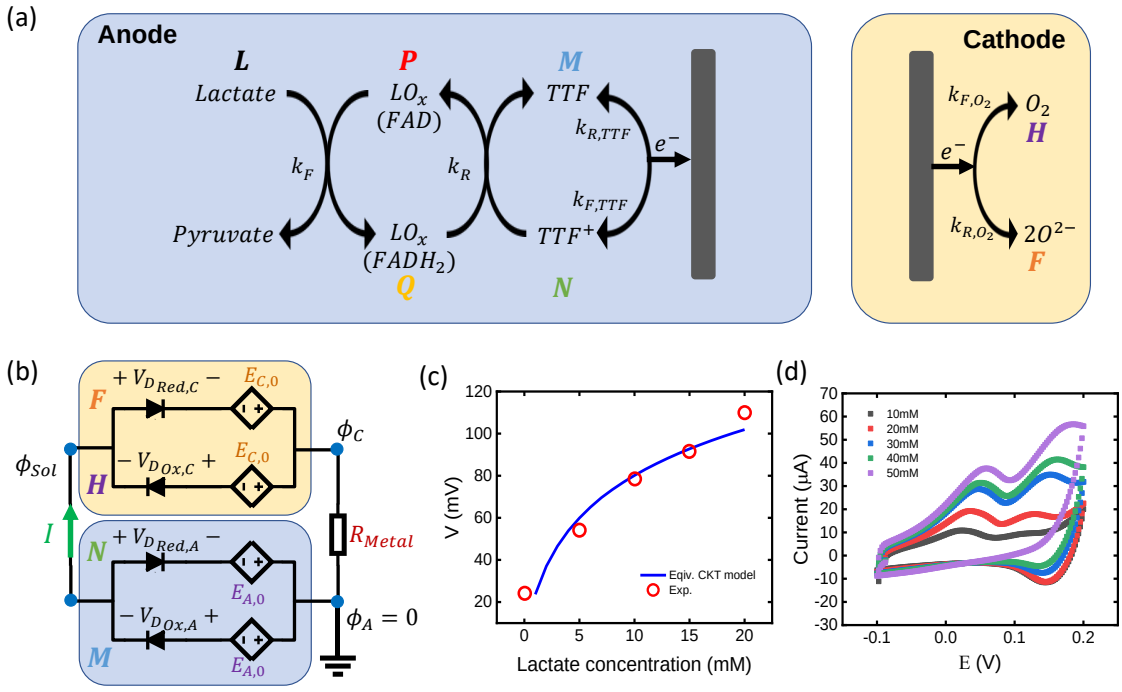

Fig. 4.3.: (a) Detection mechanism of bio-fuel lactate sensor. (b) Illustration of the equivalent circuit model. (c) The steady-state response of the equivalent circuit model (solid lines) calibrated against the experimental data (open circles). (d) CV measurement of anode against commercial Ag/AgCl reference electrode reactants.

section, we include the contributions from the coupled anodic and cathodic reactions shown in Fig. 4.3 (a) to generate a more accurate analytical model that resembles the real-life scenarios.

To include the effect of oxygen starvation, we solve the voltage dependent Butler-Volmer equations self-consistently as an equivalent circuit shown in Fig. 4.1 (b). Since the redox reaction current I is proportional to the reaction constants, the IV characteristics of the voltage dependent redox reactions at both anode and cathode can be viewed as an ideal diode in series with a constant voltage source (the value equals to the redox equilibrium potential E_0). The forward oxidation and reverse reduction reactions on both electrodes is then equivalent to two of such diode pairs

connected in parallel but in opposite direction. By applying this model to solve for the circuit equilibrium point where $I_{anode} = I_{cathode}$, we take care of all the voltage dependent reaction constants for both anode and cathode in a self-consistent way. No approximations (e.g. $k_{TTF,\ F} = k_P,\ k_{TTF,R} = 0$ in the previous section) are made in this condition. The sensor output voltage would be the exact solution of the voltage drop across the external resistor R in the equivalent circuit.

The voltage-drops driving anode and cathode reactions must be solved self-consistently. There is no explicit analytical expression for the self-consistent Butler-Volmer equivalent circuit in equilibrium. Here, we use MATLAB equation solver to find the implicit solution of the following system of equations plus the mass conservation Eq. 4.14 and 4.15:

$$I_{Anode} = I_{Ox,A} - I_{Red,A}$$
$$= qN_A \mathrm{k}_{0,\mathrm{A}} \left[\exp\left(-\frac{\psi_{Sol}+E_{A,0}}{\beta_{Ox,A}} \right) M \ - \exp\left(\frac{\psi_{Sol}+E_{A,0}}{\beta_{Red,A}} \right) N \right] \tag{4.32}$$

$$I_{Cathode} = I_{Red,C} - I_{Ox,C}$$
$$= qN_A \mathrm{k}_{0,\mathrm{C}} \left[\exp\left(\frac{\psi_{Sol}+E_{C,0}-I_{total}\cdot R_{Metal}}{\beta_{Red,C}} \right) H \ - \exp\left(\frac{I_{total}\cdot R_{Metal}-\psi_{Sol}-E_{C,0}}{\beta_{ox,C}} \right) F \right] \tag{4.33}$$

$$I_{total} = I_{Anode} = I_{Cathode} = qN_A \cdot k_F LP = qN_A \cdot k_R QN \tag{4.34}$$

where $I_{Ox,A}$, $I_{Red,A}$, $I_{Ox,C}$, $I_{Red,C}$ are the oxidation and reaction current at anode and cathode respectively. ψ_{Sol} is the electrical potential in the solution. M and N are the surface density of TTF and TTF^+ on the anode. H and F are the concentration of O_2 and O^{2-} near the cathode. They follow the mass balance and the electron balance equations from Eq. 4.11, 4.14 and 4.15 as: $M + N = R_0$, $H + F = O_0$, and $2N = F$.

Fig. 4.3 (c) shows the implicit solution of output voltage ψ_{c} of the Eq. 4.14, 4.15, 4.32 to 4.34 at different lactate concentration. It also shows the non-linear property of the output signal where the ψ_{C} saturate at higher lactate concentration.

4.3 Experimental validation of the Analytical Results

Next, we are going to validate our model against both the steady-state and transient response of the experimental measurement data from Bandodkar et al. [25] .The biofuel cell-based lactate sensor design consists of circularly cut carbon nanotube (CNT) paper as the anode. The CNT paper provides a conductive and high-surface area substrate to immobilize the oxidase enzyme and TTF for shuttling electrons from enzyme to CNT conducting paper.

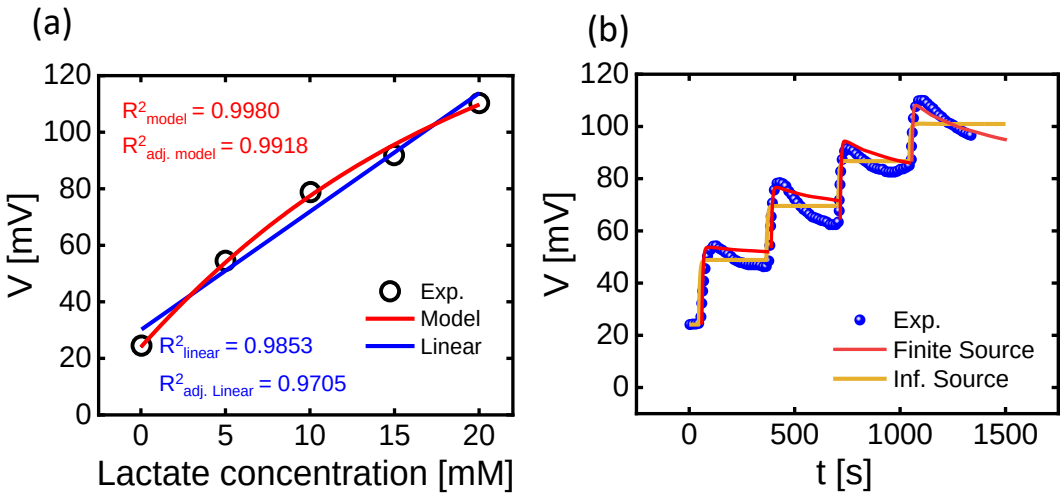

Fig. 4.4.: (a) Steady-state response from Exp. vs. analytical solu-tion vs. linear fitting. (b) Transient response of biofuel lactate sensor: exp. (blue dots) vs. model (red line: finite source setup, yellow line: infinite source setup).

4.3.1 Steady-state response

Fig. 4.4 (a) shows how our model interprets the steady-state lactate experimental data. Since the average concentration of lactate in sweat is around 14 mM, the *in-vitro* measurement take place in phosphate buffer (pH 7.0) solution with lactate concentration ranges from 0 mM to 20 mM with a 5 mM increment. By fitting the

unknown parameters (α, β, k_p, K_0.) summarized in Table 4.1, our simple single anode analytical model as described in section 4.2.4 captures the experimental data with high fidelity when there is enough oxygen supply at the cathode. At $c_L = 0$ mM, we find the constant background signal ψ_0 generated by the parallel reaction to be 22 mV. Our analytical model perfectly captures the non-linear response of the EBFC-based lactate sensor. Fig. 4.4 (a) shows a comparison between the traditional linear fitting vs. our model. The adjusted R^2 value increases from 0.97 to 0.99 and the root-mean square error reduce from 3.36 to 1.25.

Table 4.1.: Fitting parameters for analytical model

Fitting parameters		Known parameters	
α	1.378	r	1 mm
β	4.91	R	50 $k\Omega$
$k_p \cdot K_0$	$6.22 \times 10^{-5} mol/s/m^2$	A	πr^2

4.3.2 Transient response

Fig. 4.4 (b) shows the transient measurement data of the EBFC-based lactate sensor. The measurement starts from 0 mM lactate solution with a sequential 5mM lactate concentration increment up to 20 mM. For each concentration, the measurement lasts ∼300 s until the output voltage signal is stabilized. Here, we apply our numerical model to describe the sensor transient behavior. We keep fitting parameter (α, β, and γ) the same as the steady state model and increase the lactate concentration every 5 mM at t=45, 365, 706, and 1043 s. For the infinite source case (yellow solid line in Fig. 4.4 (b)), we use a constant lactate concentration at the top boundary as described in the numerical simulation section. When the sample concentration increases by 5 mM, transient voltage response jumps up and saturates to the steady-state value. In the experimental data, however, the voltage signal initially jumps up

to a larger value, and then decays slowly to a stable value. This interesting phenomenon is due to the finite lactate source in the sampling solution. The initial large jump corresponds to a large amount of lactate molecules instantly being introduced and mixed in the sample solution. The mixing adds additional convection causing the signal overshoot. Then the mixed solution reaches the steady state slowly with consumption of the lactate molecules by the EBFC-based lactate redox reactions in Eq, 4.28 and 4.6. In a new numerical simulation setup, we include the effects of finite lactate source by setting a constant initial lactate concentration in bulk solution. The simulation result in Fig. 4.4 (b) (red solid line) follows the trend of the signal decay.

4.4 Design Principles for EBFC

In the previous section, we have interpreted the experimental results of the steady-state and transient response of a BFC-based lactate sensor. In this section, we are going to explore the effect of some critical design parameters of the sensor. Based on our model prediction, we will provide design guidelines for improving the sensor performance.

For the biofuel-based sensor experimentalist, there are two important parameters that can be easily tuned during the sensor fabrication process: LOx surface density R_0 and TTF surface density K_0 on the working electrode. In addition, the dissolved oxygen level O_0 near the cathode is another important limiting factor for the biofuel sensor system.

4.4.1 Effect of enzyme surface density

Fig. 4.5 (a) shows the effect of enzyme (LOx) surface density R_0 on the enzyme-functionalized electrode of the biofuel cell-based sensor. In our analytical model, we increase R_0 from $5\times10^{-7} mol/m^2$ to $3\times10^{-6} mol/m^2$ while keeping the other parameters the same. *We find that an increase in the enzyme concentration R_0 increases the sensitivity in the linear dynamic region, but the non-linear curve saturates at a*

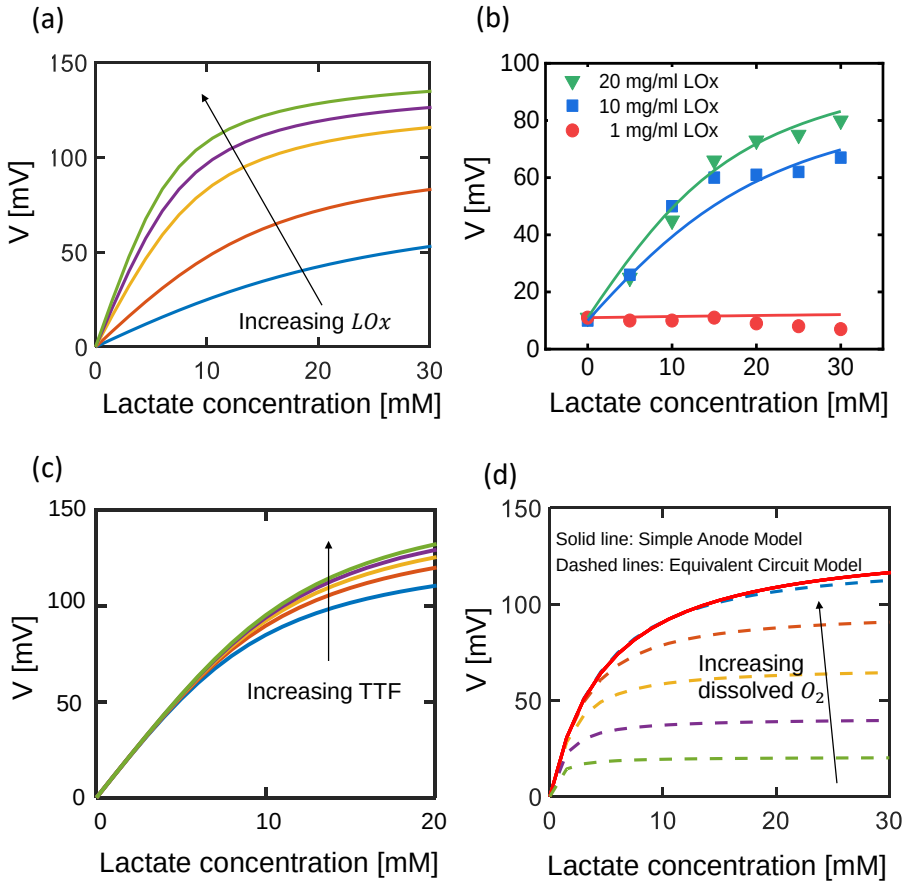

Fig. 4.5.: (a) The simulated parametric response of biofuel sensors. Potentiometric response of biofuel lactate sensor with different TTF surface density. (b) Experimental validation of the effect of surface density of LOx. (LOx layer is prepared by 1 mg/ml, 10mg/ml, 20mg/ml of LOx load solution) (c). Potentiometric response of EBFC lactate sensor with sweeping LOx surface density. (d)The impact of reactant concentration (dissolve ox-ygen) at the cathode of EBFC.

lower lactate concentration. Therefore, there is a trade-off between the linear dynamic range and sensitivity when tuning the enzyme surface density.

This interesting phenomenon has been validated by control experiment. Fig. 4.5 (b) shows the characterization results of three different EBFC-based lactate sensors

(dots) prepared by immobilizing 4 ng, 40 ng, and 80 ng of LOx. We calibrate our model to fit the experimental data by choosing LOx surface density R_0 the corelates to the amount of the immobilized LOx enzyme. Despite some small discrepancy at relatively low quantities (4 ng) of LOx loading, the results from the model correlates well with that from the experiments, thus illustrating the capabilities of the model to predict sensor performance.

4.4.2 Effect of electron transfer mediator surface density

In Fig 4.5 (c), we analyze the importance of TTF surface density K_0 in Eq. 4.11. We find that unlike the effect of R_0, increasing K_0 does not control the sensitivity of the EBFC output signal in the linear dynamic range. Instead, it increases the width of this linear dynamic range. Hence, experimentalists can manipulate this electron transfer mediator (TTF) density on their EBFC anode design to tune the linear dynamic range of the output signal without affecting the sensitivity.

4.4.3 Limiting effect of the cathode reaction

In section 4.4.1, we study the effect of enzyme surface density and electron transfer mediator surface density of the EBFC output response by assuming infinite oxygen supply from the cathode side from the self-consistent equivalent circuit model. Our model could also illustrate the effect of O_2 starvation on the cathode. The dashed lines in Fig. 4.5 (d) shows that when dissolved oxygen is insufficient, an increase in the dissolved O_2 near the cathode scales up the output signal at all lactate concentrations. The model predicts that the limiting effect of the cathodic reaction vanishes at dissolved O_2 concentrations above $\sim 10^{-5}\ mM$. Therefore, the dashed lines calculated from our equivalent circuit model approach the red solid line calculated from the simple single-anode analytical model where we assume that the redox reaction on the cathode is not the rate limiting factor. This is a unique feature of the EBFC-based sensor wherein the type of cathode redox reactions as well as the reactants should be

carefully chosen in order to reduce the impact of the cathode. Our equivalent circuit model provides a quantitative option for inspecting this interesting cathodic reaction.

To eliminate this oxygen-deficit limitation, several novel cathode designs have been reported in the literature. Jeerapan et al. use polychlorotrifluoroethylene (PCTFE), an oxygen-rich cathode material, to provide internal oxygen supply for EBFC cathode reduction reaction [131]. Yu et al. demonstrate a new solid-state Ag_2O/Ag cathode design which makes it possible for EBFC to operate under anaerobic condition [132]. Our model can easily adapt to quantitatively characterize the performance of such innovative EBFC cathode by calibrating the cathodic reaction constants as well as the concentration of different reactants in Eq. 4.7, 4.8, 4.24, and 4.27.

4.5 Conclusions

To summarize, we address the fundamental impact of different design parameters of EBFC-based sensors with sophisticated numerical modeling plus simple analytical formulas capturing the essential physics. We apply a self-consistent equivalent circuit method to couple the reactions for both the anode and cathode. Our model agrees closely with the experimental measurement data. We show that:

1. The *sensitivity* of the EBFC sensor could be enhanced by increasing the surface density of enzymatic layer (LOx). The electron mediator (TTF) does not affect the sensitivity.

2. The *linear dynamic range* of the steady state response is controlled by both the enzyme and the electron mediator, but in an opposite way. Increasing the surface density of oxidoreductase enzyme would shrink the width of linear region while an increase in the surface density of the electron mediator layer would enlarge it.

3. The redox reaction on the cathode is another limiting factor for the sensitivity of EBFC-based biosensor. In the specific case of lactate EBFC sensor, the *oxygen*

starvation effect is critical and should be carefully handled for the application of real-time wearable sweat lactate sensors.

Our self-consistent equivalent circuit method for Butler-Volmer relationship could applied to help optimize other two-electrode amperometric redox reaction systems such as battery design, metal corrosion problems, etc.

5. FUNDAMENTAL CHALLENGES, ESSENTIAL PHYSICS, SYSTEMATIC CHARACTERIZATION, AND DESIGN IMPROVEMENT OF ISE: PART I MODEL DESCRIPTION

5.1 Motivation

In chapters 2, 3, and 4, we have introduced new amperometric sensors that enhance sensitivity, increase stability, and reduce power consumption. The target analytes for amperometric sensors are usually charge-neutral such as glucose and lactate. Amperometric sensors detect the target analyte concentration by measuring the magnitude of the flow of electrons (current) generated by specialized redox reactions. For the detection of charged particles, however, we can use a simple approach based on potentiometric sensing by taking advantage of the electrostatic properties of the charge.

ISFET sensors described in chapter 1 use antibody-antigen reactions to fix the charged analyte such as protein and DNA on the liquid gate. The happed change are measured by the change in the drain current of the MOSFET. Still, this method relies on the specialized binding reactions which requires a sophisticated sensor structure. In this chapter, we will introduce and analyze another widely used potentiometric method that detects smaller charged particles: ions.

Potentiometric ion sensors use ion-selective electrode (ISE) to convert the activity of a target ion into measurable electrical potential signals. Conventional ISE sensor working electrode contain liquid contact (inner filling solution) between the ion-selective membrane(ISM) and the conducting metal electrode. Two-electrode measurement setup as shown in Fig. 5.1 (a) measures the chemical potential difference between the a working electrode and a reference electrode. The ion-selective

[0]At the time of the thesis deposition, this chapter is reproduced from a manuscript in draft.

membrane allows the target ion easily penetrate while blocking the other interfering ions, resulting in a capacitive interface. This capacitive interface generates a measurable potentiometric signal which reveals the activity of target ion.

Fig. 5.1 (b) shows a collection of in-lab steady-state measurement from a nitrate ISE sensor. We plot the steady-state response over four orders of magnitude of the sample nitrate ion concentration from $10^{-4}\ mM$ to $0.1\ mM$. Analytically, the Nernst equation determines this steady-state relationship between the target ion concentration and the sample-dependent potential:

$$\psi = \mathrm{E}_0 + \frac{kT}{zq}\ln\left(\frac{n}{n_0}\right) \tag{5.1}$$

where E_0 is the standard potential, k is the Boltzmann's constant, T is the temperature, z is the ion charge number, n is the target ion concentration, and n_0 is the standard ion concentration associated with E_0. According to the Nernst equation, the sensitivity of an ideal ISE at room temperature $T = 25°C$ should be $\frac{kT}{q} \sim\ 60\ mV/dec$ (for ion charge number: $z = 1$).

5.2 The detection mechanism of ISE

The key component of ISE is the ion-selective membrane (ISM). The chemical component of ISM is specially designed so that the target ion can easily penetrate or leach out from the membrane. A dipole forms at the sample-ISM phase boundary. Based on the material of the ISM, two main categories of polymer ISM are primary used for solid-contact ISE: ion-exchange ISM (Fig. 5.1 (a)-I) and ionophore ISM (Fig. 5.1 (a)-II). Ion-exchange ISM is based on special organic polymer membrane which contains specific ion-exchange substrate (e.g., TOA^+ being used in the design of soil nitrate sensor) accounting for the selectivity to certain ion. On the other hand, ionophore ISM uses large molecules called ionophore to bind with target ions (e.g., Na^+, K^+ sweat sensor). The selectivity come from the specialized target binding reaction between the ionophore and the ion. The target ion can either hop

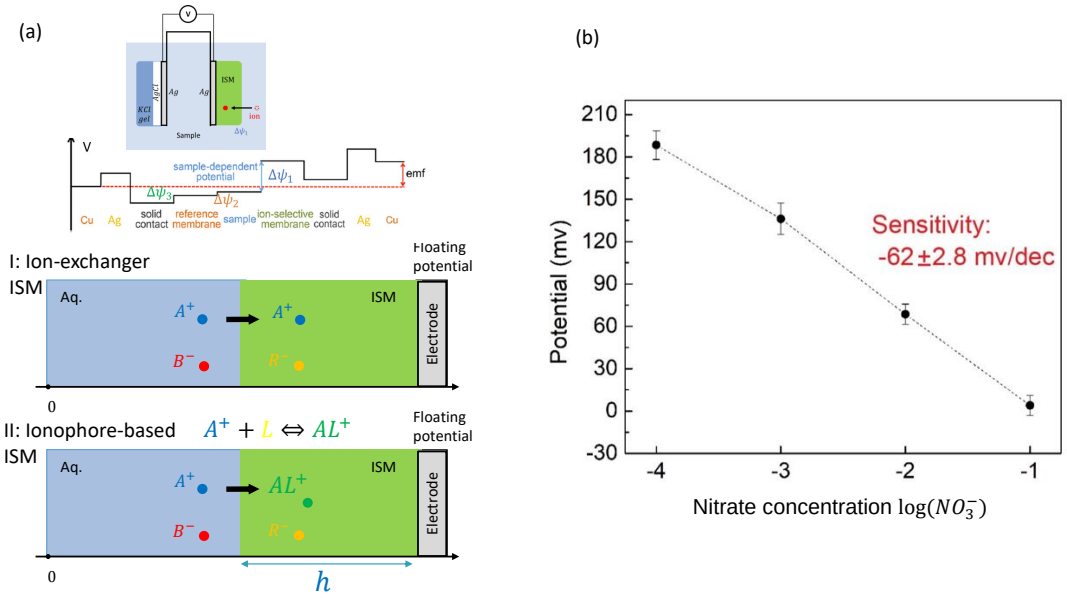

Fig. 5.1.: (a) Schematic illustration of the potential distribution profile within two-electrode cell. [133] The sample-dependent potential occurs at the sample-ISM interface. Two types of ISM: ion-exchanger and ionophore-based. (b) Steady-state response of nitrate ISE sensors

through different ionophore sites (immobile ionophore) or the bonded ion-ionophore pairs which are free to move in the polymer ISM (mobile ionophore) shown in Fig. 5.1 (a).

From our theoretical study, ISE has two different modes of operation:

1. **Depletion mode.** Most ion exchange ISM operates in this mode. The membrane is preloaded with a high level of ions. When sensing in a low concentration sample solution, the preloaded ion release from the ISM into the sample which forms a diploe at the phase boundary.

2. **Accumulation mode.** Most ionophore-based ISMs operate in this mode. Ions from the sample react with the ionophore embedded in the membrane and accumulate at the membrane side of the phase boundary.

The physics behind of those two modes are similar. The difference is that the dipole at the phase boundary form in the opposite direction.

5.3 Solid-contact ISE

The performance of conventional ISE is highly sensitive to the sensor operation conditions (such as temperature and air pressure) since the evaporation of the inner filling solution would affect the accuracy of the measurement. Therefore, the conventional liquid-contact ISE sensors are commonly used for in-lab measurements.

To implement ISE into portable integrated devices, several limits of conventional ISE need to be overcome: 1) poor sensitivity with small sample solution volume, 2) solution-induced instability of transduced signal, 3) inadequate selectivity to the target ion over a wide variety of interfering ions, and 4) low throughput manufacturing capability. Solid-contact ISEs and reference electrodes are good candidates for IoT applications such as wearable personalized healthcare systems (sweat sodium/potassium ion sensors), precision agriculture soil monitoring systems (nitrate/chloride ion sensor). The first generation of the solid-contact ISE is called coated-wire ISE [134]. The ISM is directly coated on top of the metal wire electrode, generating a purely capacitive interface. However, it has been widely reported in the literature that the coated-wire ISE pick up noise easily, show large output voltage drift, and exhibit significant sensor-to-sensor variations.

With the help of nanotechnology, the creation of new flexible material, and the development of new printing technology enable engineering of low-cost, easily foldable thin-film, lightweight, thin-film flexible ISE to overcome the challenges of the coated-wire ISE.

Fig. 5.2 (a) shows an example of a thin-film nitrate ISE sensor that consists of both solid-contact working and reference electrodes. The working and reference electrodes are fabricated by roll-to-roll (R2R) printing technology in a layer-by-layer manner on a thin-film flexible substrate. A nitrate ion-selective membrane layer is coated on the

active area of the silver working electrode. The target nitrate ions form a capacitive interface inside the membrane which determines the sample-dependent potential. Similarly, a gel membrane with a constant chloride level is coated on the active area of the reference electrode. This constant chloride ion concentration guarantees a constant interface potential at the reference electrode achieved by the reversible redox reaction: $\mathrm{AgCl}\,(s) + \mathrm{e}^- \rightleftharpoons \mathrm{Ag(s)} + Cl^-$. Details about the R2R fabrication process can be found in Appendix C.

The solid-contact thin-film ISEs shows the following advantages:

1. Due to the near-zero current operating conditions, thin-film solid-contact ISE potentiometric sensors have the advantage of low power consumption which meets the long lifetime requirements for portable integrated electronic devices.

2. Roll-to-roll (R2R) scalable nanomanufacturing technology enables thin-film solid-state ISEs to be created with high throughput and low cost. The design parameters of the thin-film electrode (ISM thickness, ISM chemical components, etc.) can be easily tuned by the R2R manufacturing process (e.g., rolling speed, membrane coating, solvent drying)

For an in-lab measurement, the ISEs are normally preconditioned and calibrated in a high concentration known target ion solution for several hours until a stable output signal has been achieved. The transient process before the initial steady-state have not been discussed extensively in the literature. Fig. 5.2 (b) shows the transient response of 12 thin-film nitrate ISE in a constant nitrate solution in the preconditioning phase. Each ISE takes $> 10\ hrs$ to reach a stable output voltage value. Therefore, several new challenges need to be overcome before the solid-contact ISE could be implemented into IoT applications:

1. **Response time.** Current theoretical studies focus on the steady-state response, but transient response including preconditioning step before the measurement is equally important. Understanding this transient response (response

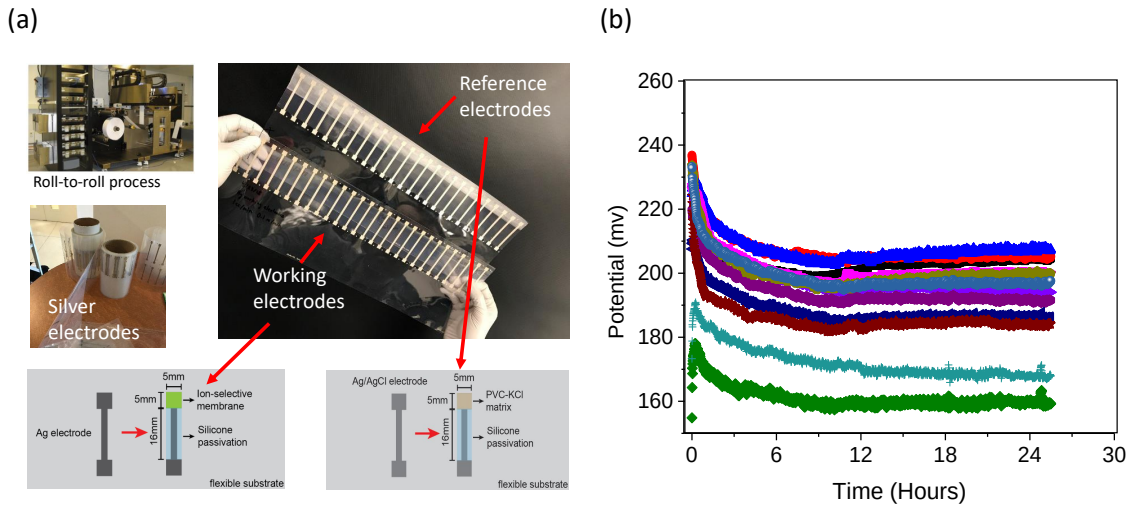

Fig. 5.2.: (a) Roll-to-roll printed thin-film nitrate ISE sensor that consists of both solid-contact working and reference. (b) Transient response of multiple R2R printed ISE nitrate sensors.

time, the pattern that the signal follows as a function of time) is critical for closed-loop continuous monitoring applications.

2. **Trade-off between low cost and sensor performance.** There are significant sensor-to-sensor variations for both steady-state and transient output response. The nitrate sensors are fabricated by the R2R technology, therefore the variations during the fabrication process (nonuniform coating of ion-selective membrane, silver electrode roughness and resistance variation, etc.) are reflected in the variations of potentiometric output signals among sensors. Reducing the variability and retaining a stable output signal with high precision remains a problem.

3. **Signal to noise ratio.** Since the ISE sensors are operating in a harsh environment for IoT applications, there is a wide variety of noise source that

could potentially superimpose fluctuations on the original sensor output signal. The the noise signal strength should be orders of magnitude smaller than the resolution of the sensing signal.

In this chapter and the next chapter, we will ask and answer the following questions derived from our in-lab experimental observations: i) Even though the Nernst equation well-explain the steady-state response with the sensitivity of $60mV/dec$, the systematic theory for the transient response of ISE is missing. What pattern should the transient response follow? ii) What is the physics behind this pattern? How long should one wait until the potentiometric signal get stabilized? Which design factors control the time constant of the transient response? iii) In the long-term measurement, there are variations (noise and drift) despite the change of ion concentration. What is the source (non-ideal effects) of those variations? How to reduce the variation?

5.4 Kinetic modeling framework

Traditional theoretical work of ISE focus on improving the steady-state response of ISE. The models reported in the literature [135] simplifies the microscopic ion penetration process in the ISM with the following assumptions:

1. **Charge neutrality.** Morf et al. [135] assumes that the cations and anions in all the regions are well balanced. This requests counter-ions are locally available to balance the charge associated with the target ion. Net charge is ignored everywhere at the sample-ISM phase boundary. A detailed systematic physics-based model is needed to explain this dipole formation.

2. **Step function approximation of phase boundary potential.** As shown in Fig. 5.1 (a), experimentalists in the literature usually approximate the emf potential profile at the phase boundary as a discrete step function. The step function is determined by the concentration difference between the two phases.

This approximation holds in the macroscopic scale. But in the microscopic scale (a few nanometers near the phase boundary interface), the phase boundary potential profile should be continuously distributed across two different materials due to the unbalanced charges from the dipole.

3. **Ignore ion drift** Molf's model only includes the diffusion flux due to the gradient of ion concentration. This assumption is based on the charge neutral approximation in 1). Here, one assumes that the driving force for target ion transport only arises from the concentration gradient generated inside different phases. If a dipole forms at the phase boundary, however, the unbalanced charge is going to interfere the local emf voltage according to Poisson's equation. Therefore, this unbalanced charge will lead to an electrostatic drift force for different charged ions.

In this section, we are going to introduce a new kinetic model which includes the contribution of detailed transportation process of all the ions near ISM boundary.

Modeling of ion transport processes near the sample to the ion-selective membrane region is shown in Fig. 5.3 (a). We coupled the drift-diffusion equation, Poisson's equation, and the charge balance equation in a simplified one-dimensional domain.

$$\frac{\partial n_i(x,t)}{\partial t} = \frac{\partial}{\partial x}(\mu_i(x)\ n_i(x,t)\frac{\partial \psi(x.t)}{\partial x} + D_i(x)\frac{\partial n_i(x,t)}{\partial x}) \tag{5.2}$$

$$\frac{\partial^2 \psi(x,t)}{\partial x^2} = -\frac{q \cdot n(x,t)}{\kappa \epsilon_0} \tag{5.3}$$

$$\rho = qN_A \cdot \textstyle\sum_i z_i n_i \tag{5.4}$$

where $n_i(x,t)$ is the concentration of ith ion, $\mu_i(x)$ and $D_i(x)$ are the location dependent mobility and diffusivity of the ith ion, ψ is the local potential, and κ is the relative dielectric constant, N_A is the Avogadro constant, z_i is the charge number of the ith ion.

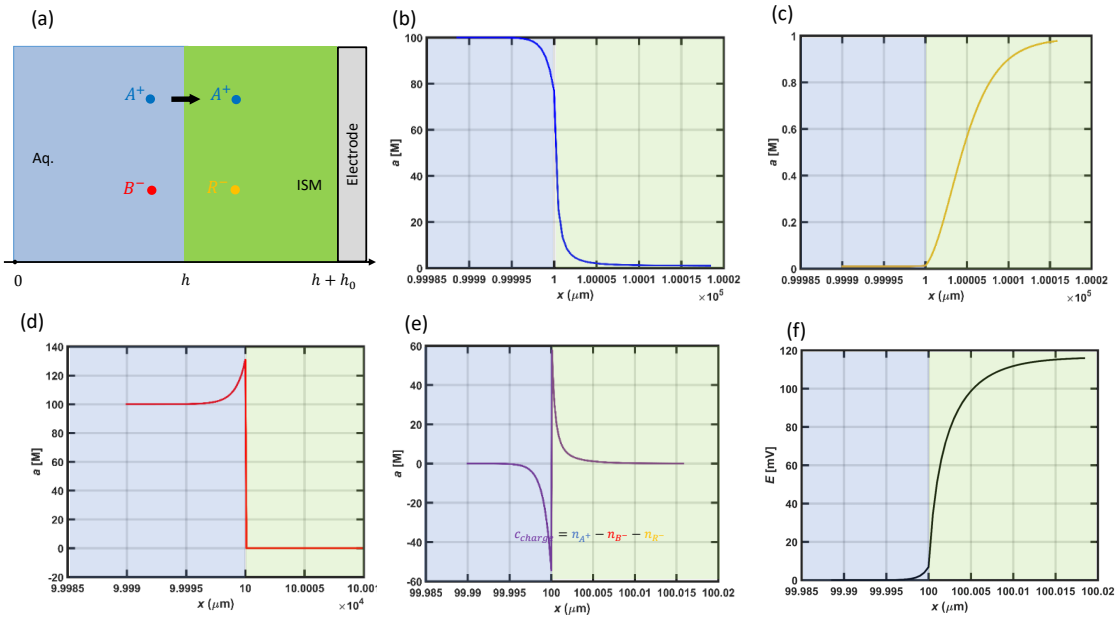

Fig. 5.3.: (a) 1D numerical simulation set up of a two-region sample/ISM structure. (b)-(d): the spatial distribution of target ion A^+, and counter ions R^- and B^- in steady-state. (e) The net charge of A^+, R^- and B^- form a dipole at the phase boundary. (f) The distribution of the phase-boundary potential near the sample/ISM interface.

5.4.1 Numerical steady-state solution

We numerically solve the ion transport Eqs. 5.2 to 5.4 by COMSOL FEM simulator. In Fig. 5.3 (a), $x = h_0$ and $x = h_0 + h$, correspond to the sample/membrane and the membrane/metal electrode interfaces, respectively, where h_0 is the thickness of the ISM. At the sample domain $0 < x < h_0$, we set constant ion concentration $n_{i,0}$ for each ion. Because ions cannot further penetrate the metal electrode, we apply reflective boundary condition and floating potential at the membrane/conductive electrode boundary. In this simulation, we focus on three different ions: 1) A^+ the sensing target ion, 2) B^- the counter ion in the sample, and 3) R^- the counter ion in the ISM. A^+, B^- and R$^-$ are free to move in the sample solution with

$D_{aq,A} = D_{aq,B} = 10^{-9} m^2/s$. Indeed, A^+ can penetrate into the membrane with $D_{M,A} = 10^{-11} m^2/s$ while B^- cannot with $D_{M,B} = 0\ m^2/s$

In this numerical simulation, the voltage distribution profile within the two-region system as well as the ion concentration profile are recorded in each simulation time step. Fig. 5.3 (b)-(d) shows the spatially distributed ion concentrations for A^+, B^- and R^- respectively. The primary ion A^+ travel from the solution into the membrane, causing the depletion of A^+in the solution outside the membrane and the accumulation of A^+ at the inner boundary. Similarly, R^- ions deplete from the membrane side and are released into the solution as shown in Fig. 5.3 (c). There is an accumulation of B^- in the solution near the boundary because if $D_{aq,B} \gg D_{M,B}$ so that B^- could quickly be dissolved in the solution. Fig. 5.3 (d) shows an accumulation peak of B^- counter ion in the solution phase near the sample-ISM. Because of this non-uniform distribution of A^+, B^- and R^-, the net charge $n_{net} = n_{A^+} - n_{B^-} - n_{R^-}$ form a dipole at the phase boundary shown in Fig. 5.3 (e), resulting in a phase boundary potential. As shown in Fig. 5.3 (f), the microscopic scale of the phase boundary potential distribution is asymmetric due to the diffusivity difference of the ions, with a major potential drop in the membrane phase and minor potential drop in the sample solution phase. But on the macroscopic scale, this potential destitution looks like a step function. The step-function approximation for the phase boundary potential [135] has been widely adopted by the literature from the ISE community.

Our numerical simulation also shows that when the ion concentration (both A^+ and B^-) increases by one order of magnitude, the phase boundary potential increases by $60mV$. This observation is well aligned with the steady-state Nernst equation. Interestingly, the physics behind the phase boundary potential vs. ion concentration is the same as the physics of the built-in potential of a PN junction. (e.g., PN junction built-in potential has a $\frac{\mathrm{kT}}{\mathrm{q}} = 60mV/dec$ relation with the semiconductor doping density.)

5.4.2 Numerical transient response

In the previous section, we have successfully applied our numerical simulation framework to solve for the steady-state response of the ISE. The accuracy of the numerical model has been validated by the Nernst equation. From our model, we have gained a good physical insight into the microscopic ion distribution and how the phase boundary potential is generated. Next, we are going to apply our numerical simulation framework to explore the transient response of ISE before it reaches the steady-state output voltage.

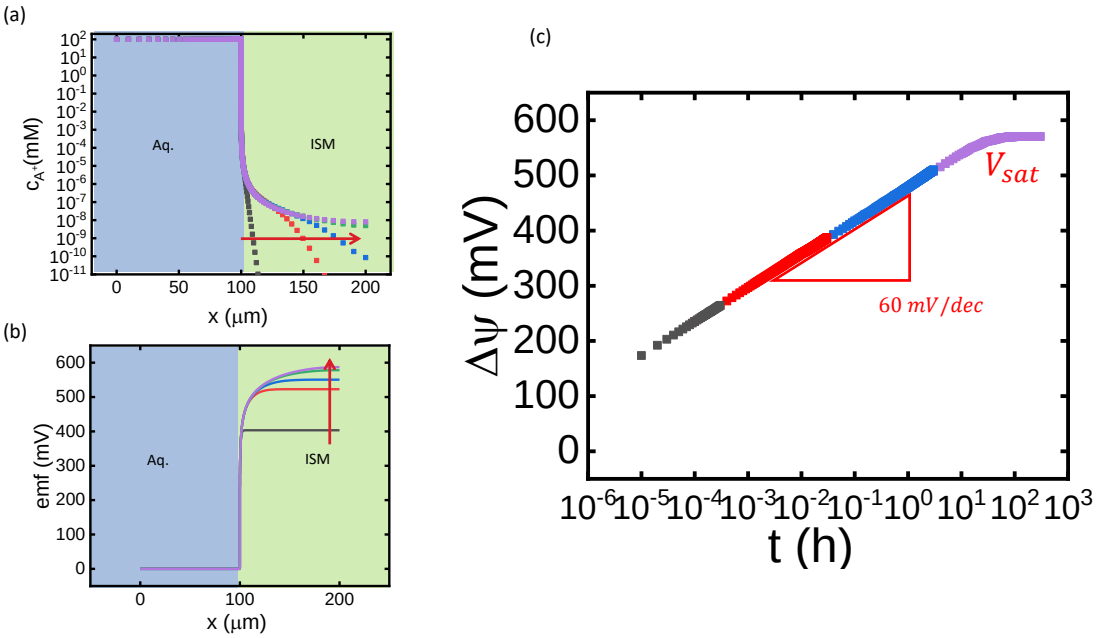

Fig. 5.4.: Time series plot of (a) the primary ion A^+ and (b) the corresponding potential distribution within the sample-ISM simulation region. (c) Semilog x plot of the total phase boundary potential $\Delta\psi$ across the sample-membrane region as a function of time.

In Fig. 5.4 (a) and (b), we plot the concentration of the primary ion A^+ and the phase boundary potential at different time steps of the numerical simulation before the system reaches the steady-state. Fig. 5.4 (a) shows that in a semi-log

y plot, the "diffusion tail" of the primary ion gradually penetrates the membrane. Although the absolute value of the diffusion tail concentration is orders of magnitude smaller than that of the concentration at the interface, the space-integrated charge is significant. It gives rise to an evolution of the phase boundary potential increase. In Fig. 5.4 (c), we plot the total phase boundary potential $\Delta\psi$ across the sample-membrane region as a function of time. We found that in a semi-log x plot before saturation, $\Delta\psi$ increases linearly as a function of time, which indicates a logarithmic relationship between $\Delta\psi$ and t. Surprisingly, the slopes of $\Delta\psi$ vs. log(t) is also 60 mV/dec. This interesting observation suggests that the coefficient before the log(t) in the analytical expression might be $\frac{\mathrm{kT}}{\mathrm{q}}$. Furthermore, this constant transient slope in the time scope is universal, independent on the targe ion concentration and other sensor design parameters. Why does the Nernst-like relationship still hold for the relationship between the phase boundary potential and time? We are going to answer this question in the next section by analytically solving Eqs. 5.2 to 5.4 and derive a new physics-based analytical model.

5.4.3 Approximate analytical solution

We solve the coupled drift-diffusion and poison's equation analytically with the same boundary conditions from the numerical simulation setup. At the beginning of the transient phase, the built-in potential ψ inside the membrane is relatively small. Therefore, we can ignore the drift term in Eq.5.2. The ion flux becomes:

$$\mathrm{J} = q \cdot D\frac{dn}{dx} = q \cdot D\frac{\Delta n}{\Delta x} = q \cdot D\frac{\mathrm{n_0} - n^*}{\Delta x} \tag{5.5}$$

where n^* is the number of ions just transferred into the membrane following the Arrhenius equation: $n^* = n_0 \cdot e^{-\frac{q\psi}{kT}}$. Δx is the diffusion width. The electrical conductivity of the membrane can be calculated from the ion flux as:

$$\sigma = \frac{dJ}{dE} = \frac{dJ}{d\psi}\ \frac{d\psi}{dE} = qD \cdot n_0 \left(\frac{q}{kT}\right) \cdot e^{-\frac{q\psi}{kT}} \tag{5.6}$$

Here the approximation is that $\frac{d\psi}{dE}$ equals to the diffusion length x_0. The length of time to reach this conductivity value would be:

$$t = C \cdot \frac{\kappa\epsilon_0}{\sigma} = \frac{kT}{q} \cdot \frac{\kappa\epsilon_0}{qDn_0} \cdot e^{\frac{q\psi}{kT}} \tag{5.7}$$

We can rewrite the Eq. 5.7 and find out the built-in potential as a function of time as:

$$V_{trans}(t) = \psi = \frac{kT}{q} \ln\left(C \cdot \frac{t}{t_0}\right) \tag{5.8}$$

where $t_0 = \frac{kT}{q} \cdot \frac{\kappa\epsilon_0}{qDn_0}$ is a time scaling factor. Eq. 5.8 shows that by scaling the time with t_0, all the transient response of ISE output potential signal (with different membrane dielectric constant ϵ, different diffusivity D) would converge to a universal curve. In the semi-log x-axis plot, the slope of this universal curve is $\frac{kT}{q} = 60mV/dec$ at the room temperature.

Similarly, we can solve Eq. 5.2 and 5.3 in the steady-state by setting $\frac{\partial n(x,t)}{\partial t} = 0$. The final expression for the saturation voltage is:

$$V_{sat} = \frac{kT}{q} \ln\left(C_1 \frac{n_0 h^2}{\kappa}\right) + \mathrm{C}_2 \tag{5.9}$$

Eq. 5.9 is a more general form of Nernst equation (Eq. 5.1). It also includes the impact of membrane thickness h and dielectric constant κ of the membrane material. The saturated steady-state value of measured emf is proportional to the logarithm of h^2(120 mV/dec) and inversely proportional to the logarithm of κ (-60mV/dec).

We can estimate the critical time for ISE to reach saturation by equating Eq. 5.8 and Eq. 5.9:

$$t_c = C_0 \cdot \frac{kT}{q} \cdot \frac{\epsilon_0 h^2}{qD} \cdot e^{\frac{qC_2}{kT}} \tag{5.10}$$

This critical time depends on the thickness h of ISM and ion diffusivity D inside the membrane material but independent of ion concentration and the relative dielectric constant.

To derive a compact analytical model for both transient and steady-state phase, we use the following mathematical expression to connect Eq. 5.8 and Eq. 5.9. We calibrate our compact model against the numerical model/experimental measurement by tuning the fitting parameter β:

$$V_{ana}(t) = \frac{V_{trans}\,(t)}{\left(1 + \left(\frac{V_{trans}(t)}{V_{sat}}\right)^{\beta}\right)^{\frac{1}{\beta}}} \tag{5.11}$$

5.4.4 Analytical model for ISM with pre-loaded constant ion concentration

In the previous approximate analytical solution, we ignored the drift term in Eq. 5.2 since the initial voltage ψ_0 is small. If we change the concentration of ions after the preconditioning phase, however, there is an initial voltage build-up ψ_0. Therefore, the drift term in Eq. 5.2 should also be included as the following:

$$J_{drift} \sim q\mu n_0 \, \frac{-\psi}{x_0} \tag{5.12}$$

where ψ is the local phase boundary potential, x_0 is the spread distance of ψ. For approximation, we treat this spread distance as a constant.

For the diffusion flux, we made the following approximation:

$$J_{diff} \sim \frac{qD}{x_0} \cdot (n_1 - n_0) \cdot e^{-\frac{q(\psi - \psi_0)}{kT}} \tag{5.13}$$

where n_0 and ψ_0 are the initial preconditioning ion concentration and the corresponding saturated phase boundary voltage respectively.

The total flux can be written as the sum of the diffusion flux and drift flux as the following:

$$\mathrm{J} = q\mu n_0 \frac{-\psi}{x_0} - \frac{qD}{x_0} \cdot (n_1 - n_0) \cdot e^{-\frac{q(\psi-\psi_0)}{kT}} \tag{5.14}$$

Similar to the approximate solution, the electrical conductivity of the membrane can be calculated from the ion flux as:

$$\sigma = \frac{dJ}{dE} = \frac{dJ}{d\psi}\frac{d\psi}{dE} = -q\mu n_0 - qD\left(-\frac{q}{kT}\right)(n_1 - n_0)e^{-\frac{q(\psi-\psi_0)}{kT}} \tag{5.15}$$

where $\frac{d\psi}{dE} = x_0$ which cancel the x_0 in Eq. 5.14. The time to reach a constant potential would be:

$$t = C \cdot \frac{\kappa\epsilon_0}{\sigma} \tag{5.16}$$

If we rearrange the terms of Eq. 5.16, the final expression for the phase boundary potential would be:

$$\psi = \frac{kT}{q}\ln\left(\frac{tq\mu\,(n - n_0)}{C \cdot \kappa\epsilon_0 + tq\mu n_0} + 1\right) + \psi_0 \tag{5.17}$$

We can check the two limits of Eq. 5.17. When $t = 0$ the logarithmic term diminished, ψ=ψ_0. When $t\to\infty$, $\psi = \frac{kT}{q}\ln\left(\frac{(n_1-n_0)}{n_0} + 1\right) + \psi_0 = \frac{kT}{q} \cdot ln\left(\frac{n_1 h^2}{\kappa}\right) + C_0 = \psi_1$. The two limits well align with the approximation result from Eq. 5.9.

5.5 Model validations

5.5.1 Numerical validation

In Fig. 5.5 (a), we plot the potential difference across the ion-selective membrane $\Delta\psi$ as a function of simulation time. We normalize the time by the scaling factor

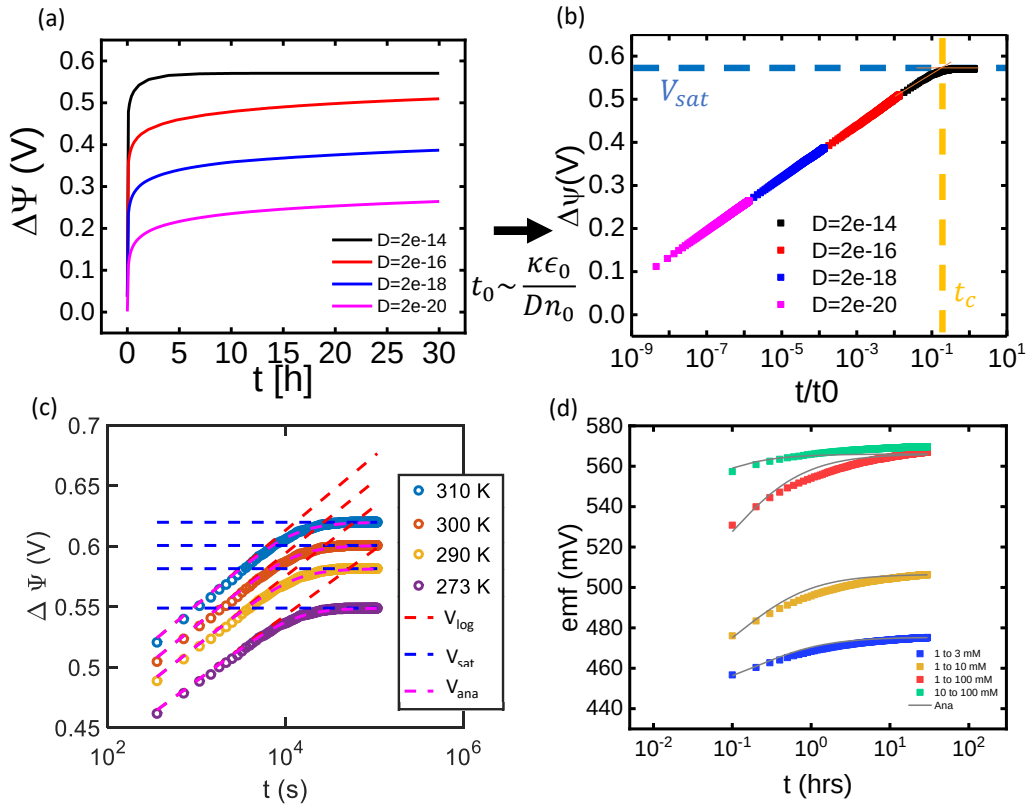

Fig. 5.5.: (a), Numerical simulation of potential difference across the ion-selective membrane $\Delta\psi$ as a function of simulation time. (b) Normalization of transient numerical simulation result by scaling factor t_0. (c) and (d) numerical(dots) validation of analytical model (solid lines).

$t_0 = \frac{kT}{q} \cdot \frac{\kappa\epsilon_0}{qDn_0}$ as suggested by the analytical model, the transient response of ISE with different diffusivity values collapse into a single universal curve in Fig. 5.5 (b). In the semi-log x axis plot, $\Delta\psi$ increases linearly with the normalized time, which indicate a logarithmic relation between $\Delta\psi$ and t. After the critical time t_c, all the curves began to saturate to a constant potential V_{sat}. This constant V_{sat} value is the steady-state response of ISE reported in the literature by Eq. 5.1 (Nernst equation).

Fig. 5.5 (c) and (d) shows that our analytical model form Eq. 5.11 and Eq. 5.17 (solid lines) follows the numerical simulation results (dots) well.

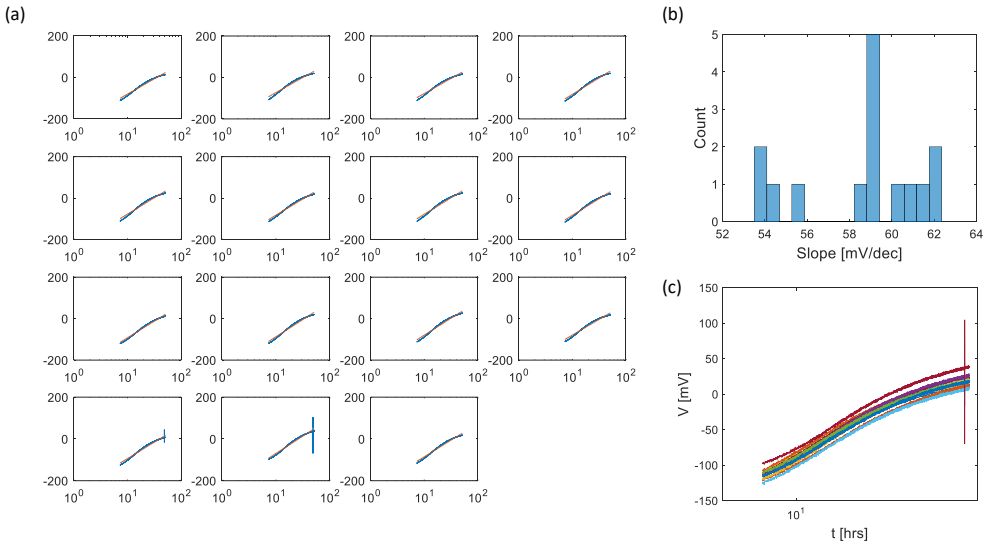

Fig. 5.6.: (a) logarithmic fitting for 15 preconditioning transient experimental measurements. (b) transient slope distribution of the 15 transient measurements. (c) Transient response of 15 ISE in a single plot.

5.5.2 Experimental validation

In Fig. 5.6 (a), we apply the logarithmic fitting for 15 preconditioning transient experimental results. The experimental results are taken from 15 thin-film roll-to-roll printed ISE sensors measured against a commercial reference electrode for ∼24 hours. We record the transient slope (the coefficient before the log) and plot the distribution in as a histogram in Fig. 5.6 (b). We find the transient slope is distributed near 60 mV/dec with a small variance. This observation confirms the generalized Nernst relationship in time as predicted by our new model.

In Fig. 5.6 (c), we plot all the transient measurement results in the same plot. We found that even within the same measurement dataset, the absolute value of the ISE output emf voltages shows large offsets in the vertical direction. We are going to discuss those non-ideal effects and the possible explanations in the next chapter 6.

5.6 Conclusions

Validated by both numerical simulation and experimental data, we offer a new physics-based modeling framework that captures the essential microscopic ion transportation process as well as the macroscopic steady-state and transient potentiometric output of ISE. In the next chapter, we are going to use our model to provide useful design guidelines to optimize sensor performance.

6. FUNDAMENTAL CHALLENGES, ESSENTIAL PHYSICS, SYSTEMATIC CHARACTERIZATION, AND DESIGN IMPROVEMENT OF ISE: PART II NON-DEAL RESPONSE

6.1 Introduction

In chapter 5, we developed a new physics-based modeling framework to capture the essential microscopic ion transportation process as well as the macroscopic steady-state and transient potentiometric responses of thin-film solid contact ISE. In this chapter, we are going to discuss the challenges for ISE IoT applications and the corresponding strategies that overcome the problems in the following topics: selectivity of ISE, statistical study of the noise signal, ISE membrane degradation, ISM thickness variations and non-uniform coating, super-Nernst transient response, and strategies to predict and reduce ISE sensor-to-sensor variations and response time.

6.2 Selectivity of ISE

In this section, we are going to explore the physical mechanism behind the selectivity of ISE. As mentioned in chapter 5, there are two basic types of ion-selective membrane: i) ion-exchange ISM and ii) ionophore-based ISM. The selectivity mechanism is slightly different for the two cases.

6.2.1 Ion-exchange ISM

For the ion-exchange ISM shown, the selectivity of the ion-selective membrane comes from the different diffusivity among various ions in the ISM. The membrane

[0]At the time of the thesis deposition, this chapter is reproduced from a manuscript in draft.

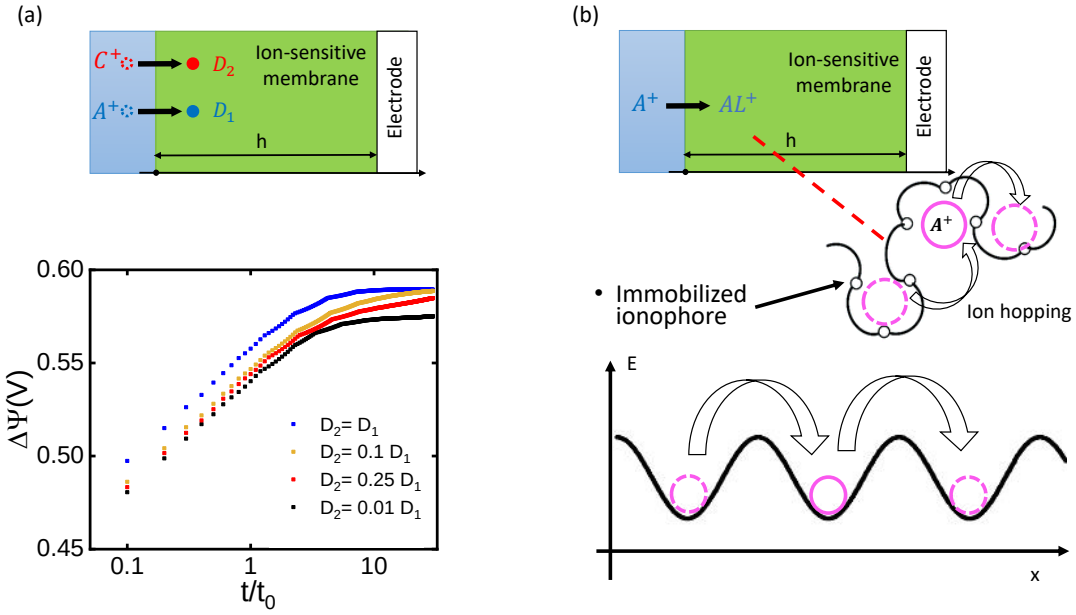

Fig. 6.1.: Selectivity of ISE (a) Numerical simulation for ion-exchange ISM case with the interference from a secondary ion. (b) ionophore-based ISM with selective reaction.

material has been carefully chosen so that the target ion has much higher diffusivity D than the other interfering ions. Therefore, the electrical potential drop across the membrane $\Delta\psi$ is primarily controlled by the target ions.

As shown in in Fig. 6.1 (a), we modify the 1-dimensional simulation setup by adding a secondary ion with a different diffusivity D_2. The coupled drift-diffusion and Poison's equation become:

$$\frac{\partial n_1(x,t)}{\partial t} = \frac{\partial}{\partial x}(\mu_1 n_1(x,t)\frac{\partial \psi(x.t)}{\partial x} + D_1\frac{\partial n_1(x,t)}{\partial x}) \tag{6.1}$$

$$\frac{\partial n_1(x,t)}{\partial t} = \frac{\partial}{\partial x}(\mu_1 n_2(x,t)\frac{\partial \psi(x.t)}{\partial x} + D_2\frac{\partial n_2(x,t)}{\partial x}) \tag{6.2}$$

$$\frac{\partial^2 \psi(x,t)}{\partial x^2} = -\frac{q\cdot(n_1(x,t)+n_1(x,t))}{\kappa\epsilon_0} \tag{6.3}$$

where the subscript index 1 represents the primary target ion while the subscript index 2 represents the secondary ion. All the boundary conditions and physic parameters for the secondary ion is set to be the same as the primary ion except the diffusivity.

As shown in Fig. 6.1 (a), we swept the diffusivity for the secondary ion D_2 from $D_2 = 0.01D_1$ to $D_2 = D_2$. We find that the transient profile of $\Delta\psi$ is bounded by the upper and lower limit of D_2: when $D_1 \gg D_2$, $\Delta\psi$ temporal profile act as if only the primary ion is penetrating through the membrane; As D_2 become larger, $\Delta\psi$ jump up quickly in the early stage due to the fast diffusing primary ion but then slowly drift because of the secondary ion; When $D_2 = D_1$, the temporal profile of $\Delta\psi$ acts as if the concentration of the target primary ion has been doubled: $n_0 = 2n_{0,1}$

Analytical solution for multiple ions We can repeat the same analytical approach used in chapter 5 to derive the analytical approximate solution for multiple ions. Let us consider a two-ion case as an illustrative example. Here, the analytical formula for the transient response is the same as Eq. 5.8 in chapter 5 except the time scaling factor depends on transport property of both primary and secondary ions:

$$V(t) = \frac{kT}{q}\ln\left(C \cdot \frac{t}{t_0}\right) \tag{6.4}$$

$$t_0 = \frac{kT}{q} \cdot \frac{\kappa\epsilon_0}{q\left(D_1 n_1 + D_2 n_2\right)} \tag{6.5}$$

The final steady-state emf expression has a similar form as Eq.5.9 in chapter 5:

$$V_{sat} = \frac{kT}{q}\ln\left(C_1\frac{(n_1+n_2)h^2}{\kappa}\right) + \mathrm{C}_2 \tag{6.6}$$

Eq. 6.6 tells us that if secondary ions can travel into the ISM, the final steady-state output is related to the sum of all the ion concentrations in the sample. But the length of time needed to reach the steady-state potential is limited by the ions with smaller membrane diffusivity. Therefore, the output signal would quickly jump to the steady-state value determined by the primary ion, but would slowly drift in due to the secondary ion afterward.

6.2.2 Ionophore-based ISM

For the ionophore-based membrane, the selectivity comes from the chemically specialized ionophore embedded in the substrate material of the membrane. The target detection ion would bind with the ionophore molecules and penetrate the ISM by hopping through various ionophore reaction sites. The selective reaction between the target ion A^+ and charge neutral ionophore L can be expressed as:

$$A^+ + L \underset{k_r}{\overset{k_f}{\rightleftharpoons}} AL^+ \tag{6.7}$$

The continuity equation for ion penetration in the membrane would be modified as:

$$\frac{\partial n_A(x,t)}{\partial t} = \frac{\partial}{\partial x}\left(\mu_A n_A(x,t)\frac{\partial \psi(x.t)}{\partial x} + D_A\frac{\partial n_A(x,t)}{\partial x}\right) - k_f \cdot n_A \cdot n_L + k_r n_{AL^+} \tag{6.8}$$

$$\frac{\partial n_{AL}(x,t)}{\partial t} = \frac{\partial}{\partial x}\left(\mu_{AL} n_{AL}(x,t)\frac{\partial \psi(x.t)}{\partial x} + D_{AL}\frac{\partial n_{AL}(x,t)}{\partial x}\right) + k_f \cdot n_A \cdot n_{\ L} - k_r n_{AL^+} \tag{6.9}$$

where k_f and k_r are the forward and reverse selectivity reaction constants. Fig. 6.1 (b) illustrate this hopping process from the energy point of view. The ionophore molecules chemically provide the local reaction energy valleys. In an ideal case, any ions on their own are not able to travel into the membrane with $D_A = 0$ and $\mu_A = 0$. The only ionophore bonded target ion in the form of AL^+ would be able to penetrate and form the dipole at the phase boundary. It is worth noticing that the reaction constants k_f and k_r, which describe the ability of the binding ability of the specialized ionophore to the target ion, play an important role in the output performance of ISM. We are going to discuss the effect of selectivity reaction constants in the section 6.6 of this chapter.

6.3 Statistical analysis and variability study of ISE experimental measurement data

Now that we have understood the physics behind ISE, let's move on to the experimental ISE measurement results. We apply a series of statistical analysis on the

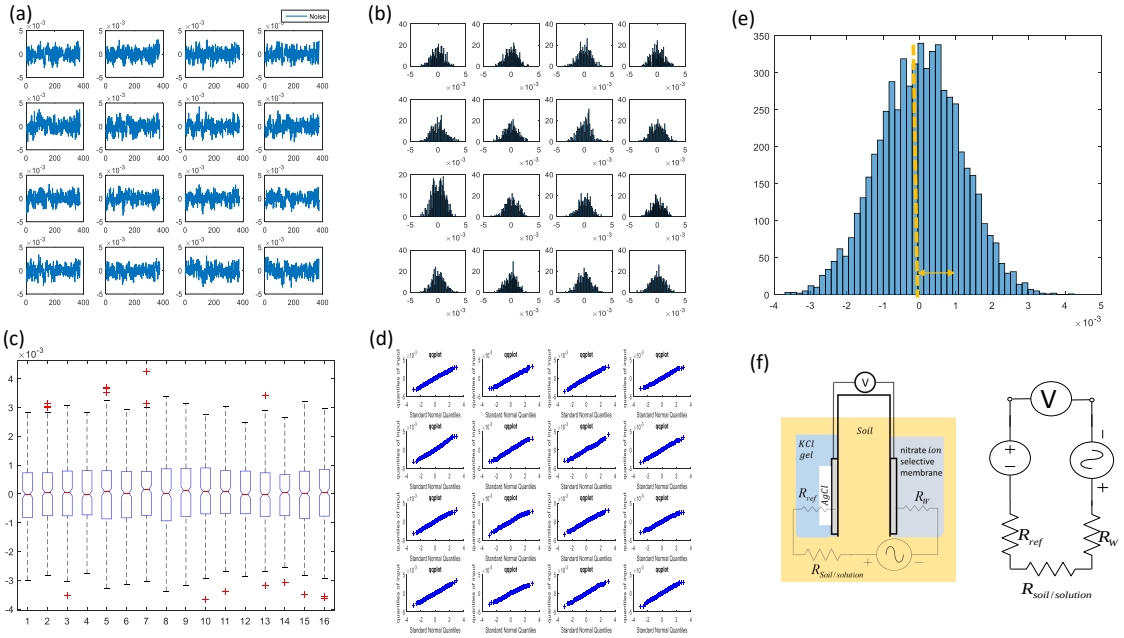

Fig. 6.2.: Statistical analysis of 16 ISE output potentiometric signal. (a) isolated noise signal (variations within each measurement). (b), (c), and (d) histogram, statistical distribution, and q-plot of the isolated noise signal. (e) Histogram of all the noise signal of the 16-measurement data in a single plot. (f) Equivalent circuit for noise analysis.

output potentiometric signal for 16 electrodes measuring in the $0.1mM$ nitrate solution. First, we pass the ISE output emf signal through a moving averaging filter with a width of 100 sampling points. Then we calculate the noise signals by subtracting the filtered signal from the original signal shown in Fig. 6.2 (a). Second, we did ANOVA test for all the 16 isolated noise signals. We calculate the F value from the ANOVA test to be 0.37 which implies that we have more than 98.6% confidence to say there are no statistically significant differences among the noise signals. We draw a histogram of the isolated noise and compare the histogram against the standard Gaussian distribution by quantile-quantile (q-q) test. We found the q-q plot for all 16 sensor electrodes well match the Gaussian distribution which implies the emf variations within each sensor electrode measurement is Johnson-Nyquist noise.

The average standard derivation (STD) of the Johnson-Nyquist noise from 16 sensor electrodes is calculated to be $\sim 1mV$. This value matches the theoretical calculation for Johnson-Nyquist noise: $V_{rms} = \sqrt{4kTR\Delta f} \sim 1.36mV$ (R calculated from the resistivity of $0.1mM$ nitrate solution). We conclude that the noise signal within each ISE sensor output is Johnson-Nyquist noise. Physically, the source of the noise signal is the thermal agitation of water molecules and nitrate ions in the testing solution.

Also, we apply ANOVA test on the original measurement signal without isolating the noise. The statistical analysis shows that the original signal fails to pass the ANOVA test with F value = 958. We conclude that there is a statistically significant difference among the 16 sensor electrodes. It comes from the sensor-to-sensor variations such as different/non-uniform ion-selective membrane thickness, bubbles forming inside the membrane, and other membrane material property variations. We are going to discuss the effect of ion-selective membrane thickness variations in detail in section 6.5.

6.4 ISM degradation

In this section, we are going to explore one of the reliability issues regarding ISE. Because of the ion-selective membrane is directly exposed to the sample solution/soil, the membrane degradation caused by moisture becomes significant. The water molecules may react with the membrane material at the interface, corrode the membrane, and cut down the thickness of the membrane h. The water molecules may also travel inside the membrane, break the membrane microstructure, and alter the diffusivity of the target ion (D) and the relative dielectric constant of the membrane (κ). At last, the water molecules may finally penetrate through the membrane, accumulate at the membrane/conducting electrode interface, form an aqueous layer, and delaminate the ion-selective membrane from the conductive electrode.

Here, we demonstrate a simple model describing the corrosion of the ion-selective membrane by moisture. The assumption is that water molecules diffuse inside the

membrane and react with the membrane material locally. We solve the following diffusion-reaction equation in a 1-Dimensional domain:

$$\frac{\partial w}{\partial t} = D\frac{\partial^2 w}{\partial y^2} - kw \tag{6.10}$$

where w stand for the moisture concentration, D is the moisture diffusivity, k is the reaction constant, and h_0 is the initial membrane thickness. By solving this partial differential equation with some boundary conditions, we found that the membrane thickness h can be expressed as a time dependent variable:

$$h\,(t) = h_0 - r_{dis} \cdot t \tag{6.11}$$

where r_{dis} is the corrosion rate of the membrane in unit of nm/day. In Fig. 6.3, we show the corrosion rate of one example membrane at different temperatures. An increase in temperature accelerates both the moisture diffusion and reaction process, thus enlarge the overall reaction rate.

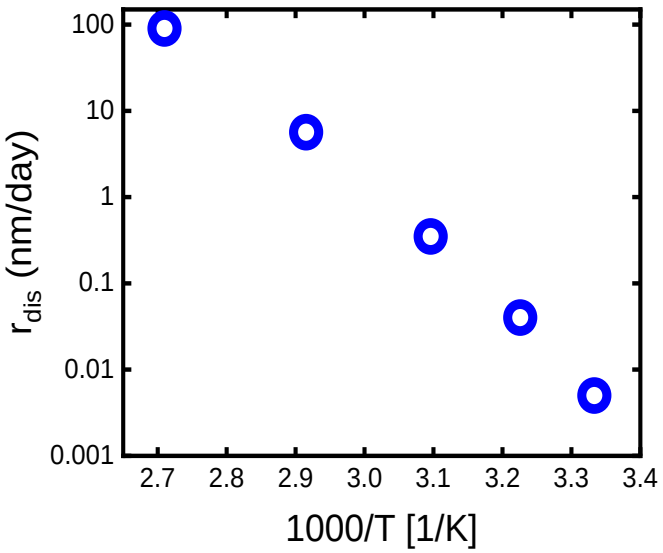

Fig. 6.3.: Ion-selective membrane corrosion rate as a function of temperature.

6.5 Effect of thickness variation and equivalent effective thickness model for non-uniform ISM

From the statistical analysis discussed in the previous section, we find that there are large variations among different sensor electrode output signals. In this section, we are going to focus on exploring one critical issue associated with the sensor-to-sensor variation: the thickness variations of ion-selective membrane. We are going to use detailed numerical simulation results to compare the effect of ISM thickness. We use experimental data to validate the thickness dependence from our model prediction. Finally, we are going to modify our model to include the effect of non-uniform ISM thickness distribution.

6.5.1 Insights of ISM thickness dependence from numerical simulation

In Fig. 6.4, we numerically compare the ion penetration process in $50\mu m$ vs. $100\mu m$ ion-selective membrane. We plot a time sequence of ion concentration profiles as well as electrical potential profiles side by side. It is clear to see that the diffusion tail of the target ion penetrates further into the ISM region for the thicker ISM case ($100\mu m$), generating a larger phase boundary potential at the sample/ISM interface. Therefore, the overall output voltage of the 100 μm ISE saturates to a higher steady-state value. From our analytical derivations in chapter 5, $V_{sat} \sim \frac{kT}{zq}\ln(h^2)$.

6.5.2 Experimental validation of thickness dependence

We validate the membrane thickness dependence of the ISE by experimental measurement results from our R2R fabricated nitrate sensor. In Fig. 6.5 (a), we plot the measured steady-state response of 3 batches of thin-film nitrate ISE with different average membrane thickness: 50μm, 70μm, and 160 μm. The concentration of the sample nitrate solution is sweeping from 10^{-4} to 0.1 M with an increment of 1 order of magnitude. The experimental data (dots) shows that an increase of the ISM thick-

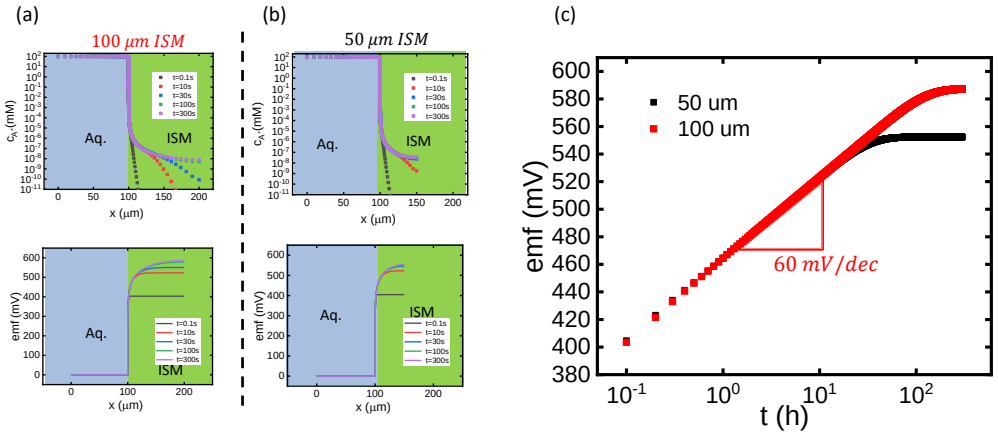

Fig. 6.4.: Detailed numerical simulation results of (a) $100\mu m$ vs (b) $50\mu m$ ISM. The top row shows the time series plot of the target ion concentration. The bottom row shows the time series plot of the potential distribution profile. (c) a comparison of the transient response of $100\mu m$ vs. $50\mu m$ ISM.

ness shifts down the value of the steady-state emf output, which is predicted by our model due to the further spread of the negatively charged nitrate ion in the ISM. To quantitatively evaluate the effect of thickness dependency, we calibrate our model to fit the experimental data. The fitting results (solid lines) captures the relative value of the experimental data with high fidelity. We plot the calibration result in Fig. 6.5 (b) in a slightly different way by switching the x-axis to ISM thickness. We can use Fig. 6.5 (b) as a guideline to map the absolute value of the ISE output voltage with any arbitrary ISE membrane thickness.

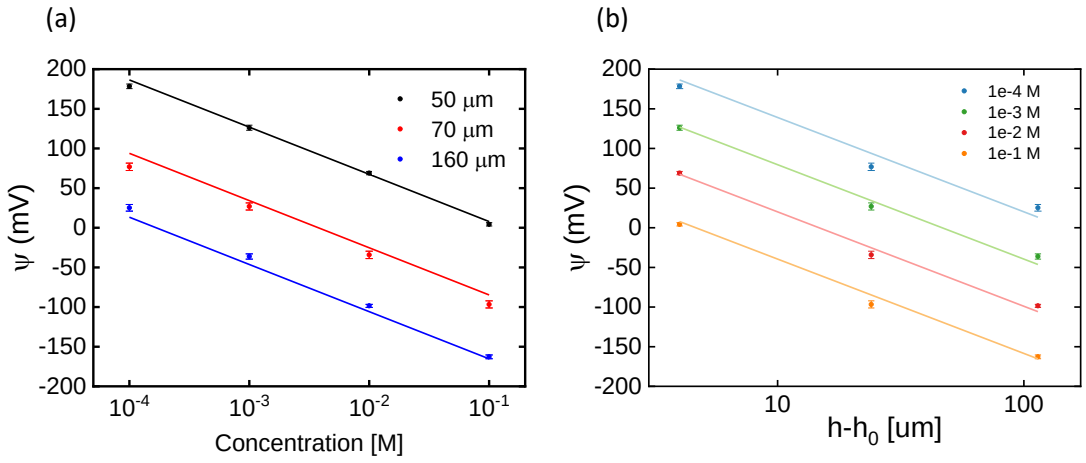

Fig. 6.5.: Experimental validation of the membrane thickness dependency. (a) ISE output emf vs. concentration for different membrane thickness. (b) ISE output emf.vs. membrane thickness for different nitrate solution concentration.

6.5.3 A model for non-uniform ISM

For any roll-to-roll printed thin-film ISE, it is impossible to guarantee a single membrane thickness across electrode active area over all the fabricated sensors. The non-uniform membrane could either come from the variations in the fabrication process or the membrane degradation discussed in the previous section. Next, we are going to explore: 1) How to modify our model to include this non-uniform membrane thickness effects? and 2) How does the membrane non-uniformity affect the steady-state response of the ISE sensor?

Fig. 6.6 shows schematic illustrations for a non-uniform membrane. Starting from the simplest case in Fig. 6.6 (a), we approximate this non-uniform membrane by dividing it into two different regions of thickness: h_1 and h_2. From our derivation in chapter 5, we know that the steady-state ISE response depends on the logarithm

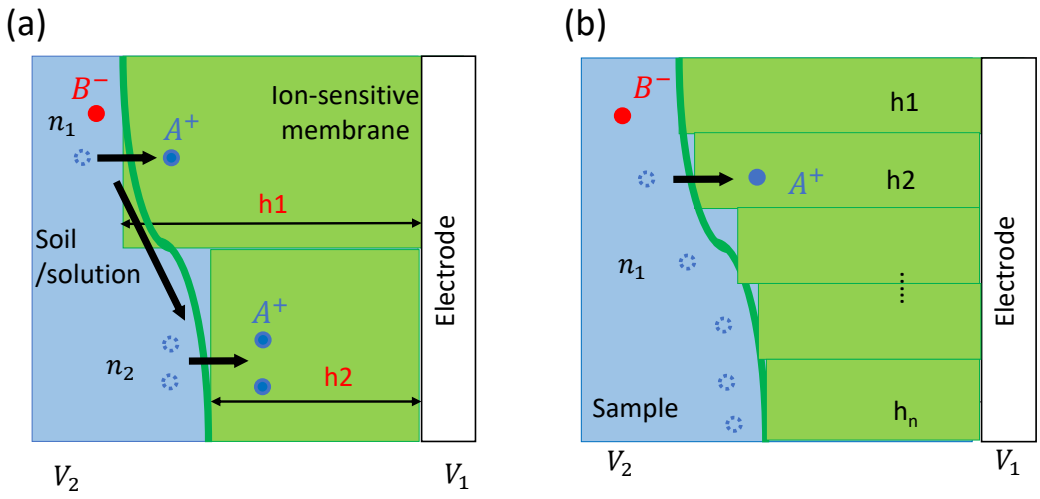

Fig. 6.6.: Schematic illustration for the model of non-uniform membrane

of h^2. Electrostatically, the total voltage drop over different thickness region should be remain the same. Therefore, the phase boundary dipoles for different membrane thickness regions should be redistributed in order to maintain the same phase boundary potential. The analytical expression for the steady-state phase boundary voltage due to two different thickness regions can be written as the following:

$$\Delta V_{sat} = \frac{kT}{q} \ln\left(\frac{n_0}{\kappa} \cdot \frac{2h_1^2 h_2^2}{h_1^2 + h_2^2}\right) + C \tag{6.12}$$

In a more general case where there is n thickness segments (h_1, h_2, ..., h_n), Eq. 6.12 can be further generalized as:

$$\Delta V_{sat} = \frac{kT}{q} \ln\left(\frac{n_0 h_{eff}^2}{\kappa}\right) + C \tag{6.13}$$

where $h_{eff}^2 = \left(n \sum_n \frac{1}{h_n^2}\right)^{-1}$ is the harmonic mean of all the distributed non-uniform membrane segments. The physical meaning of Eq. 6.12 is clear. It shows that the phase boundary potential in the steady-state is limited by the thinnest place on the

non-uniform ion-selective membrane. In other words, any non-ideal pin holes on the ISM would constrain the steady-state response of the ISE.

6.6 Super-Nernst transient response

Another non-ideal feature observed from the ISE transient response measurement is that the transient slope sometimes becomes larger than the ideal 60mV/dec value predicted by our model. We name this interesting effect as "Super-Nernst transient response". Here, we provide two possible explanations based on the assumptions that we made for our ideal model.

6.6.1 Reaction delay

As discussed in the ISE selectivity section, the chemical reaction between the target ion and the ionophore plays an important role in the ion detection process for the ionophore-based ISE. In our ideal model, we assume that the ion binding reaction is ultra-fast so that it does not limit the whole dipole forming process near the ISE phase boundary. In practice, however, this reaction process might be slow. Therefore, ionophore chemical reaction could be the rate-limiting step that determines the pattern for the transient response to follows.

Fig. 6.7 (a) and (b) quantitatively explain the effect of reaction delay by a set of numerical simulation results. In the simulation, we choose very small values for the selectivity reaction constant k_f and k_r. Fig. 6.7 (a) shows that it takes time for the target ion to react with ionophore. The bounded compound AL^+ gradually build up at boundary on the membrane side. As a result, the potentiometric response of the ISE would be delayed before output voltage jumps up to the steady-state value with transient slope $>$ 60mV/dec. The effect of reaction delay could be reduced when we increase k_f and k_r. In Fig. 6.7 (b), the transient slope converge to the 60mV/dec prediction from the ideal model with large selective reaction constant ($100k_f$ and $100k_r$).

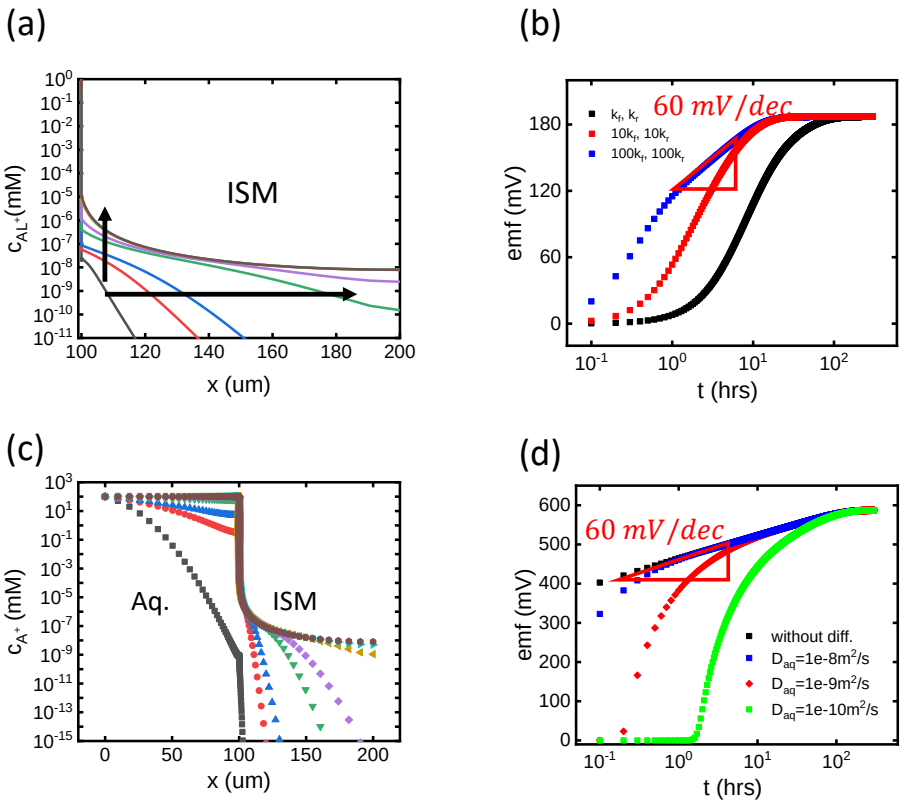

Fig. 6.7.: Numerical simulation for super-Nernst transient response. (a) and (b): reaction delay due to slower ion-ionophore reaction rate. (c) and (d): diffusion delay due to extra ion traveling time in the sample region.

6.6.2 Diffusion delay

Just like the reaction delay, the diffusion of the ions in the sample solution/soil may also account for the super-Nernst transient response. In the ideal modeling framework, we assume the ions quickly diffuse through the sample region and reach the ISE phase boundary immediately. In the numerical simulation, we choose a large value of ion diffusivity in the sample solution (in the order of $10^{-8}\ m^2/s$). For a non-ideal case such as detecting nitrate ion in a soil sample, the diffusivity of the target ion in the soil sample might be orders of magnitude smaller than the solution.

As a result, it may take much time for the ions to travel through the soil sample before reaching the ISE sensor electrode.

In Fig. 6.7 (c), we simulate an extreme case with a diffusivity in the sample region $D_{aq} = 10^{-10}\ m^2/s$. Initially, the concentration of the target ion A^+ in the 100 μm sample region is zero. In the time sequence plot, A^+ penetrate and accumulate in the sample region before travel into the membrane region. Fig. 6.7 (d) shows that as the ion diffusivity in the sample increases 2 orders of magnitudes from $10^{-10}m^2/s$ to $10^{-8}m^2/s$, the transient response unites with the case (black line) without diffusion delay.

For both diffusion delay and reaction delay, the ISE output finally reaches the same steady-state voltage. Therefore, those two non-ideal phenomena can be ignored for the steady-state in-lab measurements. But for real-time in-vivo field applications where the transient response is significant, the effect of diffusion delay and reaction delay needs to be considered carefully.

6.7 The strategies to improve the ISE sensor performance

6.7.1 The strategy to reduce sensor-to-sensor variations

Eliminate the thickness variation from the correlation between image analysis and measurement variability

In the ISM thickness variation section, we have introduced an equivalent thickness analytical model to account for the non-uniformity of the membrane coating. Our model shows that different equivalent membrane thickness as well as other design parameters of membrane material properties (dielectric constant κ, ion diffusivity D) would shift the entire output voltage response in the vertical direction. In the real ISE sensor characterization experiments, however, it requires complicated lab instruments (e.g. white light interferometry) to measure an accurate ISM thickness distribution over the entire active area of the working electrode. It is even more

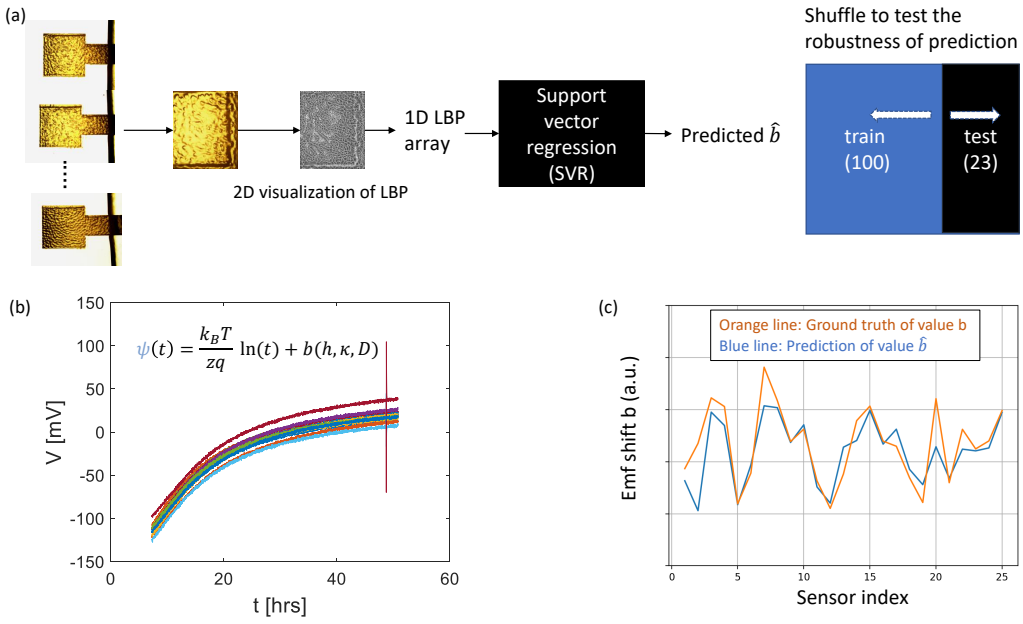

Fig. 6.8.: Scalable image processing and machine learning method to predict the output voltage shift caused by sensor-to-sensor membrane thickness variations.

difficult to measure the variations in dielectric constant and ion diffusivities of the membrane. The time-consuming process makes it impossible to calibrate the ISM thickness across all the scalable manufactured ISE sensor electrodes to reduce the variations in the sensor-to-sensor output signal.

Here, we introduce a simple but scalable image processing method to predict the output voltage shift caused by sensor-to-sensor membrane variations. As shown in Fig. 6.8 (a), we take the pictures of a batch of working electrodes of a roll-to-roll printed ISE sensors (for the demonstration:123 sensors in total). We apply an edge detection image processing technique [136] to isolate the working electrode active area. Different texture information shown in the image represent the thickness variations and dielectric constant variations of the ISM coating. According to our physics-based model, the membrane thickness as well as other parameters of membrane material properties (dielectric constant κ, ion diffusivity D) determines the absolute value of the output voltage shift b:

$$\psi(t) = \frac{k_B T}{zq}\, ln(t) + b(h, \kappa, D) \tag{6.14}$$

The image of the active area of the sensor is highly correlated to the shift of each measurement curve shown in Fig. 6.8 (b). The goal is to quantify the correlation and use it to predict the value of voltage shift b from the picture of the sensor electrode.

We apply traditional machine learning approach, including Local Binary Pattern (LBP) [137] (an illumination-invariant texturing descriptor) and non-linear regression model, to predict voltage shift b based on images of the ISE sensor active areas. Before the training process, we use LBP to extract texturing representation as 1D arrays from each image. Then we apply the 1D array as our input to the non-linear regression model. We use support vector regression (SVR) [138] to realize the regression model.

Our dataset includes the images of 123 sensors with the corresponding voltage shift b. In our implementation, we randomly select 23 sensors to be the training dataset and 100 sensors to be the testing dataset. To prevent the problem of over-fitting, we shuffle the training and testing dataset within the whole dataset and repeat the the procedure 10 times. Comparing to the measurement ground truth (orange line) shown in Fig. 6.8 (c), the predicted average voltage shift $\hat{b}$ (blue line) achieves a prediction error of : $\epsilon_{prediction} = \frac{\sum \frac{|\hat{b}-b|}{|b|}}{N} < 11\%$.

This physics-based image processing machine learning method can be easily applied to calibrate and predict the sensor performance for large scale manufacturing processes where sensor-to-sensor fabrication variation is unavoidable.

6.7.2 The strategy to reduce ISE response time

Another big issue that prevents the solid-contact ISE sensor from its IoT applications is associated with the response time. As mentioned in Chapter 5, the solid-contact ISE sensors require several hours of preconditioning time in the target ion solution with known concentration to be stabilized before they are ready to take measurements. In this section, we are going to use our modeling framework to

make a comparison between the fast response classical liquid-contact ISE and the solid-contact ISE. We are going to introduce a new solid-contact ISE design that borrows ideas from the conventional-liquid contact design that largely reduces the preconditioning response time.

A comparison between liquid-contact and solid-contact ISE: one-sided ion penetration vs. two-side ion penetration

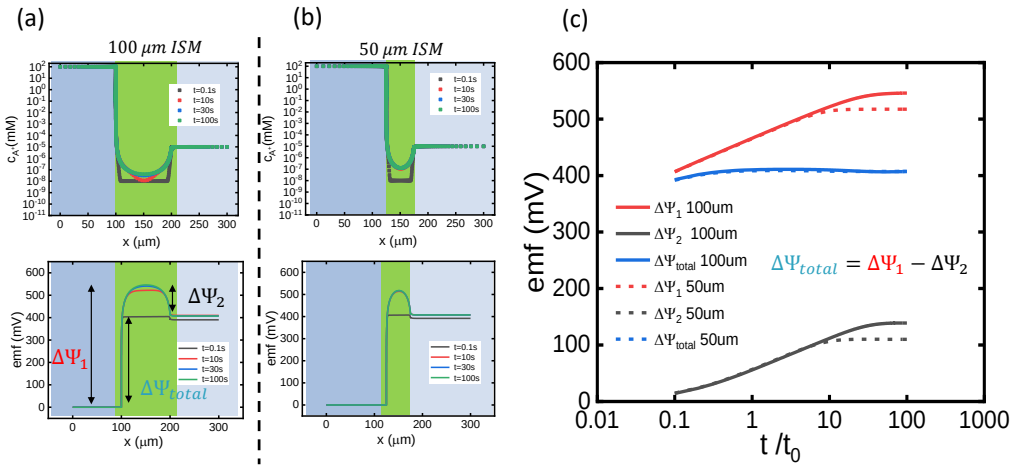

Fig. 6.9.: Detailed numerical simulation for liquid-contact ISE. (a) and (b): a comparison between $100\mu m$ vs. $50\mu m$ ISM. (c): the total output transient response from the two-phase boundary potential.

To describe the behavior of a conventional liquid contact ISE, we modified our two-region numerical simulation set up for the solid-contact ISE by adding the third inner-filling solution region between the ISM and the metal electrode. The inner filling solution region contains the target ion A^+ solution with a constant concentration of 0.1mM. As shown in Fig. 6.9, we compare the time sequence profile of ion con-

centration and potential distribution for 50μm vs. 100μm ISM. The target ions from both the sample solution and the inner filling solution could penetrate the ISM from both sides, forming two phase boundary potentials $\Delta\psi_1$ and $\Delta\psi_2$ face to face. The total potential drop across the ISM membrane region would be the difference between the two-phase boundary potentials: $\psi_{\text{total}} = \psi_1 - \psi_2$. In Fig. 6.9 (c), we plot ψ_1, ψ_2, and ψ_{total} as a function of time in a semi-log-x plot. Although the individual phase boundary potential (ψ_1 or ψ_2, black and red curves) follows the 60mV/dec transient function in time, the total voltage drop ψ_{total} become stabilized quickly. Another interesting observation is that the blue dashed line (50μm ISM) nearly align with the blue solid line (100μm ISM), indicating ψ_{total} is less sensitive to ISM thickness.

From the numerical simulation for liquid contact ISE, we conclude that the inner-filling solution helps reduce the response time by forming another dipole at the ISM-inner filling solution interface. Also, the thickness of the ISM does not have a big impact on the potentiometric response of liquid contact ISE.

A new solid-contact ISE design with graphene as an inner conducting layer

As mentioned in the previous chapter, the purpose of designing all solid-contact ISE is to avoid the drawbacks of an inner-filling solution for IoT applications. From our experimental measurement data and the theoretical analysis, however, we find that the response time and sensor-to-sensor variations become two main challenges. To overcome the two challenges, we propose a new solid-contact ISE design by adding a graphene layer between the ISM and metal electrode. This design takes advantage of the liquid-contact ISE with graphene serving as the inner conducting layer. An additional electron-hole pair form a dipole at the ISM-graphene interface, compensating the large voltage jump in the pre-conditioning phase. As shown in Fig. 6.10, the transient potentiometric response for the new design reaches its steady-state value much faster. Also, the impact of the ISM thickness has been reduced dramatically. As a result, we observe less sensor-to-sensor variations of the output voltage.

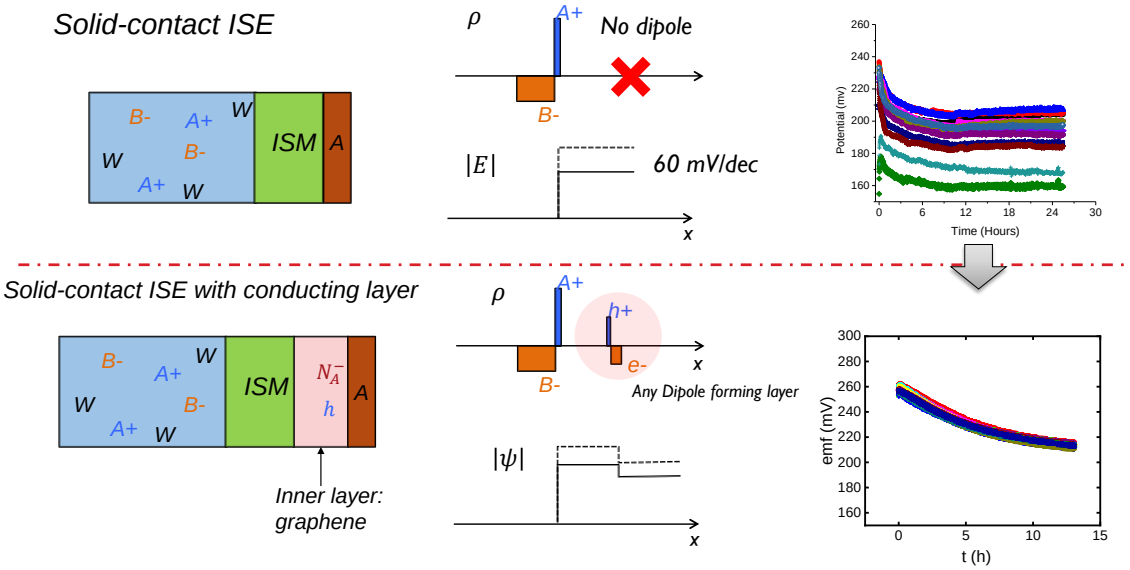

Fig. 6.10.: Schematic illustration of a new solid-contact ISE design with graphene as an inner conducting layer.

6.8 Conclusions

In this chapter, we have discussed the challenges for ISE IoT applications and the corresponding strategies that overcome the problems based on our physics-based modeling framework. The Poisson coupled ion drift-diffusion transport process is universal. Our physics-based model is transferable to other designs of electrical, mechanical, and chemical applications such as reducing ion-induced degradation for photo-voltaic systems, understanding ion migration from the metal contact pad in the high-power electronics.

7. STABILITY OF MOSFET-BASED ELECTRONIC COMPONENTS IN WEARABLE AND IMPLANTABLE SYSTEMS

7.1 Motivation

Wearable and implantable electronic (WIE) devices, such as a digital wristband, smart watch, and implantable cardioverter defibrillator, etc. have found widespread usage in healthcare and fitness applications [139]. The next generation wearable electronic devices (ultra-thin film electronics [140, 141], for instance) must be lightweight and have smaller form factor. Numerous groups have experimentally demonstrated functional prototypes. For example, Kim *et al.* have introduced "skin-like" membrane-based approach that integrates electrodes, electronics, sensors, power supply and communication components [115]. Kaltenbrunner *et al.* fabricated ultrathin active-matrix array with resistive tactile sensors [142]. Gao *et al.* have developed wearable sensor array platform for multiplexed in situ perspiration analysis [99]. Lee *et al.* have introduced a 'patch-like' electrochemical device for diabetes monitoring and therapy [24].

Long-term electromechanical stability and reliability are critical challenges for the next generation WIE systems. Comparing to the electronic components in traditional devices such as a mobile phone, the electronic components in WIE systems need to operate in an electrochemical fluid, such as sweat, saliva, and blood [143, 144]. Temperature, pH, moisture, ion concentration, etc. in the electrochemical fluid offer a non-traditional operating environment for traditional electronics, hence reliability issues of those electronic components are essential. For some devices such as bio-

[0]The content of this chapter is primarily taken from a published paper: Jin, X., Jiang, C., Song, E., Fang, H., Rogers, J. A. ,and Alam, M. A. "Stability of MOSFET-based electronic components in wearable and implantable systems. " *IEEE Transactions on Electron Devices*, 2017 64(8), 3443-3451

implantable sensors in cardiology applications, the electronic system should have a long-term stability. For other applications such as transient electronics for brain monitoring, a precise predictable degradation lifetime is of great interest [145–147]. Due to the small physical dimension, light weight, mechanical flexibility [148] and other requirements, proper design of packaging encapsulant without compromising electronic functionalities becomes an important design challenge for these electronic components.

Among various degradation mechanisms, charged ions penetrating into the encapsulation layer of wearable electronic devices directly disturb the electric field and lead to functional-failure the electronic components. The family of MOSFE-based electronic device [149] is one of the most widely used electronic components in WIE system, because they allow highly complex integration of multiple sensing and signal processing functions. Unfortunately, the performance and electrostatic integrity of MOSFETs is very sensitive to charged ions. This chapter focuses on the performance degradation of MOSFET-based electronic components, more specifically, the threshold voltage shift: ΔV_{th}, of WIE systems.

The WIE components can be divided into four groups, as shown in Fig. 7.1:

1. *Chemical biosensors* such as classical Ion-Sensitive Field-Effect Tansistor (ISFET) potentiometric sensor [150, 151]. They consist of an ion selective membrane layer on top of an insulated gate FET. The gate insulator plays an important role in protecting the channel of the ISFET from bio-fluid. Nevertheless, the charged ions penetrating into the gate insulation layer will eventually degrade the ISFET electronic performance.

2. *MEMS-based physical biosensors* [152–154] feature a microstructured dielectric gate oxide. The external pressure deforms the Micro-Electro-Mechanical Systems (MEMS) gate oxide, changes the gate capacitance, and modulates the drain current of the underlying MOSFET. Regarding its reliability, the charged

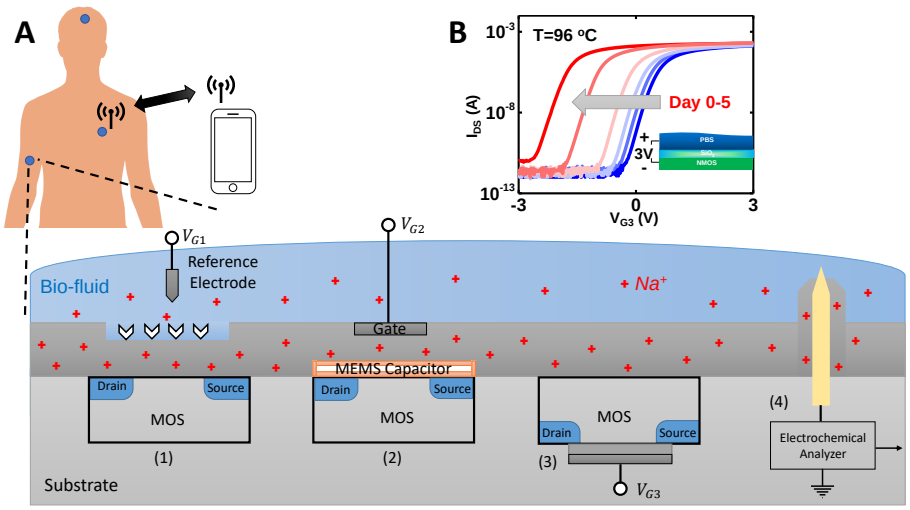

Fig. 7.1.: A. Schematic illustration of four categories of electronic components in WIE systems. 1) Chemical biosensor. 2) MEMS-based physical biosensor. 3) Implantable MOSFET for signal processing. 4) Amperometric biosensor electrode. B. Measured $I_{ds}-V_{gs}$ curves for signal processing MOSFET from accelerated salt soaking experiments at the end of 0-5 days.

ions from the human body can penetrate into the gate oxide layer and destabilize the MOSFET $I_{ds} - V_G$ response.

3. *Implantable MOSFET for signal processing* [155]. Unlike chemical or MEMS sensors, the signal processing circuitry does not involve sensing the surrounding, and may thus be entirely isolated. However, due to the ultra-thin encapsulation in flexible WIE systems, the charged ions may nonetheless penetrate through in the back encapsulation layer and shift the threshold voltage of the MOSFET.

4. *Amperometric biosensor electrode* for implantable applications. For these sensors, only the tip of the electrode must be exposed to the desired location, while the rest of the electrode must be isolated from the surrounding environment. As charged ions penetrate the encapsulant, the electrode inactive area

could generate large parasitic amperometric currently, and rapidly degrade the signal-to-noise ratio of these sensors.

In this chapter, we concentrate on MOSFET-based electronic device degradation mechanisms, cases (1), (2) and (3). To illustrate the importance of the stability/reliability of the devices, we conduct accelerated soaking experiments at $96°C$ in standard phosphate-buffered saline solution (PBS), consisting of Na_2HPO_4 and $NaCl$ dissolved in water. We apply an external voltage $V_0 = 3V$ across the test structure, with a back-gated NMOS device packaged inside (case 3). Details of the soaking test have been reported in [156,157]. Fig. 7.1 B shows the measured $I_{ds} - V_{gs}$ curves of the NMOS at the end of 0-5 days. There are two key observations: 1) the NMOS threshold voltage becomes more negative over time, consistent with the hypothesis that positively charged Na^+ is gradually penetrating the encapsulation layer and distorting the electrostatics of the transistor channel, and 2) the absolute value of ΔV_{th} increases non-linearly and accelerates over time.

To explain the experimental observations, this chapter is divided into the following sections. In section 7.2, we offer both a numerical framework and an analytical model for Na^+ transport through the encapsulation layer. In section 7.3, we provide two basic MOSFET degradation models(front gate and back gate cases) including the influence from the penetrated Na^+. The coupled model can be used to predict the overall device lifetime for arbitrary WIE systems. The measurement data from accelerated reliability experiments confirm our model to be precise and scalale. In section 7.4, the model is used to develop design guidelines for encapsulation layers for WIE systems. Finally, we note that the problem of ion penetration is general, thus our model will be useful for design of broad range of electronic, mechanical and chemical systems such as eliminating undesiable Potential Induced Degradation (PID) in photovoltaic(PV) systems [158], contact-pad induced ion drift in high power electronics [159], and so on.

7.2 Model System Part A: ion penetration

In this section, we will numerically simulate Na^+ penetration process through the encapsulation layer from the PBS solution. From the results of the numerical framework, we will then derive analytical models and scaling principles to describe this physical mechanism and offer design guidelines.

7.2.1 Numerical Framework

The transport of Na^+ through the ion barrier layer can be described by the well-known space-charge-limited process [160]. We solve the corresponding transport equations (Eq. 7.1 and Eq. 7.2 below) using COMSOL Multiphysics simulator. Fig 7.2 A shows the schematic illustration of the structure where $x = 0$ and $x = h$ correspond to the PBS/ion barrier and ion barrier/Si interface. We determine the density of Na^+ (n) by solving the coupled Poisson's equation and continuity equation:

$$\frac{\partial^2 \psi(x.t)}{\partial x^2} = -\frac{q \cdot n}{\kappa \epsilon_0} \tag{7.1}$$

$$\frac{\partial n}{\partial t} = -\frac{\partial}{\partial x}(\mu\ n \frac{\partial \psi(x.t)}{\partial x} - D\frac{\partial n}{\partial x}) \tag{7.2}$$

where $\psi(x.t)$ is the electrical potential, κ is the relative dielectric permittivity, ϵ_0 is the vacuum permittivity constant, and μ and D are the mobility and diffusivity of Na^+ in the encapsulation layer material (thermal SiO_2 for this illustrative example). Einstein's relation: $\frac{D}{\mu} = \frac{kT}{q}$ connects these quantities. The analysis makes the following assumptions, none of which should have significant effect on the key conclusions.

1. The area of the ion barrier in the y-z direction is much larger than its thickness in the x direction. Therefore a simplified 1-D simulation is appropriate.

2. Na^+ incorporation in the oxide is fast enough so that it does not limit the total drift-diffusion process. This allows us to define a constant Na^+ density (n_0) at the PBS/encapsulant interface. This interfacial concentration equals the

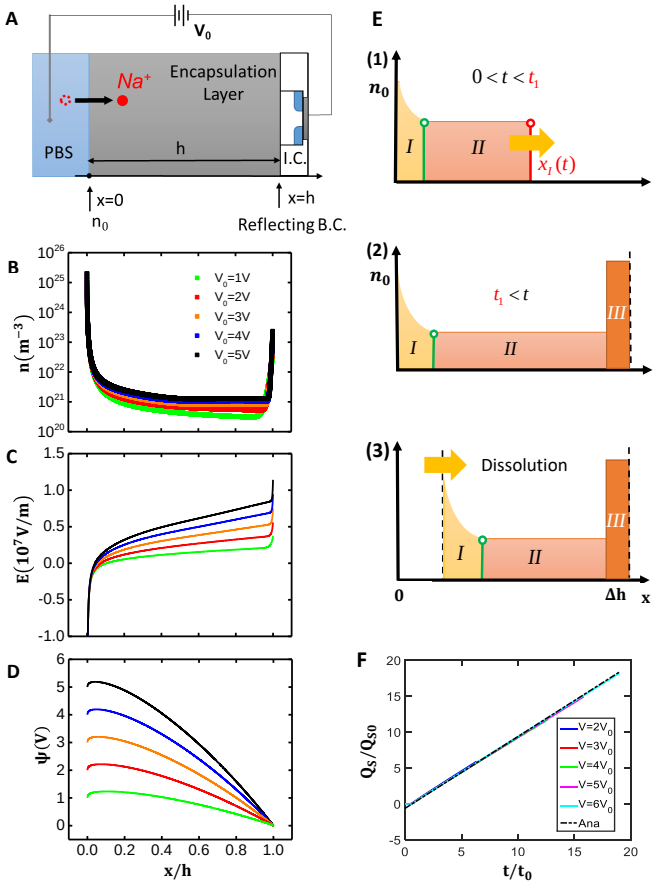

Fig. 7.2.: Numerical framework of space-charge-limited Na^+ penetration process. A. Schematic illustration of sodium ion penetration in 1-D single layer ion barrier domain with external applied voltage V_0. B-D. Na^+ density, electrical field and potential distribution within $h = 1000nm$ thermal SiO_2 layer at the end of $t = t_0 = (kT \cdot h^2)/DqV$ simulation. Potential bias V_0 is swept from 1 to 5 V with an increment of 1 V. E. Schematic illustration of time dependent Na^+ concentration profile. Region I: accumulated Na^+ near the PBS/encapsulant interface. Region II: approximate constant low Na^+ concentration middle region. Region III: accumulated Na^+ region near the encapsulant/Si interface. F. Normalized surface density of Na^+ near the encapsulant/Si interface as a function of normalized time under different external biases.

solubility limit of Na^+ inside the encapsulant (*i.e.*, 33 $mmol/L$ ($2 \times 10^{25} m^{-3}$) in thermal SiO_2) [161].

3. The physics of moisture diffusion is not included and any coupled transport effect is ignored. Therefore, the Na^+diffusion coefficient D is uniform across the encapsulant.

4. D of Na^+inside thermal SiO_2 is much smaller than that of crystalline silicon it protects [162–164]. Therefore, a reflective boundary condition defines the thermal SiO_2/Si interface.

5. The externally applied voltage V_0 across the whole structure drops primarily across the encapsulation layer, and the capacitive drop over the ultrathin double-layer screening ions [165] may be ignored.

Fig. 7.2 B shows the spatially distributed Na^+ density profile at the end of $t = t_0$ where t_0 is defined as the drift dominated transport time:

$$t_0 = \frac{h}{\mu E} = \frac{kTh^2}{DqV_0} \tag{7.3}$$

where h is the thickness of the encapsulation layer, E is the electric field, k is the Boltzmann constant, and T is the temperature. We swept the electrostatic potential V_0 from 1V to 5V with an increment of 1V. The Na^+ density decreases significantly near x=0 and accumulates at $x = h$. According to Poisson's equation (Eq. 7.1), the accumulated Na^+ near the two boundaries contribute to the significant jump of the electric field, as shown in Fig. 7.2 C.

Fig. 7.2 D shows the potential distribution across the encapsulant. Interestingly, a self-induced potential barrier (with peak value higher than V_0) occurs inside the encapsulation layer. The additional accumulated Na^+ charges lead to a negative electric field near the interface of PBS solution and the encapsulant layer. From a transient prospective, this potential barrier gradually builds up and slows down the

ion transport until Na^+ influx from the PBS solution is balanced by the negative interfacial electric field that is trying to push the ions back into the solution. In fact, we can model this internal potential barrier as an ion density dependent virtual voltage source [166]. As V_0 increases, the location of this virtual voltage source (x_0 where the electrical field reaches zero) consistently moves towards the left boundary. Moreover, the normalized potential barrier $v_r \equiv (V_{peak} - V_0)/V_0$ decreases with increasing V_0.

This virtual voltage source model explains the trend of the Na^+ density profiles under different external bias, shown in Fig. 7.2 B. If the ion drift is the dominate transport mechanism, all the five density profiles should have scaled to a universal curve at $t = t_0$. However, Fig. 7.2 B shows that there is an excess Na^+ built-up inside the encapsulation layer with increasing V_0. The location of the virtual source shifts to the left and the relative magnitude of the virtual voltage source decreases, implying the relative ineffectiveness of the potential barrier in preventing Na^+ penetration into the encapsulant.

7.2.2 Analytical Model and Scaling Principles

Intrigued by the essential simplicity of the density profiles obtained numerically, in this section we derive the time-dependent density distribution for a single encapsulation layer analytically. We solve the continuity equation and Poisson's equation self-consistently. An exact analytical solution is impossible, but a few simple, numerically validated assumptions allow insightful approximate solution of this complex space-charge-limited ion transport problem.

Fig. 7.2 E shows the schematic illustration of Na^+profile before the critical time $t_1$at which Na^+ front flow line reaches the right boundary. This critical transition time t_1 is calculated from [160] as:

$$t_1 = 2\left(1 - e^{-\frac{1}{2}}\right) \cdot t_0 = 0.787 t_0 \tag{7.4}$$

The position of the front $x_I(t)$ is given by:

$$x_I(t) = -2 \cdot ln(1 - \frac{1}{2}t/t_0) \cdot h \tag{7.5}$$

In region II, the total current flux ($J = q\mu nE + \kappa\epsilon_0 \frac{\partial E}{\partial t}$, the sum of conduction and displacement currents) is independent of position (x), so that $\frac{\partial J}{\partial x} = 0$. By taking the partial derivatives with respect to x for both conduction current and displacement current,following the carrier flow line: $\frac{dx(t)}{dt} = \mu E$ suggested by [160], and canceling and rearranging terms, the density of Na^+ (before t_1) can be shown to follow a simple relationship:

$$\frac{dn}{dt} = -\frac{\mu q}{\kappa\epsilon_0} \cdot n^2 \tag{7.6}$$

By integrating both side of Eq. 7.6, Na^+ density in region II can be expressed as a time dependent variable as:

$$n_{II}(t) = \frac{n_0}{1 + \frac{\mu q}{\kappa\epsilon_0} n_0 \cdot t} \tag{7.7}$$

In region I, however, there's no exact analytical solution for $n_I(t)$. Fortunately, the numerical simulation in Fig. 7.2 B shows that the width of region I is negligibly small and the Na^+ density drops nearly 4 order of magnitude within this region. Therefore, the delta-function shaped contribution of Na^+ from this region to the overall MOSFET device performance can be approximated by a constant. We will discuss this point further in section 7.3. a) when we calculate the threshold voltage shift of a transistor.

After the critical transition time t_1, $x_I(t)$ reach the encapsulation layer/Si boundary. Na^+ ions begin to pile up and form region III, as shown in Fig. 7.2 E. During this time interval, the Na^+ influx gradually reach a steady-state value as first derived by Mott and Gurney [167]:

$$J = \frac{9}{8}\kappa\epsilon_0\mu\frac{V_0^2}{h^3} \tag{7.8}$$

Therefore, we can approximate the surface charge density of Na^+ in region III from the steady-state flux as:

$$Q_s = J \cdot (t - t_1) = \frac{9}{8} q\kappa\epsilon_0\mu \frac{V_0^2}{h^3} \cdot (t - t_1) \tag{7.9}$$

Fig. 7.2 F shows the normalized surface charge density in region III Q_s/Q_0 ($Q_0 = \frac{9}{8}\kappa\epsilon_0\mu\frac{V_0^2}{h^3}t_0$) as a function of normalized time t/t_0 for both numerical simulation result with different V_0 and analytical result from Eq. 7.9. After $t > t_1$, all the numerical results as well as the analytical solutions can be scaled to the same universal curve. This universality verifies the assumptions and approximations in our analytical derivation. Also, Q_S scales linearly with time, as in Eq. 7.9. The upper-limit for Eq. 7.9 is defined by the requirement that Na^+ density $n = \frac{Q_s}{q \cdot \Delta h}$ cannot exceed the dissolution limit for the chosen encapsulant material.

The encapsulation layer sometimes dissolves in the harsh salty environment. To account for this effective thinning of the encapsulant through hydrolysis, we make the encapsulant thickness h (Fig. 7.2 E (3)) a time-dependent variable, namely,

$$h\,(t) = h_0 - r_{dis} \cdot t \tag{7.10}$$

where $\mathrm{r_{dis}}$ is the encapsulation layer dissolution rate (in units of nm/day) measured from the soaking experiments conducted at different temperatures. As we will see in section 7.3 the physical thinning of the encapsulation layer is essential to understand the nonlinear voltage shift reported in the experiments. Now that we have developed both numerical and analytical models describing time-dependent Na^+ density profile, in the next section, we are going to explore the impact of the charged ions on the overall performance of the MOSFET-based devices.

7.3 Model System Part B: MOSFET-based Electronic Component Performance Degradation

In this section, we will establish how ΔV_{th} of a MOSFET is affected by the amount of charged ion distribution within the encapsulant. We will focus on two types of MOSFET-based components: a) Front-gated MOSFET for biosensor applications (Type 1 and Type 2 devices described in section 7.1, and b) Back-gate MOSFET for signal processing (Type 3 device in section 7.1). Eventually, we will use the ΔV_{th} model to design encapsulant layers for specific WIE systems.

7.3.1 WIE System containing front-gated MOSFET

Similar to the effect of mobile charges in the traditional MOSFET device gate oxide [168], the charged Na^+ in the encapsulation layer will shift the effective gate voltage seen by the transistor. The failure threshold ΔV_{th} can be expressed as a function of spatial distributed Na^+ density, as follows:

$$\Delta V_{th}(t) = \frac{q}{C_0}[\frac{1}{h}\int_0^h x \cdot n(x,t)dx] \tag{7.11}$$

where C_0 is the initial gate capacitance, h is the thickness of the coating layer. The 1-D spatial coordinate is defined as $x = 0$ at the gate/oxide interface shown in Fig. 7.3 A.

As discussed in section 7.2, we derive the time dependent analytical expression for Na^+density profile $n(x,t)$ in region II (Eq. 7.7) and region III (Eq. 7.9). Inserting $n(x,t)$ in Eq. 7.11, we find:

$$\Delta V_{th} = \frac{\kappa\epsilon_0 V_0}{2h \cdot C_0} \cdot \left[-2ln\left(1 - \frac{t/t_0}{2}\right)\right]^2 \cdot n_{II}(t) + V_{th,I} \quad (t < t_1) \tag{7.12}$$

$$\Delta V_{th} = \frac{\kappa\epsilon_0 V_0}{h \cdot C_0} \cdot \left[\frac{n_{II}(t_1)}{2} + \frac{9}{8}\left(\frac{t-t_1}{t_0}\right)\left(1 - \frac{kT}{2qV_0}\right)\right] + V_{th,I} \ (t > t_1) \tag{7.13}$$

where $V_{th,I}$ is the threshold voltage shift contributed by in region I, see Fig. 7.2. Recall that we can treat $n_I(t)$ as a time-independent delta-function (once t>t_1), therefore

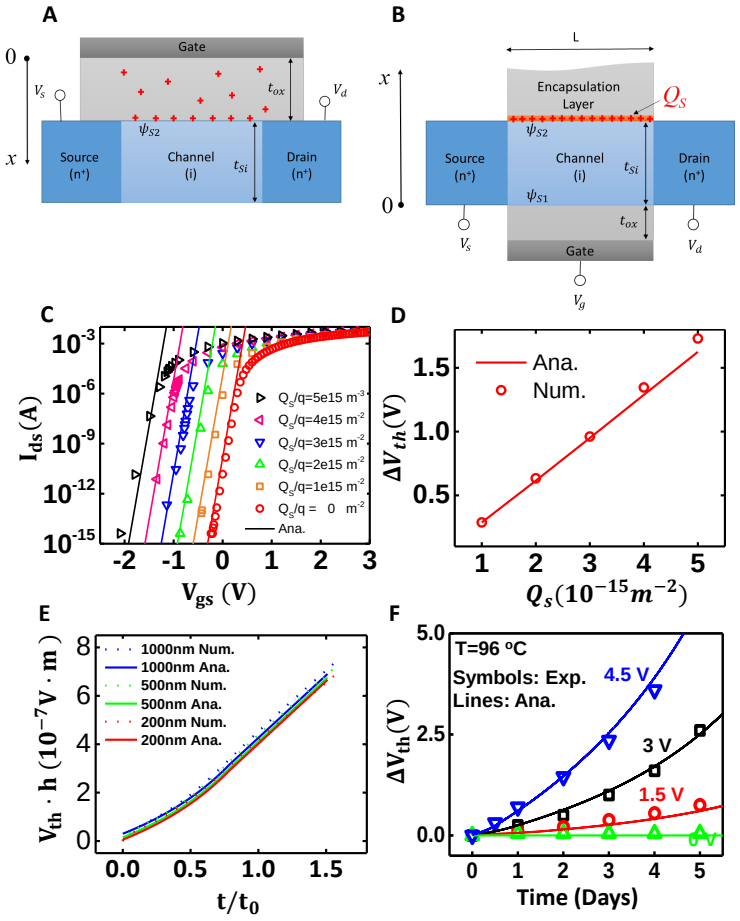

Fig. 7.3.: Implantable electronic device performance degradation. A. Schematic illustration of front gate ISFET potentiometric sensor. B. Schematic illustration of back gate signal processing MOSFET. C. Back-gate MOSFET Id-Vg curve with various back-gate charge surface density Q_s. Numerical(symbols) simulation vs. analytical (lines) result. D. Back-gate MOSFET $\Delta V_t h$ as a function of Q_S E. Front gate MOSFET implantable device ΔV_t has a function of normalized time for different ion barrier thickness. Numerical (dashed lines) vs. analytical (solid lines) results. F. Back-gate MOSFET implantable device threshold voltage shift within five days soaking test under different V_0. Experimental (symbols) vs. analytical (lines) results.

the corresponding V_{th} shift is also a time-independent constant. Our numerical simulations conclusively prove that this assumption is justified for the range of thicknesses typical of WIE systems. Fig. 7.3 E shows the product of threshold voltage shift and encapsulation layer thickness ($\Delta V_t \cdot h$) as a function of normalized time (t/t_0). Remarkably, all 6 curves scales to form a universal curve with two characteristic phases. The first phase correspond to $t/t_0 < t_1/t_0$ when the Na^+ front is yet to reach the other boundary of the ion barrier. Both numerical and analytical results (Eq. 7.12) show a non-linear ΔV_{th} increase. During the second phase where $t/t_0 > t_1/t_0$, ΔV_{th} is contributed by the accumulated surface charges in region III (at the encapsulant/Si interface.) Eq. 7.13 shows ΔV_{th} increases approximately linearly with time. This linear relationship is also confirmed by the COMSOL numerical simulation.

Similar to the concept of equivalent oxide thickness (EOT) for classical MOSFET where different gate oxide materials share the same gate capacitance, we can also define an equivalent ion barrier effective thickness (EIBT) for various encapsulation layer materials. Two materials with the same EIBT will be equally effective in protecting the MOSFET from ion-induced instability in a fluidic environment. From Eq. 7.13, we can derive an approximate compact expression at $t > t_1$ as:

$$h \propto \sqrt[3]{D \cdot \kappa} \tag{7.14}$$

The appearance of dielectric constant and mobility in Eq. 7.14 (as well as the cube-root dependence) reflects the space-charge-limited ion transport that defines the functional lifetime of MOSFETs. We will use this EIBT concept in section 7.4 to compare the performance of two candidate encapsulation layer materials.

7.3.2 Back-gated MOSFET for Signal Processing.

Eq. 7.9 defines the dependence of the surface charge density Q_s on V_0 and the PBS soak time. In this subsection, we will relate Q_S to ΔV_{th} for a back-gated MOSFET within a WIE system.

Fig. 7.3 B shows the 2D cross section of embedded NMOS device underneath the ion protection encapsulation layer. For simplicity, we will focus on long channel transistors. Since the channel length ($L = 20\mu m$) is much larger than the Si substrate thickness ($t_{Si} = 100\ nm$), we can simply solve for V_{th} in 1D as indicated in the x direction. The assumption is easily removed, if needed [169].

We solve the simplified Poisson's equation in intrinsic Si channel MOSFET:

$$\frac{\partial^2\psi(x)}{\partial x^2} = \frac{q}{\kappa_{Si}\epsilon_0} \cdot n_i \cdot exp[\frac{q \cdot \psi(x)}{kT}] \tag{7.15}$$

where $\psi(x)$ is the local potential at position x, n_i is the electron density in intrinsic Si. By integrating both side with x and applying the corresponding boundary conditions, the overall charge density inside the channel Q_{total} and the potential at the back-gate oxide/channel interface ψ_{S1} can be expressed as a function of Q_s:

$$Q_{total} = \epsilon_{Si} \cdot \sqrt{\frac{2kTn_i}{\kappa_{Si}\epsilon_0} \cdot \left(exp(\frac{q\cdot\psi(x)}{kT}) \ - exp(\frac{q\cdot\psi_{S2}}{kT}) \ \right) + \left(\frac{Q_S}{\kappa_{Si}\epsilon_0}\right)^2} \tag{7.16}$$

$$\psi_{S1}\left(Q_S\right) = \frac{kT}{q} ln \left[\left(\frac{Q_S \cdot Q_{ch}}{kT \cdot \kappa_{Si}\epsilon_0 \cdot n_i}\right) - ln \left(exp\left(\frac{Q_S}{kT \cdot C_{Si}}\right) \ - 1\right) \ \right] \tag{7.17}$$

where Q_{ch} is defined as the charge density inside the Si channel when the V_g reach the threshold voltage.

By inserting Eq. 7.16 and 7.17 back to the general expression for gate voltage:$V_G = \psi_{S1} + \psi_{fb} - \frac{Q_{total}}{C_{ox}}$, the overall front gate threshold voltage shift can be calculated as:

$$\begin{aligned} &\Delta V_{th}\left(Q_S\right) = V_{th}\left(Q_S\right) - V_{th}\left(0\right) \\ &= - \frac{Q_S}{C_{ox}} + \frac{kT}{q} \ln \left[\left(\frac{Q_S \cdot Q_{ch}}{kT \cdot \kappa_{Si}\epsilon_0 \cdot n_i}\right) - ln \left(exp\left(\frac{Q_S}{kT \cdot C_{Si}}\right) \ - 1\right) \ \right] - \frac{kT}{q} \ln \left(\frac{Q_{ch}}{t_{Si} \cdot n_i}\right) \end{aligned} \tag{7.18}$$

The physical meaning of Eq. 7.18 is clear, the first three terms containing Q_s correspond to the additional back-gate surface charge Na^+ that have penetrated the encapsulant. Both gate oxide capacitance C_{ox} and Si capacitance C_{si} play important role in this expression. The last term relates to the ΔV_{th}under standard MOSFET operation.

We can also express the $I_{ds} - V_{gs}$ relation under the influence of Q_S as [168]:

$$\begin{aligned} I_{ds} &= \mu \frac{W}{L} \int_0^{V_{ds}} Q_{ch} dV_{ch} \\ &= \mu \frac{W}{L} \frac{(kT)^2 \cdot n_i \cdot \kappa_{Si} \epsilon_0}{Q_S} \cdot \exp\left[\frac{q}{kT}\left(V_{gs} - \Psi_{FB} + \frac{Q_S}{C_{ox}}\right)\right] \\ &\quad \cdot \left[\exp\left(\frac{qQ_S}{kTC_{Si}}\right) - 1\right] \cdot \left[1 - exp(-\frac{V_{ds}q}{kT})\right] \end{aligned} \tag{7.19}$$

Fig.. 7.3 C shows the $I_{ds} - V_{gs}$ curves with different Q_S. In the sub-threshold region, the analytical solutions (solid lines) match perfectly with the Sentaurus numerical device simulation results (symbols). Fig. 7.3 D shows the corresponding ΔV_{th} as a function of Q_S, with good match between the numerical and analytical simulations.

Fig. 7.3 F shows the experimental data for the overall back-gated MOSFET threshold voltage shift for a soaking period of 5 days. To accelerate the ion penetration, the soaking test was conducted at 96°C. For simplicity, we assume that Na^+ diffusion coefficient follows an Arrhenius relationship [170]. The externally applied voltage ranges from 0V to 4.5V, with an increment of 1.5V. The drift-diffusion process is accelerated with increasing V_0, which leads to an increasing ΔV_{th}. As we have mentioned in section 7.2, another interesting observation is that ΔV_{th} increases non-linearly as a function of time. This phenomenon is caused by the dissolution of ion barrier (thermal SiO_2 in the experiment) at extreme high temperature (96°C). As the encapsulation layer shrinks, the average electric field across the encapsulant rises, which further accelerates the ion penetration process. Thus, we apply the dissolution model from section 7.2 with the experimentally calibrated dissolution rate ∼90 nm/ day at 96 ^{o}C. The analytical results predicted by this model (solid lines) perfectly reproduce the experimental data (solid dots).

With the validated model both for front-gated and back-gated MOSFETs, we are now ready to develop design principles for application-specific robust encapsulation of the WIE systems.

7.4 Results and Discussions

In this section, we will use both the numerical and analytical models to develop guidelines for the design of ion encapsulation layer. We will compare the performance of two widely used encapsulation layer materials (SiO_2 and SiN_x) along with their coupled bi-layer structure. Finally, we will provide a phase plot for mapping the failure time for back-gated MOSFET at various bias and temperature.

We apply the EIBT relationship derived in section 7.3 for thermal SiO_2 and SiN_x. Comparing to a 200 nm SiN_x encapsulation layer, the EIBT for SiO_2 is $\sim$ 4500 nm by Eq. 7.14. In Fig. 7.4 D, we plot the front-gate MOSFET ΔV_{th} vs. t for both designs. Except for slight initial difference, the two curves are essentially identical for $t>t_1$. Therefore, a 200 nm SiN_x layer has the same ion blocking capability as a 4500 nm SiO_2 layer. Obviously, materials with low ion diffusion coefficient is a good encapsulation layer candidate material especially for thin-film front-gate MOSFET based WIE systems, but the additional effect of the dielectric constant (κ) is equally important and must be accounted for.

If SiN_x is so effective in preventing ion-diffusion, then why not design encapsulation layers based exclusively on SiN_x? Recall that in the analysis above, we focused exclusively on ion-induced instability of MOSFETs. Moisture penetration and corresponding corrosion/delamination, however, could be equally important degradation mechanisms for WIE system. In our previous work [156], we experimentally demonstrated that while thermal SiO_2 is a good moisture barrier material, SiN_x is not. Therefore, the requirement for multi-objective encapsulation against moisture, ion presentation, and hydrolysis requires a stacked encapsulation approach, as follows.

As an illustrative example, let us consider a bi-layer SiO_2/SiN_x encapsulation where the top thermal SiO_2 layer (h_1=300nm) prevents moisture ingress, while the bottom SiN_x layer (h_2=200nm) suppresses Na^+ penetration, see Fig. 7.2 A. As before, we solve the coupled drift-diffusion equation and Poisson's equation (Eq. 7.1 and 7.2) for a 1-D domain, with a V_0= $3V$. The diffusion coefficients at 37 $^\circ C$ are:

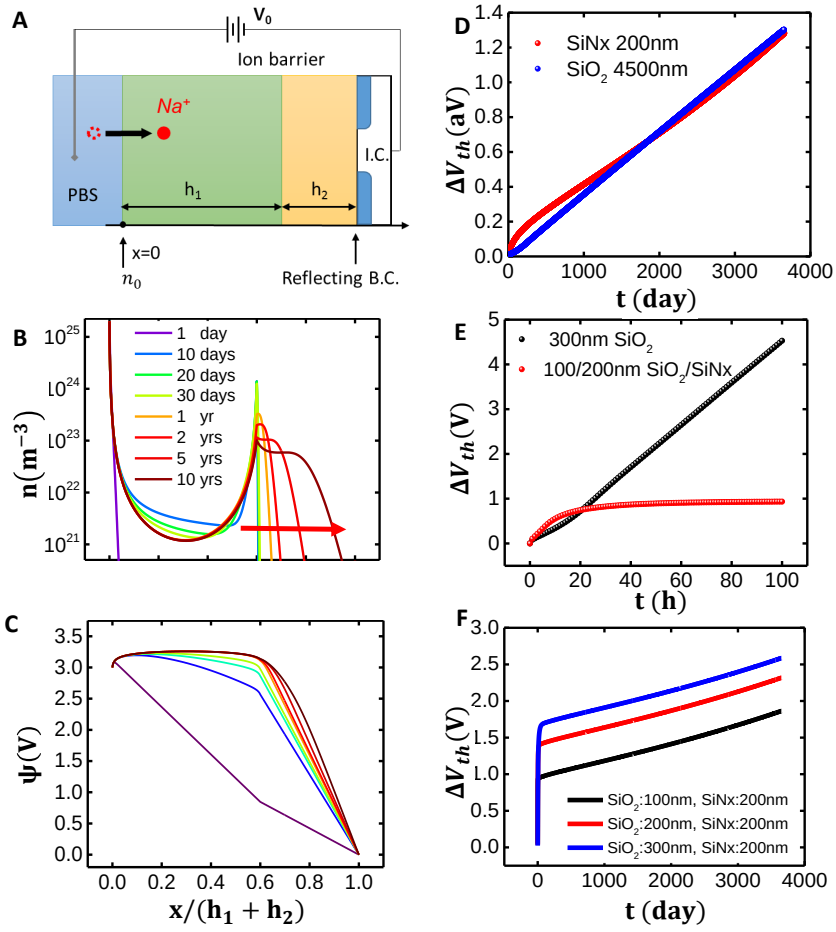

Fig. 7.4.: A comparison of single layer/bi-layer encapsulant for front-gate MOSFET case. A. Schematic illustration of sodium ion penetration in 1-D bi-layer ion barrier domain with external applied voltage V_0. B-C. Na^+ concentration, electrical field and potential distribution within $h_1 = 300nm$ thermal SiO_2 and $h_2 = 200nm$ SiN_x bi-layer ion barrier structure at the end various simulation time. The external bias is fixed at 3 V. D. Comparison of front gate MOSFET ΔV_{th} for 200 nm SiN_x and 4500 nm SiO_2. E. Comparison of front gate MOSFET ΔV_{th} under 1) 300 nm single layer SiO_2 ion barrier. 2) 100/200 nm SiO_2/SiN_x bi-layer ion barrier. F. Comparison of front gate MOSFET implantable device ΔV_tunder $SiO_2/SiNx$ bi-layer structure with (100/200)/300 nm SiO_2 and 200 nm SiN_x .

$6.53\times10^{-21}m^2/s$ for thermal SiO_2 and $4.94\times10^{-25}m^2/s$ for SiN_x . Due to the four orders of magnitude difference in the diffusion coefficients, Na^+ penetrates the top SiO_2 layer at a much faster rate than the SiN_x layer. Fig. 7.4 B shows that within the first 10 days, Na^+ build up inside the SiO_2 layer and reach a quasi-static profile. At the SiO_2/SiN_x interface, Na^+ accumulates because of the Na^+ influx coming from the thermal SiO_2 side is much larger than the outflow into the SiN_x side. After this initial transient, Na^+ begins to slowly penetrate into the SiN_x layer. From 1 year up to 10 years, the drift-front of Na^+ slowly approaches the SiN_x layer. During this period, the accumulated Na^+ peak at SiO_2/SiN_x interface gradually reduces in order to balance the amount of Na+ injected into the SiN_x layer.

Fig.. 7.4 C shows the potential distribution inside SiO_2/SiN_x bi-layer structure. Initially, there is no free charge in the dielectrics, therefore the potential drops linearly over the two layers, with the ratio defined by their respective dielectric constants. Once Na^+ penetrates and saturates within SiO_2 layer, the potential at the SiO_2/SiN_x interface rises quickly and approaches V_0. At the end of first month, most of potential drop distributes linearly over the SiN_x layer. After 1 year, a self-induced potential barrier with $V_{max} > V_0$ builds up inside the SiO_2 layer. The potential distribution across the SiN_x layer gradually shows a non-linear profile reflecting the slow penetration of Na^+ ions.

To compare the performance of the bi-layer ion barrier design to the single layer SiO_2 structure, we plot ΔV_{th} vs. t for front gate case from our numerical simulation in Fig. 7.4 E. For the bi-layer layer structure (red line), ΔV_{th} increases within 0 to 20 hours, then saturates to a constant value. The initial ΔV_{th} jump is due to the large amount of Na^+penetrating into the SiO_2 layer where the ion diffusivity is relatively large. The saturation happens when Na^+ reach the second SiN_x layer and penetrates at a much slower rate. For a single layer SiO_2(black line), however, there is no second ion barrier. As a result, ΔV_{th} increase and the implanted MOSFET device degrades at a much faster rate.

Fig. 7.4 F explores the influence of the thickness of the top thermal SiO_2 layer (h_1) on the overall MOSFET degradation. We numerically simulate three bi-layer structures with 100, 200 and 300 nm top layer SiO_2 thickness and keep the same $200nm$ thickness of SiN_x. Counter-intuitively, the thickner SiO_2 top layer produces higher initial ΔV_{th} jump; although one expects thicker oxides to *reduce* degradation. This counter-intuitive result can be explained as follows. As illustrated by Eq. 7.11, it is not the density, but the *density moment* of the spatially distributed Na^+ ions in the encapsulant that define to the threshold voltage shift of a front-gated MOSFET. Fig. 7.4 B shows that Na^+ ions penetrate through the top SiO_2 layer and reach a saturated density profile in a relatively short period of time, however in a thicker oxide, the *density moment* of the charge profile, especially the peak at the SiO_2/SiN_x interface, resides further away from the MOSFET top gate interface compared to a thinner oxide. This larger moment of Na^+ in SiO_2 layer in thicker oxides accounts for the higher initial ΔV_{th} jump in Fig. 7.4 F. After the initial jump, all three lines become parallel to each other and increase at a much slower rate reflecting Na^+ diffusion into the second SiN_x layer. From the pure ion penetration point of view, thinner top moisture layer can effectively slow down the front gate MOSFET device degradation process. But if we consider the dissolution of the barrier material, there is a trade off in the design of the moisture barrier layer thickness. We can select an optimal thickness of moisture barrier layer by considering both the material dissolution as well as Na^+ penetration.

Next, we are going to utilize our model to map the back-gate implantable MOSFET failure time from the high-temperature soaking test back to their normal operation temperature. Fig. 7.5 shows a phase plot of $V_0$and$T$ dependent failure-time ($t_{failure}$) of back gate MOSFET implantable device. The symbols are from our numerical simulation, while the lines are calculated from our analytical model, derived by combining Eq. 7.9 and Arrhenius equation to relate $t_{failure}$, T and V_0,

$$\ln\left(t_{failure}\right) = \frac{E_A}{kT} - \ln\left(\frac{\kappa\epsilon_0 D_0}{kTqh}\cdot \mathrm{V_0}^2\right) + \text{Constant} \tag{7.20}$$

where D_0 is the pre-exponential factor and E_A is the activation energy.

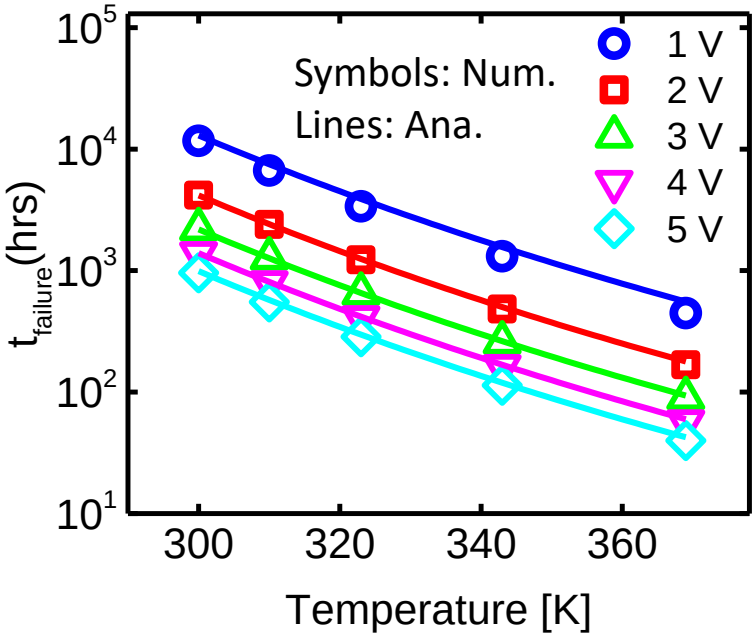

Fig. 7.5.: Phase plot of back-gate MOSFET failure time as a function of temperature with sweeping V_0.

In this particular case, we choose $t_{failure}$ to correspond to $\Delta V_{th} = 1V$, related to the surface Na^+density of, $Q_{s,th}/q \sim 3\times10^{15}m^{-2}$, see Fig. 7.3 C. Several observations can be made from the phase plot. First, the numerical and analytical results both support the trend that lifetime is reduced at higher temperature due to the enhanced Na^+mobility. Second, high external bias V_0 accelerate the Na^+ drift process and shortens the MOSFET failure time. We note that the while the match between analytical and numerical results are good, they are not exact, especially at low V_0. This is because our analytical model presumed ion diffusion to be unimportant compared to ion drift. This is a poor approximation at very low V_0. As a result, the failure time from the numerical simulation is slightly shorter than the analytical one at low bias ($V_0 = 1V$). At higher bias, drift dominates diffusion, and the difference disappears.

From the failure time phase plot, we can simply map the failure time in high-temperature soaking test back to the normal operation temperature device failure time under different external bias voltage profiles.

7.5 Conclusions

The stability of MOSFET-based electronic components in WIE systems is of great interest. Ion penetration is one of the most significant problems that degrade the device performance. The design of proper encapsulation layer requires systematic theoretical analysis. In this chapter, we have developed numerical and analytical frameworks for lifetime prediction of MOSFET-based components in WIE systems. More generally, the modeling framework can be used for solving ion penetration problems in a broad range of electrochemical applications. The predictions are validated by accelerated soaking experiment. The model suggests optimum design given multiple design parameters (such as encapsulation thickness, ion diffusivity in an encapsulation material, temperature, and external voltage bias and encapsulation layer dissolution). Our analysis suggests that a bi-layer or tri-layer encapsulation may be essential for multi-objective protection. Since this chapter focuses on the design of encapsulants as ion/moisture barrier, we have compared the blocking effectiveness of inorganic encapsulants. For *in vivo* applications, however, a layer of organic material (such as parylene C) must be added to the encapsulant stack to satisfy the bio-compatibility requirements between body tissue and the WIE systems.

8. SUMMARY AND FUTURE WORK

8.1 Summary of thesis

In this thesis, we have developed end-to-end physics-based modeling frameworks for two IoT-based applications: personalized medicine and precision agriculture. By coupling the physics of analyte mass transfer, electrochemical reactions, and electrostatics, the frameworks have explored the geometrical and electrochemical limits of electrochemical biosensors and has provided guidelines for improving the sensitivity, enhancing the selectivity, reducing the response time, and increasing the signal-to-noise ratio for the next generations of electrochemical biosensors. The innovations include: 1) high sensitivity nano-electrode non-enzymatic/enzymatic amperometric glucose sensors, 2) self-powered enzymatic biofuel cell (EBFC)-based lactate sensors, and 3) roll-to-roll printed thin-film ion-selective electrode (ISE)-based soil nitrate sensors. The frameworks have also included quantitative modeling of the general reliability issues for the IoT edge-computing electronics in the system integration level. The specific contributions are summarized below:

8.1.1 Summary and conclusions from chapter 2 : nanoparticle-based amperometric glucose biosensors

Nanoparticle-based amperometric glucose sensors (on CNT, graphene, and liquid crystal polymer(LCP) substrate) have demonstrated exceptionally fast and highly sensitive detection of glucose concentration in both *in vivo* and *in vitro* applications. Those sensors are potential candidates for being integrated into sophisticated multi-functional wearable systems that detect glucose concentration in sweat, saliva, and

tears, with the hope of obviating the need for repeated needle pricks, for example, in diabetes. We have made the following contributions:

1. We have provided a compact analytic model that describes the steady-state current response of nanoparticle-based amperometric glucose sensor.

2. We have generalized the theory to include the impact of geometrical, physical and chemical parameters that are uniquely correlated to its nanoparticle structure.

3. We have modeled the nanoparticle sensor structure in two density limits: isolated nanoparticle limit and chain nanoparticle limit. Those two limits distinguish the glucose diffusion and hydrogen peroxide recapture processes by different geometrical considerations.

4. We have illustrated the implications of the model regarding the scaling of the nanoparticles and optimization of nanoparticle distribution which could enhance the overall output current response and sensitivity.

We conclude that the sensitivity of the NP amperometric sensor is enhanced by the nanoparticle electrodes in two ways: 1) the geometric properties of the nanoparticles increase the total electrode active area within the same electrode footprint. 2) The neighboring nanoparticles help recapture more H_2O_2 and generate larger current.

Our modeling frameworks are ideally suited to interpret and optimize nanoparticle-based amperometric glucose sensors. This would help researchers in nanostructured biosensor design for complex integrated systems.

8.1.2 Summary and conclusions from chapter 3 : metal oxide-based non-enzymatic glucose sensor

In chapter 3, we have provided the first systematic theoretical study of performance limits, dynamic range, and parametric dependencies of a non-enzymatic glu-

cose sensor and consistently interpret the amperometric response associated with experiments involving a variety of nanostructured substrates. Our theoretical approach based on the equivalent diffusion capacitance can be easily generalized to other nanostructured electrode geometries. The model has been used to explore the effectiveness of various design parameters and provide guidelines to improve the overall steady-state performance of this non-enzymatic glucose sensor. The key contributions from chapter 3 are as follows:

1. We have provided a compact analytical model that describes the steady-state current response of non-enzymatic metal oxide-based amperometric glucose sensors.

2. We have generalized the theory to include the impact of geometrical, physical and chemical parameters that uniquely characterize the non-enzymatic reactions and the nanostructured electrode. We found the quantitative correlation between the characteristics of the analytical signal of the sensor (sensitivity, limit of linearity, etc.) and the properties of different metal oxide and nanoelectrode materials.

3. We have both numerically and analytically simulated the diffusion-reaction processes and validate the accuracy of our model by multiple experimental results published by a variety of groups worldwide. The theoretical model unifies the seemingly disparate (or even contradictory) results associated with these sensors.

4. We have illustrated the implications of the model regarding scaling of the nanostructured electrode geometry (such as radius and density of the nanowire electrode, the surface density of the metal oxide on the electrode) and different reaction constants by changing the metal oxide morphology or chemical component.

5. From our model, we have demonstrated the advantages of nanowire material over the traditional planar electrode. We have also compared the performance of non-enzymatic glucose vs. widely used enzymatic glucose sensor and have indicated their scope of applications.

We conclude that while non-enzymatic glucose sensor still does not have sufficient dynamic range to replace the classical blood glucose sensors, these sensors could be useful for low concentration glucose sensing applications involving sweat, saliva, and ocular fluid.

8.1.3 Summary and conclusions from chapter 4 : Self-powered Enzymatic Biofuel Cell (EBFC) Amperometric Sensor

Chapter 4 has provided the first systematic theoretical study of performance limits, dynamic range, and parametric dependencies of an EBFC-based biosensor and consistently interpreted the output response associated with experiments involving a variety of operating conditions. The model has been used to explore the effectiveness of various design parameters and to provide guidelines to improve the overall steady-state performance of EBFC-based biosensors. The key contributions of chapter 4 are as follows:

1. We have provided an elegant yet simple equivalent circuit model that captures the complex, three-dimensional interplay between coupled catalytic redox reactions occurring in an EBFC-based sensor.

2. We have used sophisticated numerical modeling plus simple analytical formulas to capture the essential physics, which agrees closely with the sensor experimental measurements.

3. We have generalized the theory to include the fundamental impact of different design parameters of EBFC-based sensors on their detection performance. We have showed that the surface densities of oxidoreductase enzyme and electron

transfer mediators had very different influences on the various features of the response, such as the sensitivity and the linear dynamic region.

4. We found that redox reaction at the cathode can potentially become the rate-limiting factor. Our equivalent circuit model has provided a quantitative option for inspecting the role of cathode reactions. In the specific case of the lactate EBFC sensor, the *oxygen starvation* effect is critical and should be carefully handled for the application of real-time wearable biosensors.

Based on our model, we conclude that the linear dynamic range and sensitivity of the EBFC-based sensor can be fine-tuned by changing the surface density of enzymes and electron mediators at the anode and by enhancing reductant concentrations at the cathode. But there are the trade-offs among chemical design parameters such as various reaction constants as well as electrical parameters in the Butler-Volmer relationship.

Our theoretical approach based on a self-consistent equivalent circuit model can be easily adapted to understand a wide range of two-electrode systems, including sensors, fuel cells, and energy storage devices.

8.1.4 Summary and conclusions from chapter 5 and chapter 6 : ion-selective electrode (ISE) sensors

In chapter 5 and chapter 6, we developed design guidelines for thin-film solid-contact ion-selective electrode (ISE) sensors. Specifically, we fabricated ISE nitrate sensors for soil fertilizer level detection to improve farm-to-folk productivity. The fabrication process involves roll-to-roll (R2R) nano-manufacturing facility which enables high throughput at low cost. We developed a fundamental physics-based model to describe both the steady-state response and the transient response of ISE sensor.

The key contributions of chapter 5 are as follows:

1. Our detailed numerical simulation has provided physics-based insights regarding the ISE emf output generated by the electrostatic redistribution of different ions at the ion-selective membrane phase boundary.

2. Our model has quantified the correlation between the ISE response time and different R2R ISE manufacturing parameters (e.g., membrane thickness, membrane dielectric constant)

3. We have discovered a new universal scaling phenomenon in the transient response of ISE. Validated by the experimental measurement data, we have derived a simple analytical model where the universal transient slope shows an interesting 60mV/dec Nernst relationship in time.

In chapter 6, we deployed the theory from chapter 5 to engineer and optimize the general solid-contact ISE design:

1. We have statistically analyzed the variability of ISE experimental measurement data and identified the noise signal within each sensor electrode measurement as Johnson-Nyquist noise generated by thermal agitation of different molecules.

2. We have successfully predicted and reduced the effect of ion-selective membrane variation on output emf voltage by image analysis and machine learning methods.

3. We have suggested the development of a new graphene-based ISE design to reduce ISE response time and sensor-to-sensor variations.

Based on our theoretical analysis, we conclude that the conventional logarithmic Nernst relationship in the steady-state can be extended in the time domain. For a thin solid-contact ISE, the ion-selective membrane thickness plays a significant role due to the accumulation and depletion of target ions in the entire membrane region.

8.1.5 Summary and conclusion from chapter 7 : Stability of MOSFET-based Electronic Components in Wearable and Implantable Systems

Long-term electromechanical stability and reliability are critical challenges for the next generation of Wearable and Implantable Electronic (WIE) systems. Protecting the built-in electronic components (such as MOSFET-based sensors) in a harsh fluidic environment is difficult because the requirement of wearability/flexibility demands ultra-thin encapsulation. The charged ions (such as Na^+) from the body-fluids can diffuse rapidly through the thin encapsulation layer and destabilize the entire system. However, a theory predicting degradation lifetime and relating multiple design parameters is lacking, which we have provided in our work as follows:

1. We have offered both a numerical framework and an analytical model for Na^+ transport through the encapsulation layer. Coupled with the physics of MOSFET degradation, the ion diffusion model has predicted the lifetime of MOSFET-based wearable electronics encapsulated by various types of coating materials.

2. We have utilized our model to include multiple design parameters, such as stacks of encapsulation layers, encapsulation layer thicknesses, temperature/field dependent ion drift and rate of dissolution of the encapsulation layer, etc.

3. Our analysis suggested that a bi-layer or tri-layer encapsulation may be essential for multi-objective protection. However, the thickness needs to be optimized by considering both charged ion penetration and dissolution of the encapsulation layer.

In conclusion, our work have suggested optimum design given multiple design parameters such as encapsulation thickness, ion diffusivity in an encapsulation material, temperature, and external voltage bias and encapsulation layer dissolution. We inspected different encapsulant material properties and found that: thermal SiO_2 pre-

vents moisture diffusion, SiN_xcan be used for design of ion barrier layer, and HfO_2 is a good candidate for anti-corrosion.

To summarize, this thesis has provided generalized physics-based modeling frameworks exploring the geometrical and electrochemical limitations of of novel electrochemical biosensors for IoT integration. It provides guidelines for improving the sensitivity, enhancing the selectivity, reducing the response time, increasing the signal-to-noise ratio, and improving the lifetime. While these works address challenges in amperometric and potentiometric sensing systems, future works are warranted to achieve better component-level performance and successful system integration. Below are some interesting research directions worth exploring:

8.2 Future research directions

8.2.1 Paper-based smart bandage

Paper-based smart bandage integrated systems have become a hot topic recently for the advantage of low-cost, easy accessibility, and low power consumption [171]. Paper-based sensors detect signs of an infection in a simple and convenient way. For example, samples placed on a paper chip contain beads of colorimetric chemical components. Clumps around the bead could be formed around the target particle, changing the color of the paper chip [172]. Smartphone camera could analyzes the image and determine the target analyte concentration. Drugs or antibodies embedded in the nanofiber of the paper-based smart bandage could be actively triggered to release. Paper-based smart bandage system is highly foldable, allowing a series of diagnostic experiments extended in the time dimension [173]. The chemical compounds in the paper-based bandage carries their own energy, greatly reducing the need for external high-density power source.

Traditional modern electrochemical sensors could also be integrated into the paper-based bandage system (e.g., the thin-film ISE introduced in this thesis could be combined with Organic Electrochemical Transistor (OECT) technology [174] on a

paper-based flexible platform). To design and optimize the performance of smart bandages, a systematic theoretical understanding of various microscopic processes (diffusion of analytes of different sizes, virus, biomolecules, bacteria, etc. within the paper nanofiber, optical and colorimetric properties of the paper, and the device physics of organic transistor that correlate the sensor electrochemical response) and physics-based modeling frameworks of paper-based sensing and drug-releasing components would be a worthy topic of research. Scalable manufacturing process involving roll-to-roll printing technology, for instance, could also be adapted to enhance the large-scale fabrication and reduce the cost of paper-based bandage systems.

8.2.2 Improvement of the solid-state reference electrode

Another key component of both amperometric and potentiometric sensors is the reference electrode. Maintaining a stable electrochemical potential for a long period of time while miniaturizing the size of the reference electrodes are the two main challenges that facing the design of electrochemical biosensors for systematic integration. The solid-state reference electrode (S.S. Ref.) is considered as a good candidate for next-generation IoT sensor applications. A comprehensive model for solid-state reference electrode is highly desirable for identifying the factors in S.S Ref. electrode response time and Nernstian condition such as the ionic mobility and position between ISE and S.S. Ref.

8.2.3 Programmable encapsulant

A smart encapsulant design for implantable electronics that protect the system for a desired period of time. The smart encapsulant can be thermally or optically triggered to either partially destroyed or completely resorbed by the body or self-dissolved in the environment. The programmable encapsulant will have broad application prospects such as drug release in the application of medical care and deposition of electronics in the soil for precision agriculture. The smart encapsulant would be

highly desirable for thin-film skin-mounted wearable system or paper-based bandage systems.

8.3 Epilogue

Looking into the future, human beings are standing at the next development front: the starting point of the Internet of Things (IoT) discussed in this thesis. Human history will once again take a big step forward. While looking forward to a better future, however, we cannot ignore the challenges we are facing: Ebola virus and novel coronavirus are spreading on the land of Africa and Asia; Non-renewable resources such as cultivated land and oil on the earth are constantly decreasing; Forest fires caused by global warming and climatic anomalies are raging in Australia and the American continent; the rapid rise of artificial intelligence is like a double-edged sword, while benefiting human beings, there is still a potential threat to human information security. Faced with unknown dangers and challenges, human beings are still scared by their own weakness and vulnerability. The research results presented in this thesis only make a modest contribution to address the grand challenges. But with many small contributions like this, we will be able to ultimately solve the problems facing humanity.

REFERENCES

REFERENCES

[1] F. Mattern and C. Floerkemeier, "From the internet of computers to the internet of things," *From active data management to event-based systems and more*, pp. 242–259, 2010.

[2] K. Ashton, "That 'internet of things' thing," *RFiD Journal*, vol. 22, no. 7, 2011.

[3] A. Nordrum, "Popular internet of things forecast of 50 billion devices by 2020 is outdated," *IEEE Spectrum*, vol. 18, 2016.

[4] G. Santucci, "The internet of things: Between the revolution of the internet and the metamorphosis of objects," *Vision and Challenges for Realising the Internet of Things*, pp. 11–24, 2010.

[5] O. Vermesan and P. Friess, *Internet of things: converging technologies for smart environments and integrated ecosystems*. River Publishers, 2013.

[6] S. Ajami and F. Teimouri, "Features and application of wearable biosensors in medical care," *Journal of research in medical sciences: the official journal of Isfahan University of Medical Sciences*, vol. 20, no. 12, p. 1208, 2015.

[7] E. Sazonov and M. Neuman, *Wearable Sensors: Fundamentals, Implementation and Applications*. ACADEMIC PressINC, 2017. [Online]. Available: https://books.google.com/books?id=R3TJDAEACAAJ

[8] D. Konstantas, "An overview of wearable and implantable medical sensors," *Yearbook of medical informatics*, vol. 7, no. 1, pp. 66–69, 2007.

[9] R. T. Li, S. R. Kling, M. J. Salata, S. A. Cupp, J. Sheehan, and J. E. Voos, "Wearable performance devices in sports medicine," *Sports health*, vol. 8, no. 1, pp. 74–78, 2016.

[10] J. A. Ritter, M. R. Bean, G. Burnett, R. Mieskoski, V. Finomore, and L. G. Militello, "Tools for battlefield airmen: Where we've been and where we're going," in *Proceedings of the Human Factors and Ergonomics Society Annual Meeting*, vol. 55. SAGE Publications Sage CA: Los Angeles, CA, Conference Proceedings, pp. 2069–2072.

[11] Y.-L. Zheng, X.-R. Ding, C. C. Y. Poon, B. P. L. Lo, H. Zhang, X.-L. Zhou, G.-Z. Yang, N. Zhao, and Y.-T. Zhang, "Unobtrusive sensing and wearable devices for health informatics," *IEEE Transactions on Biomedical Engineering*, vol. 61, no. 5, pp. 1538–1554, 2014.

[12] A. McBratney, B. Whelan, T. Ancev, and J. Bouma, "Future directions of precision agriculture," *Precision agriculture*, vol. 6, no. 1, pp. 7–23, 2005.

[13] J. V. Stafford, "Implementing precision agriculture in the 21st century," *Journal of Agricultural Engineering Research*, vol. 76, no. 3, pp. 267–275, 2000.

[14] P. Reyns, B. Missotten, H. Ramon, and J. De Baerdemaeker, "A review of combine sensors for precision farming," *Precision Agriculture*, vol. 3, no. 2, pp. 169–182, 2002.

[15] L. Ruiz-Garcia, L. Lunadei, P. Barreiro, and I. Robla, "A review of wireless sensor technologies and applications in agriculture and food industry: state of the art and current trends," *sensors*, vol. 9, no. 6, pp. 4728–4750, 2009.

[16] J. Ma, X. Zhou, S. Li, and Z. Li, "Connecting agriculture to the internet of things through sensor networks," in *Internet of Things (iThings/CPSCom), 2011 International Conference on and 4th International Conference on Cyber, Physical and Social Computing*. IEEE, Conference Proceedings, pp. 184–187.

[17] V. I. Adamchuk, J. Hummel, M. Morgan, and S. Upadhyaya, "On-the-go soil sensors for precision agriculture," *Computers and electronics in agriculture*, vol. 44, no. 1, pp. 71–91, 2004.

[18] J. X. Zhang and K. Hoshino, *Molecular Sensors and Nanodevices: Principles, Designs and Applications in Biomedical Engineering*. Academic Press, 2018.

[19] E. Akbari, R. Moradi, A. Afroozeh, A. Alizadeh, and M. Nilashi, "A new approach for prediction of graphene based isfet using regression tree and neural network," *Superlattices and Microstructures*, vol. 130, pp. 241–248, 2019.

[20] J. S. Daniels and N. Pourmand, "Label-free impedance biosensors: Opportunities and challenges," *Electroanalysis: An International Journal Devoted to Fundamental and Practical Aspects of Electroanalysis*, vol. 19, no. 12, pp. 1239–1257, 2007.

[21] E. P. Randviir and C. E. Banks, "Electrochemical impedance spectroscopy: an overview of bioanalytical applications," *Analytical Methods*, vol. 5, no. 5, pp. 1098–1115, 2013.

[22] L. Su, W. Jia, C. Hou, and Y. Lei, "Microbial biosensors: a review," *Biosensors and Bioelectronics*, vol. 26, no. 5, pp. 1788–1799, 2011.

[23] W. Gao, S. Emaminejad, H. Y. Nyein, S. Challa, K. Chen, A. Peck, H. M. Fahad, H. Ota, H. Shiraki, D. Kiriya, D. H. Lien, G. A. Brooks, R. W. Davis, and A. Javey, "Fully integrated wearable sensor arrays for multiplexed in situ perspiration analysis," *Nature*, vol. 529, no. 7587, pp. 509–14, 2016. [Online]. Available: http://www.ncbi.nlm.nih.gov/pubmed/26819044

[24] H. Lee, T. K. Choi, Y. B. Lee, H. R. Cho, R. Ghaffari, L. Wang, H. J. Choi, T. D. Chung, N. Lu, T. Hyeon, S. H. Choi, and D.-H. Kim, "A graphene-based electrochemical device with thermoresponsive microneedles for diabetes monitoring and therapy," *Nat Nano*, vol. advance online publication, no. 6, pp. 566–72, 2016. [Online]. Available: http://dx.doi.org/10.1038/nnano.2016.38http://www.nature.com/nnano/journal/vaop/ncurrent/pdf/nnano.2016.38.pdf

[25] A. J. Bandodkar, P. Gutruf, J. Choi, K. Lee, Y. Sekine, J. T. Reeder, W. J. Jeang, A. J. Aranyosi, S. P. Lee, and J. B. Model, "Battery-free, skin-interfaced microfluidic/electronic systems for simultaneous electrochemical, colorimetric, and volumetric analysis of sweat," *Science advances*, vol. 5, no. 1, p. eaav3294, 2019. [Online]. Available: https://www.ncbi.nlm.nih.gov/pubmed/30746477

[26] R. Rosenberg, "Screen-printed ion selective electrodes for soil ion detection," Thesis, 2016.

[27] K. Ogurtsova, J. da Rocha Fernandes, Y. Huang, U. Linnenkamp, L. Guariguata, N. Cho, D. Cavan, J. Shaw, and L. Makaroff, "Idf diabetes atlas: Global estimates for the prevalence of diabetes for 2015 and 2040," *Diabetes Research and Clinical Practice*, vol. 128, pp. 40–50, 2017.

[28] L. C. Clark, R. Wolf, D. Granger, and Z. Taylor, "Continuous recording of blood oxygen tensions by polarography," *Journal of Applied Physiology*, vol. 6, no. 3, pp. 189–193, 1953. [Online]. Available: http://jap.physiology.org/content/jap/6/3/189.full.pdf

[29] G. G. Guilbault and G. J. Lubrano, "An enzyme electrode for the amperometric determination of glucose," *Analytica Chimica Acta*, vol. 64, no. 3, pp. 439–455, 1973. [Online]. Available: http://www.sciencedirect.com/science/article/pii/S0003267001824764

[30] X. Zhang, H. Ju, and J. Wang, *Electrochemical sensors, biosensors and their biomedical applications*. Academic Press, 2011.

[31] 2014. [Online]. Available: https://googleblog.blogspot.com/2014/01/introducing-our-smart-contact-lens.html

[32] M. Scott, "Novartis joins with google to develop contact lens that monitors blood sugar," *The New York Times*, vol. 15, 2014.

[33] J. D. Lane, D. M. Krumholz, R. A. Sack, and C. Morris, "Tear glucose dynamics in diabetes mellitus," *Current eye research*, vol. 31, no. 11, pp. 895–901, 2006.

[34] A. D. Association, "Diagnosis and classification of diabetes mellitus," *Diabetes care*, vol. 37, no. Supplement 1, pp. S81–S90, 2014.

[35] G. S. Wilson and Y. Hu, "Enzyme-based biosensors for in vivo measurements," *Chemical Reviews*, vol. 100, no. 7, pp. 2693–2704, 2000.

[36] M. Jamal, J. Xu, and K. M. Razeeb, "Disposable biosensor based on immobilisation of glutamate oxidase on pt nanoparticles modified au nanowire array electrode," *Biosensors and Bioelectronics*, vol. 26, no. 4, pp. 1420–1424, 2010. [Online]. Available: http://ac.els-cdn.com/S095656631000446X/1-s2.0-S095656631000446X-main.pdf?_tid=27d6aec2-65f3-11e5-a8d0-00000aacb361&acdnat=1443453252_51c89280e46d1bde74c0ff41f1972f5c

[37] X. Jiang, Y. Wu, X. Mao, X. Cui, and L. Zhu, "Amperometric glucose biosensor based on integration of glucose oxidase with platinum nanoparticles/ordered mesoporous carbon nanocomposite," *Sensors and Actuators B: Chemical*, vol. 153, no. 1, pp. 158–163, 2011. [Online]. Available: http://ac.els-cdn.com/S0925400510008300/1-s2.0-S0925400510008300-main.

pdf?_tid=5558a1a8-65f2-11e5-9ca4-00000aacb35e&acdnat=1443452899_e988115a3160bb4629eb732206d66fd2

[38] P. R. Nair and M. A. Alam, "Performance limits of nanobiosensors," *Applied Physics Letters*, vol. 88, no. 23, p. 233120, 2006. [Online]. Available: ⟨GotoISI⟩://WOS:000238914500073

[39] J. C. Claussen, J. B. Hengenius, M. M. Wickner, T. S. Fisher, D. M. Umulis, and D. M. Porterfield, "Effects of carbon nanotube-tethered nanosphere density on amperometric biosensing: simulation and experiment," *The Journal of Physical Chemistry C*, vol. 115, no. 43, pp. 20 896–20 904, 2011.

[40] J. C. Claussen, A. Kumar, D. B. Jaroch, M. H. Khawaja, A. B. Hibbard, D. M. Porterfield, and T. S. Fisher, "Nanostructuring platinum nanoparticles on multilayered graphene petal nanosheets for electrochemical biosensing," *Advanced Functional Materials*, vol. 22, no. 16, pp. 3399–3405, 2012.

[41] A. Yakoh, C. Pinyorospathum, W. Siangproh, and O. Chailapakul, "Biomedical probes based on inorganic nanoparticles for electrochemical and optical spectroscopy applications," *Sensors*, vol. 15, no. 9, p. 21427, 2015. [Online]. Available: http://www.mdpi.com/1424-8220/15/9/21427http://www.mdpi.com/1424-8220/15/9/21427/pdf

[42] A. Bard and L. Faulkner, *Electrochemical Methods: Fundamentals and Applications*. Wiley, 2000. [Online]. Available: https://books.google.com/books?id=kv56QgAACAAJ

[43] H. Berg, *Random Walks in Biology*. Princeton University Press, 1993. [Online]. Available: https://books.google.com/books?id=DjdgXGLoJY8C

[44] P. R. Nair and M. A. Alam, "Dimensionally frustrated diffusion towards fractal adsorbers," *Physical Review Letters*, vol. 99, no. 25, p. 256101, 2007. [Online]. Available: http://link.aps.org/doi/10.1103/PhysRevLett.99.256101http://journals.aps.org/prl/abstract/10.1103/PhysRevLett.99.256101

[45] J. Jackson, *Classical electrodynamics*. Wiley, 1975. [Online]. Available: https://books.google.com/books?id=_7rvAAAAMAAJ

[46] M. A. Wahab, S. H. Jin, A. E. Islam, J. Kim, J.-h. Kim, W.-H. Yeo, D. J. Lee, H. U. Chung, J. A. Rogers, and M. A. Alam, "Electrostatic dimension of aligned-array carbon nanotube field-effect transistors," *ACS nano*, vol. 7, no. 2, pp. 1299–1308, 2013.

[47] L. Michaelis and M. L. Menten, "Die kinetik der invertinwirkung," *Biochem. z*, vol. 49, no. 333-369, p. 352, 1913.

[48] S. Karmalkar, P. V. Mohan, H. P. Nair, and R. Yeluri, "Compact models of spreading resistances for electrical/thermal design of devices and ics," *Electron Devices, IEEE Transactions on*, vol. 54, no. 7, pp. 1734–1743, 2007. [Online]. Available: http://ieeexplore.ieee.org/ielx5/16/4252351/04252367.pdf?tp=&arnumber=4252367&isnumber=4252351

[49] Q. H. Gibson, B. E. Swoboda, and V. Massey, "Kinetics and mechanism of action of glucose oxidase," *Journal of Biological Chemistry*, vol. 239, no. 11, pp. 3927–3934, 1964.

[50] J. Parker and C. Schwartz, "Modeling the kinetics of immobilized glucose oxidase," *Biotechnology and bioengineering*, vol. 30, no. 6, pp. 724–735, 1987. [Online]. Available: http://www.ncbi.nlm.nih.gov/pubmed/18581491http://onlinelibrary.wiley.com/store/10.1002/bit.260300605/asset/260300605_ftp.pdf?v=1&t=ig3wtx90&s=0e7e10cc2970dfb9921c2b0c9aa796bdfaf8d314

[51] X. Zhang, H. Ju, and J. Wang, *Electrochemical sensors, biosensors and their biomedical applications*. Academic Press, 2011.

[52] H. Zhu, L. Li, W. Zhou, Z. Shao, and X. Chen, "Advances in non-enzymatic glucose sensors based on metal oxides," *Journal of Materials Chemistry B*, vol. 4, no. 46, pp. 7333–7349, 2016.

[53] T. Koschinsky and L. Heinemann, "Sensors for glucose monitoring: technical and clinical aspects," *Diabetes/metabolism research and reviews*, vol. 17, no. 2, pp. 113–123, 2001.

[54] G. Kokkinidis and N. Xonoglou, "Comparative study of the electrocatalytic influence of underpotential heavy metal adatoms on the anodic oxidation of monosaccharides on pt in acid solutions," *Bioelectrochemistry and Bioenergetics*, vol. 14, no. 4-6, pp. 375–387, 1985.

[55] M. Sakamoto and K. Takamura, "Catalytic oxidation of biological components on platinum electrodes modified by adsorbed metals: anodic oxidation of glucose," *Bioelectrochemistry and Bioenergetics*, vol. 9, no. 5, pp. 571–582, 1982.

[56] N. Xonoglou and G. Kokkinidis, "Catalysis of the oxidation of monosaccharides on platinum surfaces modified by underpotential submonolayers," *Bioelectrochemistry and Bioenergetics*, vol. 12, no. 5-6, pp. 485–498, 1984.

[57] K. E. Toghill and R. G. Compton, "Electrochemical non-enzymatic glucose sensors: a perspective and an evaluation," *Int. J. Electrochem. Sci*, vol. 5, no. 9, pp. 1246–1301, 2010.

[58] W. Xu, S. Dai, X. Wang, X. He, M. Wang, Y. Xi, and C. Hu, "Nanorod-aggregated flower-like cuo grown on a carbon fiber fabric for a super high sensitive non-enzymatic glucose sensor," *Journal of Materials Chemistry B*, vol. 3, no. 28, pp. 5777–5785, 2015.

[59] C. Dong, H. Zhong, T. Kou, J. Frenzel, G. Eggeler, and Z. Zhang, "Three-dimensional cu foam-supported single crystalline mesoporous cu2o nanothorn arrays for ultra-highly sensitive and efficient nonenzymatic detection of glucose," *ACS applied materials interfaces*, vol. 7, no. 36, pp. 20 215–20 223, 2015.

[60] R.-J. Chung, A.-N. Wang, Q.-L. Liao, and K.-Y. Chuang, "Non-enzymatic glucose sensor composed of carbon-coated nano-zinc oxide," *Nanomaterials*, vol. 7, no. 2, p. 36, 2017.

[61] M. Li, Q. Guo, J. Xie, Y. Li, and Y. Feng, "Cuo nanoparticles supported on nitrogen and sulfur co-doped graphene nanocomposites for non-enzymatic glucose sensing," *Journal of Nanoparticle Research*, vol. 19, no. 1, p. 11, 2017.

[62] J. Song, L. Xu, C. Zhou, R. Xing, Q. Dai, D. Liu, and H. Song, "Synthesis of graphene oxide based cuo nanoparticles composite electrode for highly enhanced nonenzymatic glucose detection," *ACS applied materials interfaces*, vol. 5, no. 24, pp. 12 928–12 934, 2013.

[63] C. Zhou, L. Xu, J. Song, R. Xing, S. Xu, D. Liu, and H. Song, "Ultrasensitive non-enzymatic glucose sensor based on three-dimensional network of zno-cuo hierarchical nanocomposites by electrospinning," *Scientific reports*, vol. 4, p. 7382, 2014.

[64] J. Q. Brown and M. J. McShane, "Modeling of spherical fluorescent glucose microsensor systems: design of enzymatic smart tattoos," *Biosensors and Bioelectronics*, vol. 21, no. 9, pp. 1760–1769, 2006. [Online]. Available: http://ac.els-cdn.com/S0956566305002575/1-s2.0-S0956566305002575-main.pdf?_tid=11797dce-3c47-11e5-b345-00000aacb360&acdnat=1438871343_ad7313cb7f40d58556fab5be9a9a0b5e

[65] R. Hovorka, V. Canonico, L. J. Chassin, U. Haueter, M. Massi-Benedetti, M. O. Federici, T. R. Pieber, H. C. Schaller, L. Schaupp, and T. Vering, "Nonlinear model predictive control of glucose concentration in subjects with type 1 diabetes," *Physiological measurement*, vol. 25, no. 4, p. 905, 2004.

[66] M. Marchesiello and E. Genies, "A theoretical model for an amperometric glucose sensor using polypyrrole as the immobilization matrix," *Journal of Electroanalytical Chemistry*, vol. 358, no. 1-2, pp. 35–48, 1993.

[67] J. Hussain, H. Jónsson, and E. Skúlason, "Faraday efficiency and mechanism of electrochemical surface reactions: Co2 reduction and h2 formation on pt (111)," *Faraday discussions*, vol. 195, pp. 619–636, 2017.

[68] A. Bard and L. Faulkner, *Electrochemical Methods: Fundamentals and Applications*. Wiley, 2000. [Online]. Available: https://books.google.com/books?id=kv56QgAACAAJ

[69] S. Park, H. Boo, and T. D. Chung, "Electrochemical non-enzymatic glucose sensors," *Analytica Chimica Acta*, vol. 556, no. 1, pp. 46–57, 2006. [Online]. Available: http://www.sciencedirect.com/science/article/pii/S0003267005009864http://ac.els-cdn.com/S0003267005009864/1-s2.0-S0003267005009864-main.pdf?_tid=e47a2c6a-4aa5-11e6-9088-00000aacb35d&acdnat=1468598884_61387975a210810909a2ae1577c8a29a

[70] P. K. Sonkar, V. Ganesan, S. A. John, D. K. Yadav, and R. Gupta, "Non-enzymatic electrochemical sensing platform based on metal complex immobilized carbon nanotubes for glucose determination," *RSC Advances*, vol. 6, no. 108, pp. 107 094–107 103, 2016.

[71] Y. Zhong, T. Shi, Z. Liu, S. Cheng, Y. Huang, X. Tao, G. Liao, and Z. Tang, "Ultrasensitive non-enzymatic glucose sensors based on different copper oxide nanostructures by in-situ growth," *Sensors and Actuators B: Chemical*, vol. 236, pp. 326–333, 2016.

[72] X. Jin, T. S. Fisher, and M. A. Alam, "Generalized compact modeling of nanoparticle-based amperometric glucose biosensors," *IEEE Transactions on Electron Devices*, 2016.

[73] L.-C. Jiang and W.-D. Zhang, "A highly sensitive nonenzymatic glucose sensor based on cuo nanoparticles-modified carbon nanotube electrode," *Biosensors and Bioelectronics*, vol. 25, no. 6, pp. 1402–1407, 2010. [Online]. Available: http://www.sciencedirect.com/science/article/pii/S0956566309005971

[74] G. Wang, X. He, L. Wang, A. Gu, Y. Huang, B. Fang, B. Geng, and X. Zhang, "Non-enzymatic electrochemical sensing of glucose," *Microchimica Acta*, vol. 180, no. 3-4, pp. 161–186, 2013.

[75] L. Burke, "Premonolayer oxidation and its role in electrocatalysis," *Electrochimica Acta*, vol. 39, no. 11-12, pp. 1841–1848, 1994.

[76] P. R. Nair and M. A. Alam, "Dimensionally frustrated diffusion towards fractal adsorbers," *Phys Rev Lett*, vol. 99, no. 25, p. 256101, 2007. [Online]. Available: http://www.ncbi.nlm.nih.gov/pubmed/18233533

[77] R. A. Alberty and G. G. Hammes, "Application of the theory of diffusion-controlled reactions to enzyme kinetics," *The Journal of Physical Chemistry*, vol. 62, no. 2, pp. 154–159, 1958.

[78] P. W. Atkins, *Physical chemistry*. Oxford; Melbourne; Tokyo: Oxford University Press, 1998.

[79] X. Cheng, J. Zhang, H. Chang, L. Luo, F. Nie, and X. Feng, "High performance cu/cu 2 o nanohybrid electrocatalyst for nonenzymatic glucose detection," *Journal of Materials Chemistry B*, vol. 4, no. 27, pp. 4652–4656, 2016.

[80] P. R. Nair and M. A. Alam, "Performance limits of nanobiosensors," *Applied Physics Letters*, vol. 88, no. 23, p. 233120, 2006. [Online]. Available: ⟨GotoISI⟩://WOS:000238914500073

[81] J. Jackson, *Classical electrodynamics*. Wiley, 1975. [Online]. Available: https://books.google.com/books?id=_7rvAAAAMAAJ

[82] S. Y. Tee, C. P. Teng, and E. Ye, "Metal nanostructures for non-enzymatic glucose sensing," *Materials Science and Engineering: C*, vol. 70, pp. 1018–1030, 2017.

[83] S. Y. Tee, E. Ye, P. H. Pan, C. J. J. Lee, H. K. Hui, S.-Y. Zhang, L. D. Koh, Z. Dong, and M.-Y. Han, "Fabrication of bimetallic cu/au nanotubes and their sensitive, selective, reproducible and reusable electrochemical sensing of glucose," *Nanoscale*, vol. 7, no. 25, pp. 11 190–11 198, 2015.

[84] D. Rathod, C. Dickinson, D. Egan, and E. Dempsey, "Platinum nanoparticle decoration of carbon materials with applications in non-enzymatic glucose sensing," *Sensors and Actuators B: Chemical*, vol. 143, no. 2, pp. 547–554, 2010.

[85] A. Weremfo, S. T. C. Fong, A. Khan, D. B. Hibbert, and C. Zhao, "Electrochemically roughened nanoporous platinum electrodes for non-enzymatic glucose sensors," *Electrochimica Acta*, vol. 231, pp. 20–26, 2017.

[86] J. C. Claussen, J. B. Hengenius, M. M. Wickner, T. S. Fisher, D. M. Umulis, and D. M. Porterfield, "Effects of carbon nanotube-tethered nanosphere density on amperometric biosensing: simulation and experiment," *The Journal of Physical Chemistry C*, vol. 115, no. 43, pp. 20 896–20 904, 2011.

[87] J. C. Claussen, A. Kumar, D. B. Jaroch, M. H. Khawaja, A. B. Hibbard, D. M. Porterfield, and T. S. Fisher, "Nanostructuring platinum nanoparticles on multilayered graphene petal nanosheets for electrochemical biosensing," *Advanced Functional Materials*, vol. 22, no. 16, pp.

3399–3405, 2012. [Online]. Available: ⟨GotoISI⟩://WOS:000307566200005http://onlinelibrary.wiley.com/store/10.1002/adfm.201200551/asset/3399_ftp.pdf?v=1&t=j3ory7dc&s=1d1de638f7c47d46c33e1b66c858d7ea67b8335c

[88] W. Wu, J. Shen, Y. Li, H. Zhu, P. Banerjee, and S. Zhou, "Specific glucose-to-spr signal transduction at physiological ph by molecularly imprinted responsive hybrid microgels," *Biomaterials*, vol. 33, no. 29, pp. 7115–7125, 2012.

[89] Y. Li, Y. Yuan, D. Gong, W. Hu, and M. Yang, "A spr glucose sensor based on immobilized glucose oxidases and silica mesocellular foams," *IEEE Sensors Journal*, vol. 18, no. 6, pp. 2229–2235, 2018.

[90] R. Badugu, J. R. Lakowicz, and C. D. Geddes, "Ophthalmic glucose monitoring using disposable contact lenses—a review," *Journal of fluorescence*, vol. 14, no. 5, pp. 617–633, 2004.

[91] C. E. Ferrante do Amaral and B. Wolf, "Current development in non-invasive glucose monitoring," *Medical Engineering Physics*, vol. 30, no. 5, pp. 541–549, 2008. [Online]. Available: http://www.sciencedirect.com/science/article/pii/S1350453307001178

[92] M. C. Moreno-Bondi, O. S. Wolfbeis, M. J. Leiner, and B. P. Schaffar, "Oxygen optrode for use in a fiber-optic glucose biosensor," *Analytical Chemistry*, vol. 62, no. 21, pp. 2377–2380, 1990.

[93] R. X. D. C. H. G. L. H. I. K. C. L. L. L. J. R. K. Fox, L.A.; Beck, "Variation of interstitial glucose measurements assessed by continuous glucose monitors in healthy, nondiabetic individuals," *Diabetes Care*, vol. 33, no. 6, pp. 1297–1299, 2010. [Online]. Available: http://care.diabetesjournals.org/content/diacare/33/6/1297.full.pdf

[94] P. Makaram, D. Owens, and J. Aceros, "Trends in nanomaterial-based non-invasive diabetes sensing technologies," *Diagnostics*, vol. 4, no. 2, pp. 27–46, 2014.

[95] H. Lee, C. Song, Y. S. Hong, M. S. Kim, H. R. Cho, T. Kang, K. Shin, S. H. Choi, T. Hyeon, and D.-H. Kim, "Wearable/disposable sweat-based glucose monitoring device with multistage transdermal drug delivery module," *Science Advances*, vol. 3, no. 3, 2017. [Online]. Available: http://advances.sciencemag.org/content/advances/3/3/e1601314.full.pdf

[96] S. Gupta, S. V. Sandhu, H. Bansal, and D. Sharma, "Comparison of salivary and serum glucose levels in diabetic patients," *Journal of diabetes science and technology*, vol. 9, no. 1, pp. 91–96, 2014.

[97] R. Badugu, J. R. Lakowicz, and C. D. Geddes, "Fluorescence sensors for monosaccharides based on the 6-methylquinolinium nucleus and boronic acid moiety: potential application to ophthalmic diagnostics," *Talanta*, vol. 65, no. 3, pp. 762–768, 2005.

[98] X. Yang, Y. Yuan, Z. Dai, F. Liu, and J. Huang, "Optical property and adsorption isotherm models of glucose sensitive membrane based on prism spr sensor," *Sensors and Actuators B: Chemical*, vol. 237, pp. 150–158, 2016.

[99] W. Gao, S. Emaminejad, H. Y. Nyein, S. Challa, K. Chen, A. Peck, H. M. Fahad, H. Ota, H. Shiraki, D. Kiriya, D. H. Lien, G. A. Brooks, R. W. Davis, and A. Javey, "Fully integrated wearable sensor arrays for multiplexed in situ perspiration analysis," *Nature*, vol. 529, no. 7587, pp. 509–14, 2016. [Online]. Available: http://www.ncbi.nlm.nih.gov/pubmed/26819044

[100] J. Heikenfeld, A. Jajack, B. Feldman, S. W. Granger, S. Gaitonde, G. Begtrup, and B. A. Katchman, "Accessing analytes in biofluids for peripheral biochemical monitoring," *Nature biotechnology*, p. 1, 2019.

[101] E. Song, Y. K. Lee, R. Li, J. Li, X. Jin, K. J. Yu, Z. Xie, H. Fang, Y. Zhong, and H. Du, "Transferred, ultrathin oxide bilayers as biofluid barriers for flexible electronic implants," *Advanced Functional Materials*, 2017.

[102] J. Zhao, H. Guo, J. Li, A. J. Bandodkar, and J. A. Rogers, "Body-interfaced chemical sensors for noninvasive monitoring and analysis of biofluids," *Trends in Chemistry*, 2019.

[103] 2009.

[104] M. Zhou, N. Zhou, F. Kuralay, J. R. Windmiller, S. Parkhomovsky, G. Valdés-Ramírez, E. Katz, and J. Wang, "A self-powered "sense-act-treat" system that is based on a biofuel cell and controlled by boolean logic," *Angewandte Chemie International Edition*, vol. 51, no. 11, pp. 2686–2689, 2012.

[105] A. J. Bandodkar, J.-M. You, N.-H. Kim, Y. Gu, R. Kumar, A. V. Mohan, J. Kurniawan, S. Imani, T. Nakagawa, and B. Parish, "Soft, stretchable, high power density electronic skin-based biofuel cells for scavenging energy from human sweat," *Energy Environmental Science*, vol. 10, no. 7, pp. 1581–1589, 2017.

[106] D. P. Hickey, R. C. Reid, R. D. Milton, and S. D. Minteer, "A self-powered amperometric lactate biosensor based on lactate oxidase immobilized in dimethylferrocene-modified lpei," *Biosensors and Bioelectronics*, vol. 77, pp. 26–31, 2016.

[107] W. Jia, G. Valdés-Ramírez, A. J. Bandodkar, J. R. Windmiller, and J. Wang, "Epidermal biofuel cells: energy harvesting from human perspiration," *Angewandte Chemie International Edition*, vol. 52, no. 28, pp. 7233–7236, 2013. [Online]. Available: https://www.ncbi.nlm.nih.gov/pubmed/23729381

[108] X. Jin and M. Alam, "Generalized modeling framework of metal oxide-based non-enzymatic glucose sensor: concepts, methods, and challenges," *IEEE Transactions on Biomedical Engineering*, 2019. [Online]. Available: https://www.ncbi.nlm.nih.gov/pubmed/31150330

[109] P. Cinquin, C. Gondran, F. Giroud, S. Mazabrard, A. Pellissier, F. Boucher, J.-P. Alcaraz, K. Gorgy, F. Lenouvel, and S. Mathé, "A glucose biofuel cell implanted in rats," *PloS one*, vol. 5, no. 5, p. e10476, 2010.

[110] M. Cooney, V. Svoboda, C. Lau, G. Martin, and S. D. Minteer, "Enzyme catalysed biofuel cells," *Energy Environmental Science*, vol. 1, no. 3, pp. 320–337, 2008.

[111] A. Fraiwan, S. Mukherjee, S. Sundermier, H.-S. Lee, and S. Choi, "A paper-based microbial fuel cell: Instant battery for disposable diagnostic devices," *Biosensors and bioelectronics*, vol. 49, pp. 410–414, 2013.

[112] L. Halámková, J. Halámek, V. Bocharova, A. Szczupak, L. Alfonta, and E. Katz, "Implanted biofuel cell operating in a living snail," *Journal of the American Chemical Society*, vol. 134, no. 11, pp. 5040–5043, 2012.

[113] S. D. Minteer, B. Y. Liaw, and M. J. Cooney, "Enzyme-based biofuel cells," *Current opinion in biotechnology*, vol. 18, no. 3, pp. 228–234, 2007.

[114] A. Zebda, C. Gondran, A. Le Goff, M. Holzinger, P. Cinquin, and S. Cosnier, "Mediatorless high-power glucose biofuel cells based on compressed carbon nanotube-enzyme electrodes," *Nature communications*, vol. 2, p. 370, 2011.

[115] D.-H. Kim, N. Lu, R. Ma, Y.-S. Kim, R.-H. Kim, S. Wang, J. Wu, S. M. Won, H. Tao, and A. Islam, "Epidermal electronics," *science*, vol. 333, no. 6044, pp. 838–843, 2011. [Online]. Available: https://www.ncbi.nlm.nih.gov/pubmed/21836009

[116] K. Mitsubayashi and T. Arakawa, "Cavitas sensors: Contact lens type sensors mouthguard sensors," *Electroanalysis*, vol. 28, no. 6, pp. 1170–1187, 2016.

[117] J. Park, J. Kim, S.-Y. Kim, W. H. Cheong, J. Jang, Y.-G. Park, K. Na, Y.-T. Kim, J. H. Heo, and C. Y. Lee, "Soft, smart contact lenses with integrations of wireless circuits, glucose sensors, and displays," *Science advances*, vol. 4, no. 1, p. eaap9841, 2018.

[118] H. Yao, Y. Liao, A. Lingley, A. Afanasiev, I. Lähdesmäki, B. Otis, and B. Parviz, "A contact lens with integrated telecommunication circuit and sensors for wireless and continuous tear glucose monitoring," *Journal of Micromechanics and Microengineering*, vol. 22, no. 7, p. 075007, 2012.

[119] X. Chen, L. Yin, J. Lv, A. J. Gross, M. Le, N. G. Gutierrez, Y. Li, I. Jeerapan, F. Giroud, and A. Berezovska, "Stretchable and flexible buckypaper-based lactate biofuel cell for wearable electronics," *Advanced Functional Materials*.

[120] I. Jeerapan, J. R. Sempionatto, and J. Wang, "On-body bioelectronics: Wearable biofuel cells for bioenergy harvesting and self-powered biosensing," *Advanced Functional Materials*, 2019.

[121] A. F. Yeknami, X. Wang, I. Jeerapan, S. Imani, A. Nikoofard, J. Wang, and P. P. Mercier, "A 0.3-v cmos biofuel-cell-powered wireless glucose/lactate biosensing system," *IEEE Journal of Solid-State Circuits*, vol. 53, no. 11, pp. 3126–3139, 2018.

[122] S. Choi, "Microscale microbial fuel cells: Advances and challenges," *Biosensors and Bioelectronics*, vol. 69, pp. 8–25, 2015.

[123] S. Cosnier, A. J. Gross, F. Giroud, and M. Holzinger, "Beyond the hype surrounding biofuel cells: What's the future of enzymatic fuel cells?" *Current Opinion in Electrochemistry*, vol. 12, pp. 148–155, 2018.

[124] R. A. Escalona-Villalpando, E. Ortiz-Ortega, J. P. Bocanegra-Ugalde, S. D. Minteer, L. G. Arriaga, and J. Ledesma-García, "A complete tattoo-based wireless biofuel cell using lactate directly from sweat as fuel," *Journal of Physics: Conference Series*, vol. 1407, p. 012028, 2019. [Online]. Available: http://dx.doi.org/10.1088/1742-6596/1407/1/012028

[125] Y. Song, V. Penmatsa, and C. Wang, "Modeling and simulation of enzymatic biofuel cells with three-dimensional microelectrodes," *Energies*, vol. 7, no. 7, pp. 4694–4709, 2014. [Online]. Available: ⟨GotoISI⟩://WOS:000339989200037

[126] D.-S. Chan, D.-J. Dai, and H.-S. Wu, "Dynamic modeling of anode function in enzyme-based biofuel cells using high mediator concentration," *Energies*, vol. 5, no. 7, pp. 2524–2544, 2012.

[127] M. Falk, V. Andoralov, M. Silow, M. D. Toscano, and S. Shleev, "Miniature biofuel cell as a potential power source for glucose-sensing contact lenses," *Analytical chemistry*, vol. 85, no. 13, pp. 6342–6348, 2013.

[128] X. Xiao, T. Siepenkoetter, P. O. Conghaile, D. Leech, and E. Magner, "Nanoporous gold-based biofuel cells on contact lenses," *ACS applied materials interfaces*, vol. 10, no. 8, pp. 7107–7116, 2018.

[129] R. Asadpour, X. Sun, and M. A. Alam, "Electrical signatures of corrosion and solder bond failure in c-si solar cells and modules," *IEEE Journal of Photovoltaics*, vol. 9, no. 3, pp. 759–767, 2019.

[130] M. Tahir Patel, M. Ryyan Khan, and M. A. Alam, "Thermodynamic limit of solar to fuel conversion for generalized photovoltaic-electrochemical system," *arXiv preprint arXiv:1707.03970*, 2017.

[131] I. Jeerapan, J. R. Sempionatto, J.-M. You, and J. Wang, "Enzymatic glucose/oxygen biofuel cells: Use of oxygen-rich cathodes for operation under severe oxygen-deficit conditions," *Biosensors and Bioelectronics*, vol. 122, pp. 284–289, 2018. [Online]. Available: ⟨GotoISI⟩://WOS:000448493800034

[132] Y. Yu, M. Xu, L. Bai, L. Han, and S. Dong, "Recoverable hybrid enzymatic biofuel cell with molecular oxygen-independence," *Biosensors and Bioelectronics*, vol. 75, pp. 23–27, 2016. [Online]. Available: https://www.ncbi.nlm.nih.gov/pubmed/26283586

[133] J. Hu, A. Stein, and P. Bühlmann, "Rational design of all-solid-state ion-selective electrodes and reference electrodes," *TrAC Trends in Analytical Chemistry*, vol. 76, pp. 102–114, 2016.

[134] R. Cattrall and H. Freiser, "Coated wire ion-selective electrodes," *Analytical Chemistry*, vol. 43, no. 13, pp. 1905–1906, 1971.

[135] W. E. Morf, M. Badertscher, T. Zwickl, N. F. de Rooij, and E. Pretsch, "Effects of ion transport on the potential response of ionophore-based membrane electrodes: a theoretical approach," *The Journal of Physical Chemistry B*, vol. 103, no. 51, pp. 11 346–11 356, 1999.

[136] N. Kanopoulos, N. Vasanthavada, and R. L. Baker, "Design of an image edge detection filter using the sobel operator," *IEEE Journal of solid-state circuits*, vol. 23, no. 2, pp. 358–367, 1988.

[137] T. Ahonen, A. Hadid, and M. Pietikainen, "Face description with local binary patterns: Application to face recognition," *IEEE transactions on pattern analysis and machine intelligence*, vol. 28, no. 12, pp. 2037–2041, 2006.

[138] H. Drucker, C. J. Burges, L. Kaufman, A. J. Smola, and V. Vapnik, "Support vector regression machines," in *Advances in neural information processing systems*, 1997, pp. 155–161.

[139] E. Sazonov and M. R. Neuman, *Wearable Sensors: Fundamentals, implementation and applications*. Elsevier, 2014.

[140] J. P. Rojas, G. A. T. Sevilla, and M. M. Hussain, "Can we build a truly high performance computer which is flexible and transparent?" *Scientific reports*, vol. 3, p. 2609, 2013.

[141] J. P. Rojas, G. A. Torres Sevilla, M. T. Ghoneim, S. B. Inayat, S. M. Ahmed, A. M. Hussain, and M. M. Hussain, "Transformational silicon electronics," *ACS nano*, vol. 8, no. 2, pp. 1468–1474, 2014. [Online]. Available: http://pubs.acs.org/doi/pdfplus/10.1021/nn405475k

[142] M. Kaltenbrunner, T. Sekitani, J. Reeder, T. Yokota, K. Kuribara, T. Tokuhara, M. Drack, R. Schwödiauer, I. Graz, and S. Bauer-Gogonea, "An ultra-lightweight design for imperceptible plastic electronics," *Nature*, vol. 499, no. 7459, pp. 458–463, 2013. [Online]. Available: https://www.ncbi.nlm.nih.gov/pubmed/23887430

[143] A. Koh, D. Kang, Y. Xue, S. Lee, R. M. Pielak, J. Kim, T. Hwang, S. Min, A. Banks, and P. Bastien, "A soft, wearable microfluidic device for the capture, storage, and colorimetric sensing of sweat," *Science Translational Medicine*, vol. 8, no. 366, pp. 366ra165–366ra165, 2016. [Online]. Available: http://stm.sciencemag.org/content/scitransmed/8/366/366ra165.full.pdf

[144] H. Nam, J. S. Yoon, H. Izuoka, B.-R. Oh, K. Kurabayashi, W. Wan, and X. Liang, "Nanofluidic flow assisted assembly of dispersed plasmonic nanostructures into shallow nanochannel sensors," *Journal of Vacuum Science Technology B, Nanotechnology and Microelectronics: Materials, Processing, Measurement, and Phenomena*, vol. 34, no. 6, p. 06KM04, 2016. [Online]. Available: ⟨GotoISI⟩://WOS:000389530000049

[145] K. K. Fu, Z. Wang, J. Dai, M. Carter, and L. Hu, "Transient electronics: materials and devices," *Chemistry of Materials*, vol. 28, no. 11, pp. 3527–3539, 2016. [Online]. Available: ⟨GotoISI⟩://WOS:000378016400002

[146] S.-K. Kang, R. K. Murphy, S.-W. Hwang, S. M. Lee, D. V. Harburg, N. A. Krueger, J. Shin, P. Gamble, H. Cheng, and S. Yu, "Bioresorbable silicon electronic sensors for the brain," *Nature*, vol. 530, no. 7588, pp. 71–76, 2016. [Online]. Available: http://www.nature.com/nature/journal/v530/n7588/pdf/nature16492.pdf

[147] D.-H. Kim, J. Viventi, J. J. Amsden, J. Xiao, L. Vigeland, Y.-S. Kim, J. A. Blanco, B. Panilaitis, E. S. Frechette, and D. Contreras, "Dissolvable films of silk fibroin for ultrathin conformal bio-integrated electronics," *Nature materials*, vol. 9, no. 6, pp. 511–517, 2010. [Online]. Available: http://www.nature.com/nmat/journal/v9/n6/pdf/nmat2745.pdf

[148] T. Sekitani, Y. Noguchi, K. Hata, T. Fukushima, T. Aida, and T. Someya, "A rubberlike stretchable active matrix using elastic conductors," *Science*, vol. 321, no. 5895, pp. 1468–1472, 2008. [Online]. Available: http://science.sciencemag.org/content/sci/321/5895/1468.full.pdf

[149] P. Bergveld, "The impact of mosfet-based sensors," *Sensors and Actuators*, vol. 8, no. 2, pp. 109–127, 1985. [Online]. Available: ⟨GotoISI⟩://WOS:A1985A114000003

[150] J. Go and M. Alam, "Effect of fluid gate on the electrostatics of isfet-based ph sensors," in *Micro/Nano Symposium (UGIM), 2010 18th Biennial University/Government/Industry*. IEEE, Conference Proceedings, pp. 1–3.

[151] T. Matsuo and M. Esashi, "Methods of isfet fabrication," *Sensors and Actuators*, vol. 1, no. 1, pp. 77–96, 1981. [Online]. Available: ⟨GotoISI⟩://WOS:A1981LY43200006

[152] A. Jain and M. A. Alam, "Intrinsic low pass filtering improves signal-to-noise ratio in critical-point flexure biosensors," *Applied Physics Letters*, vol. 105, no. 8, p. 084106, 2014. [Online]. Available: ⟨GotoISI⟩://WOS:000342753500120http://aip.scitation.org/doi/pdf/10.1063/1.4893597

[153] A. Jain, P. R. Nair, and M. A. Alam, "Flexure-fet biosensor to break the fundamental sensitivity limits of nanobiosensors using nonlinear electromechanical coupling," *Proceedings of the National Academy of Sciences*, vol. 109, no. 24, pp. 9304–9308, 2012. [Online]. Available: ⟨GotoISI⟩://WOS:000305511300027https://www.ncbi.nlm.nih.gov/pmc/articles/PMC3386129/pdf/pnas.1203749109.pdf

[154] G. Schwartz, B. C.-K. Tee, J. Mei, A. L. Appleton, D. H. Kim, H. Wang, and Z. Bao, "Flexible polymer transistors with high pressure sensitivity for application in electronic skin and health monitoring," *Nature communications*, vol. 4, p. 1859, 2013. [Online]. Available: https://www.ncbi.nlm.nih.gov/pubmed/23673644

[155] H. Fang, K. J. Yu, C. Gloschat, Z. Yang, E. Song, C.-H. Chiang, J. Zhao, S. M. Won, S. Xu, and M. Trumpis, "Capacitively coupled arrays of multiplexed flexible silicon transistors for long-term cardiac electrophysiology," *Nature Biomedical Engineering*, vol. 1, p. 0038, 2017.

[156] H. Fang, J. Zhao, K. J. Yu, E. Song, A. B. Farimani, C.-H. Chiang, X. Jin, Y. Xue, D. Xu, and W. Du, "Ultrathin, transferred layers of thermally grown silicon dioxide as biofluid barriers for biointegrated flexible electronic systems," *Proceedings of the National Academy of Sciences*, vol. 113, no. 42, pp. 11 682–11 687, 2016. [Online]. Available: ⟨GotoISI⟩://WOS:000385610400041

[157] E. Song, H. Fang, X. Jin, J. Zhao, C. Jiang, K. J. Yu, Y. Zhong, D. Xu, J. Li, and G. Fang, "Thin, transferred layers of silicon dioxide and silicon nitride as water and ion barriers for implantable flexible electronic systems," *Advanced Electronic Materials*, 2017.

[158] R. Swanson, M. Cudzinovic, D. DeCeuster, V. Desai, J. Jürgens, N. Kaminar, W. Mulligan, L. Barbarosa, D. Rose, and D. Smith, "The surface polarization effect in high-efficiency silicon solar cells," in *15th PVSEC*. Shanghai, China, Conference Proceedings.

[159] O. Kraft, J. Sanchez, M. Bauer, and E. Arzt, "Quantitative analysis of electromigration damage in al-based conductor lines," *Journal of materials research*, vol. 12, no. 8, pp. 2027–2037, 1997. [Online]. Available: ⟨GotoISI⟩://WOS:A1997XQ27800010

[160] A. Many and G. Rakavy, "Theory of transient space-charge-limited currents in solids in the presence of trapping," *Physical Review*, vol. 126, no. 6, p. 1980, 1962.

[161] E. Yon, W. Ko, and A. Kuper, "Sodium distribution in thermal oxide on silicon by radiochemical and mos analysis," *IEEE Transactions on Electron Devices*, vol. Ed13, no. 2, pp. 276–280, 1966. [Online]. Available: ⟨GotoISI⟩://WOS:A19667492800007http://ieeexplore.ieee.org/ielx5/16/31618/01474270.pdf?tp=&arnumber=1474270&isnumber=31618

[162] T. Burges, "Thermal diffusion of sodium in silicon nitride shielded silicon dioxide film," *Journal Electrochem Soc*, vol. 116, no. 7, 1969.

[163] V. M. Korol, "Sodium-ion implantation into silicon," *Physica Status Solidi a-Applied Research*, vol. 110, no. 1, pp. 9–34, 1988. [Online]. Available: ⟨GotoISI⟩://WOS:A1988R880800001http://onlinelibrary.wiley.com/store/10.1002/pssa.2211100102/asset/2211100102_ftp.pdf?v=1&t=j0bbehqd&s=950651aad88947b67d12e137a33ed6791d1a542b

[164] H. A. Schaeffer, J. Mecha, and J. Steinmann, "Mobility of sodium-ions in silica glass of different oh content," *Journal of the American Ceramic Society*, vol. 62, no. 7-8, pp. 343–346, 1979. [Online]. Available: ⟨GotoISI⟩://WOS:A1979HG27200007http://onlinelibrary.wiley.com/store/10.1111/j.1151-2916.1979.tb19074.x/asset/j.1151-2916.1979.tb19074.x.pdf?v=1&t=j0bbbtqh&s=f34b3fd3bb049eec0d2e08cea983a421b33eafe9

[165] P. R. Nair and M. A. Alam, "Screening-limited response of nanobiosensors," *Nano letters*, vol. 8, no. 5, pp. 1281–1285, 2008. [Online]. Available: http://pubs.acs.org/doi/pdfplus/10.1021/nl072593i

[166] A. Grinberg, S. Luryi, M. Pinto, and N. Schryer, "Space-charge-limited current in a film," *IEEE Transactions on Electron Devices*, vol. 36, no. 6, pp. 1162–1170, 1989. [Online]. Available: ⟨GotoISI⟩://WOS:A1989U631000023

[167] N. F. Mott and R. W. Gurney, "Electronic processes in ionic crystals," 1940.

[168] R. Pierret, *Semiconductor Device Fundamentals*. Addison-Wesley, 1996. [Online]. Available: https://books.google.com/books?id=GMZFHwAACAAJ

[169] Y. Taur and T. Ning, *Fundamentals of Modern VLSI Devices*. Cambridge University Press, 2009. [Online]. Available: https://books.google.com/books?id=Aw5jPgAACAAJ

[170] K. J. Laidler, "The development of the arrhenius equation," *J. Chem. Educ*, vol. 61, no. 6, p. 494, 1984. [Online]. Available: ⟨GotoISI⟩://WOS:A1984SX06600005

[171] A. Pal, D. Goswami, H. E. Cuellar, B. Castro, S. Kuang, and R. V. Martinez, "Early detection and monitoring of chronic wounds using low-cost, omniphobic paper-based smart bandages," *Biosensors and Bioelectronics*, vol. 117, pp. 696–705, 2018.

[172] K. Pardee, A. A. Green, T. Ferrante, D. E. Cameron, A. DaleyKeyser, P. Yin, and J. J. Collins, "Paper-based synthetic gene networks," *Cell*, vol. 159, no. 4, pp. 940–954, 2014.

[173] W. L. Then and G. Garnier, "Paper diagnostics in biomedicine," *Reviews in Analytical Chemistry*, vol. 32, no. 4, pp. 269–294, 2013.

[174] X. Strakosas, M. Bongo, and R. M. Owens, "The organic electrochemical transistor for biological applications," *Journal of Applied Polymer Science*, vol. 132, no. 15, 2015.

[175] D. R. Lide, *CRC handbook of chemistry and physics*. CRC press, 2004, vol. 85.

[176] R. F. Fox, T. P. Hill, and R. M. Fox, "Macroscope: An exact value for avogadro's number," *American Scientist*, vol. 95, no. 2, pp. 104–107, 2007. [Online]. Available: http://www.jstor.org/stable/27858920

[177] K. Karmali, A. Karmali, A. Teixeira, and M. J. M. Curto, "Assay for glucose oxidase from aspergillus niger and penicillium amagasakiense by fourier transform infrared spectroscopy," *Analytical Biochemistry*, vol. 333, no. 2, pp. 320–327, 2004. [Online]. Available: http://www.sciencedirect.com/science/article/pii/S0003269704005421

[178] D. Rando, G.-W. Kohring, and F. Giffhorn, "Production, purification and characterization of glucose oxidase from a newly isolated strain of penicillium pinophilum," *Applied Microbiology and Biotechnology*, vol. 48, no. 1, pp. 34–40, 1997. [Online]. Available: http://dx.doi.org/10.1007/s002530051011

APPENDIX

A. SUMMARY OF ANALYTICAL EQUATIONS AND FITTING PARAMETERS

A.1 Chapter 2: Nanoparticle-based Amperometric Glucose Biosensors

Table A.1.: List of physical constants for Nanoparticle-based Amperometric Glucose Biosensors

Symbol	Definition	Value	Units	Reference
D_G	Glucose diffusion coefficient	6×10^{-10}	m^2/s	[175]
N_A	Avogadro constant	6.02×10^{23}	$1/mol$	[176]
k_f	Forward reaction constant	16000	$m^3/mol/s$	[49]
k_c	Catalytic rate constant	1350	$1/s$	[177]
E_0	Surface enzyme(GO_x) density	4.38×10^{-9}	mol/m^2	[39]
r_{Pt}	Average Pt nanosphere radius	75	nm	[39]
r_{ez}	Average Enzyme radius	4	nm	[178]
t_{ez}	Average Enzyme thickness	3	nm	[178]
H	Height of unit cell	2	μm	[39]

Table A.2.: List of fitting parameters for match of analytical expressions to experimental data for Nanoparticle-based Amperometric Glucose Biosensors

Fig. Plot	Fitting Parameters
Fig.2.4 (a), CNT NP sensor current response	$K_m = 24.9 mol/m^2$, $M = 2.67 \times 10^7$, $d = 4r_{Pt}$, $W_c = 6r_{Pt}$
Fig.2.4(b),MPGN NP sensor current response	$K_m = 50 mol/m^2$, $iNP : d_{0.625mA} = 1.2r_{Pt}, d_{1.25mA} = 0.5r_{Pt}$. cNP: $W_c = 6r_{Pt}$
Fig.2.6, Current response and sensitivity with varying r_{Pt}	$K_m = 24.9 mol/m^2$, $M = 2.67 \times 10^7$, $d = 4r_{Pt}$

A.2 Chapter 3: Metal oxide-based non-enzymatic glucose sensor

Table A.3.: List of analytical equations for metal oxide-based non-enzymatic glucose sensor

Description	Equation
The normalized form of Eq. 3.3 to 3.7	$\frac{N^*_{III}\cdot G^*_s}{(1-G^*_S)} = \gamma$, (Equating Eq.3.4 and Eq. 3.7 in the steady state) $N^*_{III}G^*_S - (\alpha N^*_{II} - \beta N^*_{III}) = 0$ (Eq.3.5) $N^*_{III} + N^*_{II} = 1$ (Eq. 3.6)
The surface density of metal oxide in the reductive state (exactsolution)	$N^*_{III} = \frac{(-(\gamma(\alpha+\beta)+\gamma-\alpha)+\sqrt{(\gamma(\alpha+\beta)+\gamma-\alpha)^2+4\alpha\gamma\cdot(\alpha+\beta)}}{2(\alpha+\beta)}$
Glucose concentration near the NW electrode arrays	$G_s = \frac{C_D\cdot G_0}{(A_e\cdot k_F\cdot(N_0-N_{II})+C_D)}$
Diffusion capacitance of NW electrode arrays with metal oxide deposited on the surface	$C_{D,NW} = \frac{2\pi D\cdot l}{\log\left(\frac{\sinh(\frac{2\pi(\sqrt{2Dt}+r_{NW})}{W_C})}{\sinh(\frac{\pi r_{NW}}{W_C})}\right)} + \frac{\pi l}{2N_0\cdot r_M}$ where r_M is the average radius of CuO NPs. $\mathrm{A_e} = 2\pi r_{NW} l$ (per unit cell)
Butler-Volmer equation	$k_R = k_0 \cdot exp(-\alpha f(E - E_0))$ $k'_R = k_0 \cdot exp((1-\alpha) f(E - E_0))$ where E is the voltage bias applied on the working electrode and k_0 is a prefactor determined by the property of Cu II and the pH of the electrolyte (the concentration of OH^- in Eq. 3.2).

Table A.4.: List of key fitting parameters for metal oxide-based non-enzymatic glucose sensor

Fig.	Key Calibration parameters					
	Deposition voltage /morphology	N_0 (mol/m^2)	k_F $(m^3/(s \cdot mol))$	k_R (s^{-1})	k'_R (s^{-1})	r_{NW} (μm)
3.3, A	400 mV 16 min	1.55×10^{-9}	76	300	30	50
	400 mV 30 min	2×10^{-9}	same	same	same	same
	450 mV 16 min	2.6×10^{-9}	same	same	same	same
	450 mV 30 min	2.7×10^{-9}	same	same	same	same
3.3, B	CuO, NP	3.2×10^{-9}	8	51	5	5
	CuO, NW	same	31	same	same	same
	CuO, NSs	same	75	same	same	same
3.3, C	CuO NW	6.8×10^{-10}	90	210	42	0.2
	CuO/ZnO NW	same	220	same	same	same
	CuO/ZnO HNC 10min	same	same	1600	320	same
	CuO/ZnO HNC 15min	1.2×10^{-9}	same	same	same	same
	CuO/ZnO HNC 20min	2×10^{-9}	same	same	same	same

A.3 Chapter 7: Stability of MOSFET-based Electronic Components in Wearable and Implantable Systems

Table A.5.: List of fitting parameters for MOSFET-based electronic components in wearable and implantable systems

Fig. Plot	Parameters
7.2 B to D	$D = 6.53 \times 10^{-21} m^2/s$, $T = 37°C$
7.3, B	$L = 20\mu m, W = 300\mu m, t_{ox} = 40nm, t_{Si} = 100nm, V_{ds} = 1V,$ $\mathrm{N}_{D,Source/Drain} = 10^{19} cm^{-3}$
7.3, C to D	$Q_{ch} = 7.8 \times 10^{8} m^{-3}$
7.3, E	$D = 6.53 \times 10^{-21} m^2/s, T = 37°C$
7.3, F	$D = 1.05 \times 10^{-19} m^2/s, r_{dis} = 90nm/day, T = 96°C$
7.4, B to F	$SiO_2 : D = 6.53 \times 10^{-21} m^2/s, T = 37°C$ $SiN_x : D = 4.94 \times 10^{-25} m^2/s, T = 37°C$
7.5	$D_0 = 2.29 \times 10^{-12} m^2/s, E_A = 7.43 \times 10^{-20} J$

B. NANOPARTICLE-BASED AMPEROMETRIC GLUCOSE BIOSENSORS: ISOLATED NP VS. CHAIN NP SYSTEMS

B.1 Numerical Simulation of isolated NP and chain NP systems

In order to validate the analytical formula developed in this paper, we simulate the isolated NP and chain NP systems numerically with the aid of COMSOL Multiphysics ®. Fig.B.1(a) and (b) compare the faradic current predicted by the analytical and the numerical in a single unit cell for both iNP and cNP cases. Specifically, we sweep G_0 from 10 mM to 60 mM and calculate the output current. It is satisfying to see that the analytical solution and numerical simulation solutions match very well, thereby validating the model developed in this paper.

B.2 A Comparison between Chain NP Electrode and Planar Electrode

To illustrate the claim that NP chains at very high density act like a planar electrode, we compare the responses of a cNP sensor and a planar sensor by using COMSOL simulation. As shown in the Fig.B.2 (a) and (b) below, the 2D unit cells of those two systems have the same width and height. Our goal would be to vary size of the NP (r_{pt}) with respect to the periodicity of the cell (W_c) to establish the transition density at which the Faradic current of a chain of a NP (I_{cNP}) is indistinguishable from that of a planar sensor (I_{planar}). The top surface has a glucose concentration of $G_0 = 50mM$ and the rest of the boundaries are reflective. We assume the glucose molecules are completely absorbed by the electrode, and then calculate the Faradic current by integrating the flux over the electrode surface. The ratio of the current is plotted in Fig.B.2 (c). The results show that the transition to planar response occurs

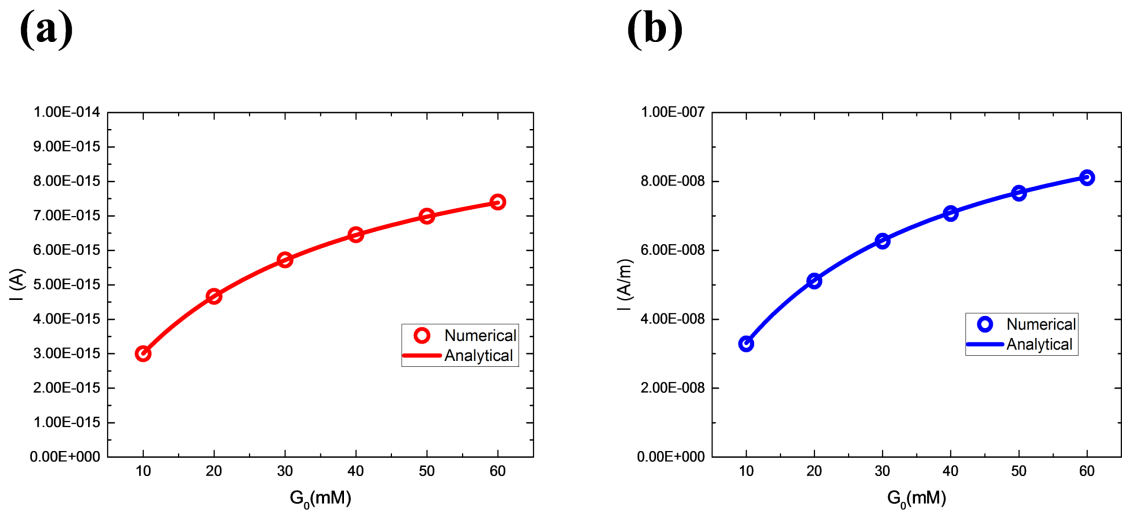

Fig. B.1.: A comparison between the analytical and numerical faradic response in a unit cell for (a) iNP and (b) cNP.

at $\frac{2\pi r_{pt}}{W_C} \geq 0.5$ as $\frac{I_{cNP}}{I_{planar}} > 90\%$. The surface of the chain of the NP, if unrolled, covers approximately half the periodicity.

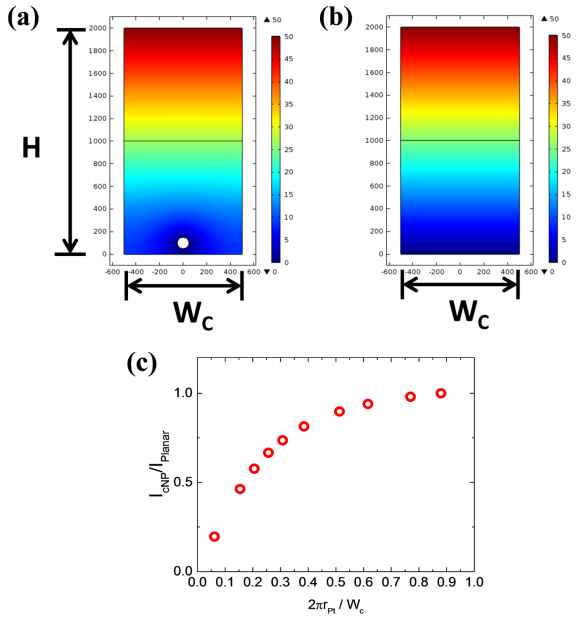

Fig. B.2.: A comparison of faradic response in a 2D unit cell between (a) cNP and (b) Planar electrode. (c) Plot of normalized current as a function of $2\pi r_{pt}/W_c$.

B.3 Additional Discussion on Parametric Sensitivity of iNP and cNP sensors

(i) For the cNP case, let us calculate the sensitively of the Faradic current on the average radius of the NPs, r_{pt} (without changing the total length l and inter-particle distance d). Fig.B.3 (a) below plots the current as a function of glucose concentration, with r_{pt} as a sweeping parameter. The sensitivity (dI/dG_0) at high concentration vs. r_{pt} is characterized by a slope of $\sim$1 (Fig.B.3 (b)), demonstrating that the current scales linearly with r_{Pt}, or more generally, with the effective surface area of the sensor.

(ii) For the iNP case, we may similarly calculate the sensitivity as a function of the radius of the NPs, while keeping the total surface area of all the NPs a constant. We find that the sensitivity increase slightly for small NP ($r_{pt} < 10^{-7}$), flattens out at the intermediate thicknesses, but then drops dramatically beyond a critical size (10^{-6} m in this example). The optimal point occurs at $r_{Pt} \sim 2 \times 10^{-7} m$. The initial

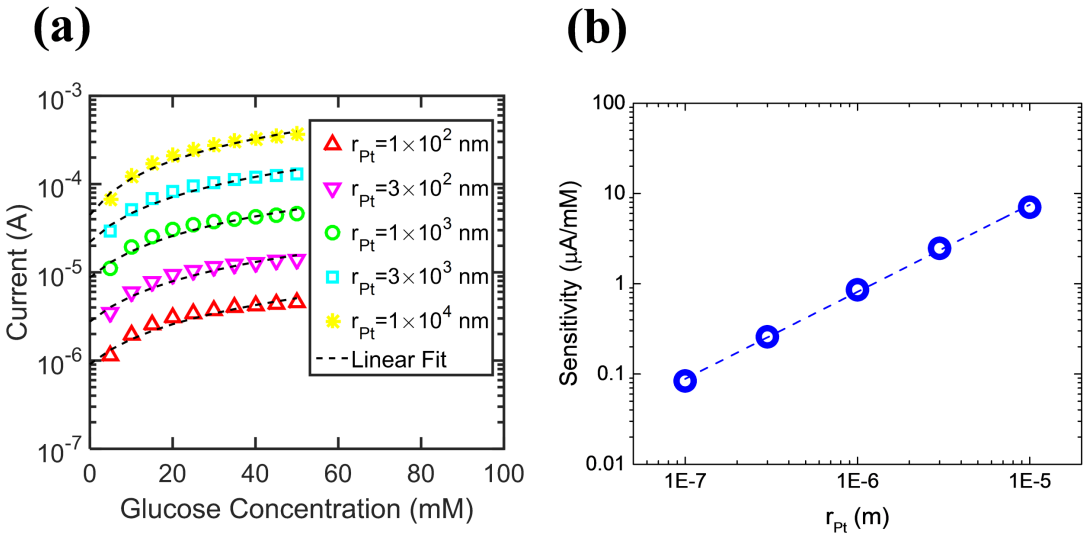

Fig. B.3.: Amperometric current response as a function of r_{Pt} ranging from $100nm$ to 10^4nm in cNP case. The total chain length l presumed a constant. The sensitivity in (b) is calculated from the slope of each fitted lines in (a). The slope of fitted line is 1 (in the log-log plot), indicating that the sensitivity depends linearly on the radius of NP.

increase is due to the H_2O_2 generation and recapture step dominates. As r_{Pt} increase, there's larger probability for the NP electrode to capture H_2O_2. However, when r_{Pt} become very large, the glucose diffusion and reaction steps begin to dominate current generation. Surface glucose concentration G_s decreases with increasing r_{Pt}, which in turn, reduces the output faradic response.

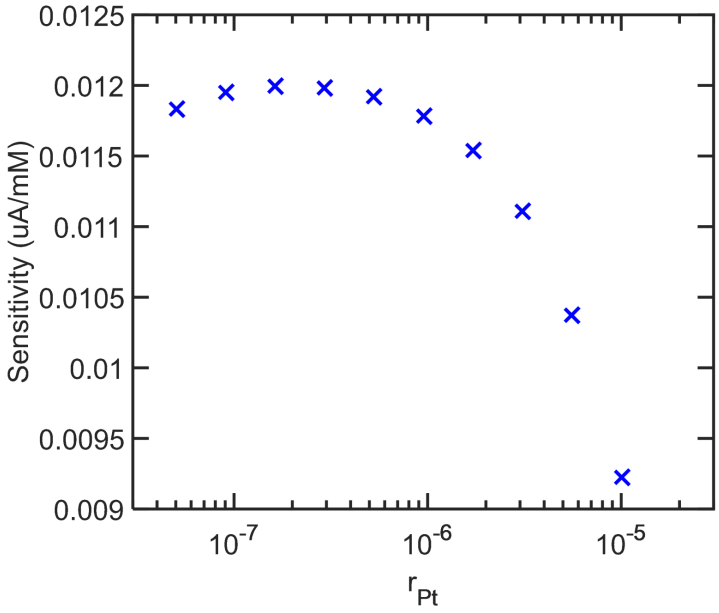

Fig. B.4.: Sensitivity as a function of r_{Pt} with constant total sensor surface area.

C. METHOD AND MATERIAL: R2R PRINTED THIN-FILM-BASED ISE NITRATE SENSOR

C.1 Printed conductive electrodes

Rolls of DuPont Teijin Films poly(ethylene terephthalate) (PET) film, grade ST-505, 0.005 inch thick x 6 inch wide x 500 foot long, were used as substrates. Semi-continuous, roll-to-roll screen printing was used to define conductive electrodes on the PET substrate. In the case of reference electrodes, DuPont 5880 silver/silver-chloride paste was used, and in the case of working electrodes, DuPont 5025 silver paste was used. A diagram of the screen-print pattern used to define electrodes is shown in Fig. C.1. Pastes were dried after printing by following the paste manufacturer's recommendations. The rolls of electrodes were subsequently coated with various coatings to enhance selectivity (in the case of working electrodes) or stability (in the case of reference electrodes).

C.2 Working electrodes

The silver electrodes were coated using the same Yasui Seiki-MIRWEC Mini-Labo Deluxe^{TM} coating machine and a similar slot die coating process. In this case, the 0.7 inch wide die was used to apply an ion selective coating aligned with one end of the electrode array. The material used for this coating comprised a solution of PVC, di-n-butylphthalate, and tetraoctylammonium bromide (TOA-Br) in tetrahydrofuran (THF). The ratio of PVC:di-n-butylphthalate:TOA-Br:THF was 15:30:1:X by weight, where X was between 135 and 160. This suspension was supplied to the slot die at a flow rate of 0.3 to 1.4 mL/min via a tapped hole on one side of the die that was connected to a syringe pump via flexible tubing. After the coating was applied, an

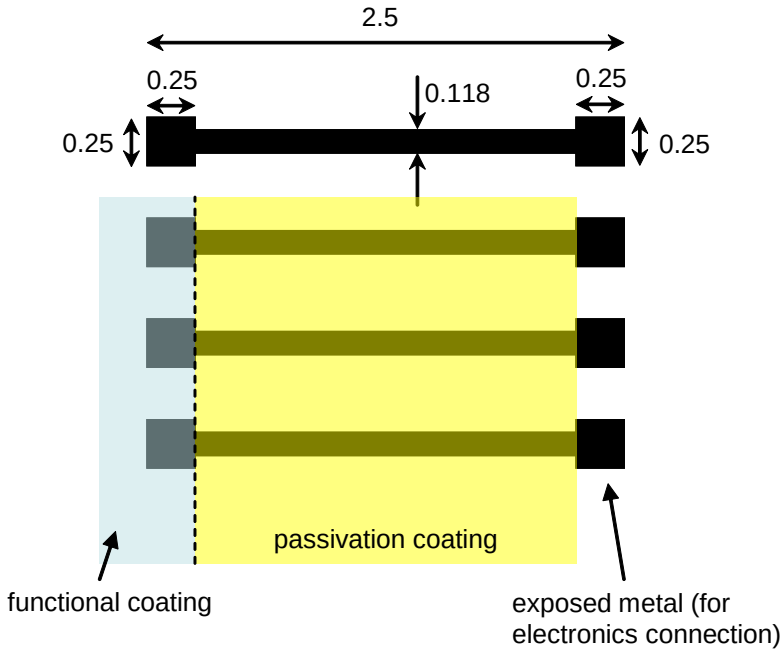

Fig. C.1.: The as-printed repeating electrode geometry is shown in black, with dimensions shown in inches on the top electrode. The passivation coating provides electrical insulation and protects the printed metal from exposure to water. The functional coating enhances selectivity (in the case of working electrodes) or stability (in the case of reference electrodes). Coatings are deposited on top of the printed and dried electrodes via a continuous, roll-to-roll slot-die coating method in which the machine direction is vertical in this diagram.

in-line 1 m long convection oven with air heated to 55°C flowing on top and bottom of the film was used to dry off the solvent.

The same material and process was used to apply the silicone passivation coating to the working electrodes as was used for the reference electrodes. After all coatings were completed, individual working and reference electrodes were cut from the respective rolls via scissors. The uncoated printed metal ends (see Fig. C.1) were used as connection points to electronic measurement systems.

C.3 Reference electrodes

The silver/silver chloride electrodes were coated via a continuous, roll-to-roll slot die coating method using a Yasui Seiki-MIRWEC Mini-Labo Deluxe^{TM} coating machine. While the printed PET film was unwound and rewound at a line speed of 100 mm/min, a slot die was placed at either 45° or 90° relative to the film as it passed over a flat, rigid platform. The aluminum slot die was custom designed and consisted of two flat faces that were set apart by an adjustable shim. The shim design defines the geometry of the opening of the slot die. All shims were 0.005 inch thick and had either 0.7 inch or 2 inch wide opening.

The 0.7 inch wide die was used to apply a stabilizing coating aligned with one end of the electrode array. The material used for this coating comprised potassium chloride particles suspended in a solution of poly(vinyl chloride) (PVC) in tetrahydrofuran (THF). The KCl particles were milled via mortar and pestle and passed through a series of sieves, the finest of which was 635 mesh (20 micrometer opening). The ratio of KCl:PVC:THF was 10:10:100 by weight. This suspension was supplied to the slot die at a flow rate of 0.6 to 1.0 mL/min via a tapped hole on one side of the die that was connected to a syringe pump via flexible tubing. After the coating was applied, an in-line 1 m long convection oven with air heated to 55°C flowing on top and bottom of the film was used to dry off the solvent.

After rewinding the film, the 2-inch wide die was used to apply a passivation coating, the purpose of which is to provide electrical insulation and to protect the printed metal from exposure to water. The material used for passivation was Silicone Solutions SS-6002S. It was supplied to the slot die at a flow rate of 1.5 mL/min via a tapped hole on one side of the die that was connected to a syringe pump via flexible tubing. After the coating was applied, an in-line 1 m long convection oven with air heated to 55°C flowing on top and bottom of the film was used to cure the silicone.

D. EXPERIMENTAL VARIATION OF CONCENTRATION OF SODIUM ION IN THE ENCAPSULATION

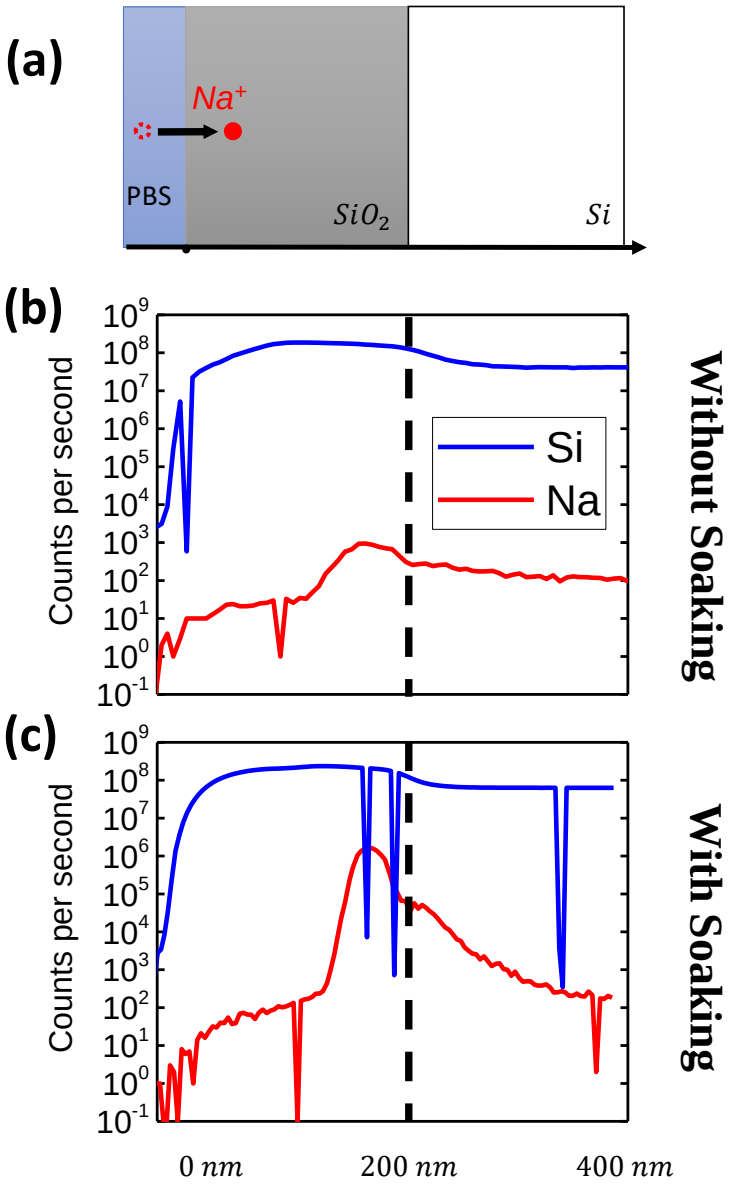

Fig. D.1.: SIMS measurement result for the samples from the soaking test.

Fig.D.1 (a) shows that the test structure has a $200nm$ thermal SiO_2 layer grown on top of the Si substrate. We prepared two samples from the same wafer. We soaked one sample in 70°C PBS solution for 48 hours (salt-soaked sample) and left the other sample untreated (control sample) for comparison. Next, we conducted the SIMS profiling of the two samples. As shown in Fig. D.1 (b) and (c), the Si line identifies the sample structure. From 0 to $200nm$, the Si count remains at a relative high value, identifying the region as the SiO_2 layer. After $200nm$, the Si line drops down and remains a constant value in the Si substrate. The larger signal in SiO_2 is due to the enhancement of positive ion yield by the presence of oxygen. Therefore, we can directly locate the thermal SiO_2 layer from the Si element line. The vertical dashed line in Fig. D.1 (b) and (c) indicates the Si/SiO_2 interface.

VITA

VITA

Xin Jin was born in Nanjing, China on the 28th of October, 1989. In May 2013, he received Bachelor's degrees from Purdue University, West Lafayette. In the same year, he continue as a direct PhD student at Purdue university, in the department of Electrical and Computer Engineering, and became a research assistant in the Prof. Alam's CEED group. His research interests are design and analysis of electrochemical/biosensors for IoT applications (e.g., wearable and implantable devices). He is a multidisciplinary researcher who is familiar with both the electrochemical, mechanical (i.e., structural, thermal, reliability) aspect of sensor design. He is proficient in various analytical tools such as finite-element analysis, compact modeling, statistical/machine learning analysis for the optimization of electronic devices. He has years of practical experience in designing ultra-sensitive sensors for healthcare and precision agriculture applications. He is interested in developing new design approaches to optimize sensor performances (i.e., enhance SNR, reduce response time) and solving real-world design problems to push the boundary of the technology.